Intermolecular Covalent Interactions

de Azevedo Santos, Lucas

2021

document version
Publisher's PDF, also known as Version of record

Intermolecular Covalent Interactions

A Quantitative Molecular Orbital Perspective

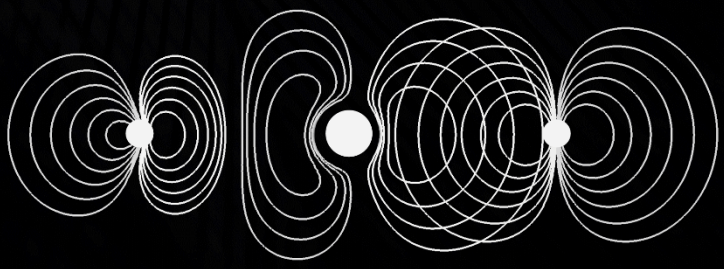

Lucas de Azevedo Santos

VRIJE UNIVERSITEIT

Intermolecular Covalent Interactions

A Quantitative Molecular Orbital Perspective

ACADEMISCH PROEFSCHRIFT

ter verkrijging van de graad Doctor of Philosophy aan
de Vrije Universiteit Amsterdam en
Universidade Federal de Lavras,
op gezag van de rectores magnifici
prof.dr. C.M van Praag
en prof.dr. J.C. Resende Júnior,
in het openbaar te verdedigen
ten overstaan van de promotiecommissie
van de Faculteit der Bètawetenschappen
op dinsdag 2 november 2021 om 11.45 uur
in een bijeenkomst van de universiteit,
De Boelelaan 1105

door

Lucas de Azevedo Santos

geboren te Lavras, Brazilië

promotoren:	prof.dr. F.M. Bickelhaupt
	prof.dr. T.C. Ramalho
copromotor:	dr. T.A. Hamlin
promotiecommissie:	prof.dr. P. Gori-Giorgi
	prof.dr. I. Fernandez
	dr. S. Simon Rabasseda
	prof.dr. R. Marek
	prof.dr. M.P. de Freitas
	prof.dr. N.P.E. Vermeulen

LUCAS DE AZEVEDO SANTOS

INTERMOLECULAR COVALENT INTERACTIONS

A QUANTITATIVE MOLECULAR ORBITAL PERSPECTIVE

LAVRAS – MG | AMSTERDAM – NL

2021

LUCAS DE AZEVEDO SANTOS

INTERMOLECULAR COVALENT INTERACTIONS

A QUANTITATIVE MOLECULAR ORBITAL PERSPECTIVE

Tese apresentada à Universidade Federal de Lavras, como parte das exigências do Programa de Pós-Graduação em Agroquímica, área de concentração em Química/Bioquímica, para a obtenção do título de Doutor, e em conformidade com o acordo acadêmico internacional para diploma duplo de doutorado firmado com a Vrije Universiteit Amsterdam.

Prof. Dr. Teodorico de Castro Ramalho (UFLA)
Prof. Dr. F. Matthias Bickelhaupt (VU)
Orientador

Dr. Trevor A. Hamlin (VU)
Coorientador

LAVRAS – MG | AMSTERDAM – NL

2021

Ficha catalográfica elaborada pelo Sistema de Geração de Ficha Catalográfica da Biblioteca Universitária da UFLA, com dados informados pelo(a) próprio(a) autor(a).

de Azevedo Santos, Lucas.
Intermolecular Covalent Interactions : A Quantitative Molecular Orbital Perspective / Lucas de Azevedo Santos. - 2021.
126 p.

Orientador(a): Teodorico de Castro Ramalho.
Coorientador(a): Friedrich Matthias Bickelhaupt, Trevor Alexander Hamlin.
Tese (doutorado) - Universidade Federal de Lavras, 2021.
Bibliografia.

1. Interações intermoleculares. 2. Teoria de ligação. 3. Teoria do funcional de densidade. I. de Castro Ramalho, Teodorico. II. Bickelhaupt, Friedrich Matthias. III. Hamlin, Trevor Alexander.

LUCAS DE AZEVEDO SANTOS

INTERMOLECULAR COVALENT INTERACTIONS

A QUANTITATIVE MOLECULAR ORBITAL PERSPECTIVE

Tese apresentada à Universidade Federal de Lavras, como parte das exigências do Programa de Pós-Graduação em Agroquímica, área de concentração em Química/Bioquímica, para a obtenção do título de Doutor, e em conformidade com o acordo acadêmico internacional para diploma duplo de doutorado firmado com a Vrije Universiteit Amsterdam.

Aprovada em 02 de novembro de 2021

Prof. Dr. Paola Gori-Giorgi

Prof. Dr. Israel Fernandez

Dr. Sílvia Simon Rabasseda

Prof. Dr. Radek Marek

Prof. Dr. Matheus Puggina de Freitas

Prof. Dr. Teodorico de Castro Ramalho (UFLA)
Prof. Dr. F. Matthias Bickelhaupt (VU)
Orientador

Dr. Trevor A. Hamlin (VU)
Coorientador

LAVRAS – MG | AMSTERDAM – NL

2021

Intermolecular Covalent Interactions

A Quantitative Molecular Orbital Perspective

Lucas de Azevedo Santos

This work has been financially supported by the Fundação de Amparo à Pesquisa do Estado de Minas Gerais (FAPEMIG), by the Conselho Nacional de Desenvolvimento Científico e Tecnológico (CNPq), by the Coordenação de Aperfeiçoamento de Pessoal de Nível Superior (CAPES), and by the Netherlands Organization for Scientific Research (NWO).

Intermolecular Covalent Interactions
A Quantitative Molecular Orbital Perspective
Lucas de Azevedo Santos
2021

Resumo

Esta tese aborda investigações detalhadas utilizando métodos quantum-mecânicos acerca da força e natureza de interações intermoleculares nos complexos $D_mZ\bullet\bullet\bullet A^-$, mediados pelos átomos Z pertencentes aos grupos 15–17 da tabela periódica, baseando-se na teoria quantitativa dos orbital moleculares de Kohn-Sham. A princípio, foi realizado um benchmark dos métodos *ab initio*, bem como uma validação da teoria do funcional de densidade (DFT). Para cada tipo de ligação, isto é, para ligação de pnictogênio (PnB) e ligação de calcogênio (ChB), assim como por meios de comparação, para ligação de halogênio (XB) e ligação de hidrogênio (HB), foram acuradamente computadas tendências para força e comprimento de ligação, baseando-se em um conjunto de dados consistente obtido pelo método DFT anteriormente validado. Aqui, a principal finalidade é estabelecer uma visão unificada das PnB, ChB e XB, assim como da ligação de hidrogênio (HB). Análises mostram que as interações intermoleculares são significativamente covalentes e, certamente, suas naturezas não são predominantemente eletrostáticas, como é incorretamente proposto pelo modelo σ-*hole*, cujas fraquezas são consistentemente explicitadas. Portanto, os resultados encontrados nesta tese sugerem que a designação "Interações Não-Covalentes (NCI)", comumente utilizada para as interações intermoleculares em questão, não cobre apropriadamente suas naturezas e aqui é proposto que a mesma designação seja substituída pela mais adequada "Interações Intermoleculares Covalentes (ICI)".

Palavras-chave: Interações intermoleculares. Benchmark. Teoria do funcional de densidade. Teoria de ligação.

Abstract

This thesis reports detailed quantum chemical investigations on the nature and strength of intermolecular interactions in $D_mZ\bullet\bullet\bullet A^-$ complexes, mediated via atoms Z of groups 15–17 in the periodic table, based on quantitative Kohn-Sham molecular orbital theory. In the first stage, accurate *ab initio* benchmark and density functional theory (DFT) validation studies have been done. For each type of bond, pnictogen bond (PnB) and chalcogen bond (ChB), and, for comparison, halogen bond (XB) and hydrogen bonds (HB), accurate trends in bond length and strength are computed, based on a consistent set of data from our validated relativistic DFT approach. The main purpose is to provide a unified picture of chalcogen bonds and pnictogen bonds, together with hydrogen bonds and halogen bonds. The analyses herein reveal that the intramolecular interactions have a strong covalent component and are certainly not dominantly electrostatic in nature, as it is incorrectly suggested by the σ-hole model whose weaknesses are consistently exposed. The findings in this thesis work thus suggest that the commonly accepted designation "Non-Covalent Interactions (NCI)" for the pertinent intermolecular interactions does not properly cover their nature and it is proposed to replace this designation with the more appropriate "Intermolecular Covalent Interactions (ICI)".

Keywords: Intermolecular interactions. Benchmark. Density Functional Theory. Bond Theory.

Table of contents

SECTION A

1 | General Introduction

Matter does not want to be isolated; it seems. Different particles spontaneously combine to form atoms that, in turn, make bonds with other atoms to form molecules. Quite social entities, one would say. This impulse to interact is the driving force that gives rise to bigger molecular aggregates and, ultimately, forms everything we can touch and see. Then, understanding this impulse is crucial to comprehend the part of the universe itself. Especially for chemists, the interaction between molecules, referred to as intermolecular interactions, has been extensively studied to explain phenomena in several fields of chemistry, such as in catalysis, biological and supramolecular chemistry, and spectroscopy.

In physics, it is all about kinetic and potential energies, but chemists use their chemical intuition to translate the different ways these energies manifest into more feasible terms, such as spatial repulsion or electrostatic attraction. However, with the flourishing of computational methods, chemists do not need to rely on their (good) intuition but directly extract data from accurate calculations based on physical models. The main goal of this thesis is to provide a unified view of the most prominent intermolecular interactions based on sound and quantitative methods to rationalize the bonding mechanism, or the impulse to interact, between molecules. Herein, pnictogen bonds (PnB), chalcogen bonds (ChB), halogen bonds (XB), and hydrogen bonds (HB), are featured along the following chapters divided into two sections: Section A, containing Chapters 1 and 2, with the theoretical background of the key subjects addressed in this thesis; and Section B, containing Chapters 3 to 6, with the state-of-the-art findings published in scientific journals.

Chapter 3 in Section B of this thesis summarizes a benchmark study on anionic $D_2Ch{\bullet\bullet\bullet}A^-$ chalcogen bonds (Ch = S, Se; D, A = F, Cl). This is done by computing the chemical stability of the $D_2Ch{\bullet\bullet\bullet}A^-$ complexes in a double-hierarchical manner, that is, along the series of increasingly accurate relativistic *ab initio* methods as well as along with a series of increasingly accurate basis sets. Thus, in these double-hierarchical series, the description of Coulomb correlation between electrons in the quantum chemical model as well as the number of functions per *nl* shell (flexibility), the number of polarization functions, and the number of

diffuse functions in the basis set have been systematically increased to achieve trustworthy converged complexation energies. The best combination of relativistic *ab initio* method and basis set is used as a reference to evaluate the performance of 13 density functionals to obtain accurate geometries, complexation energies, and correct trends on chemical stability.

Next, the nature of archetypal $D_2Ch{\bullet\bullet\bullet}A^-$ chalcogen bonds and $D_3Pn{\bullet\bullet\bullet}A^-$ pnictogen bonds (Ch = O, S, Se, Te; Pn = N, P, As, Sb; D, A = F, Cl, Br) is investigated in Chapters 4 and 5, respectively. In the literature, these bonds have been extensively explained by qualitative electrostatic models. Herein, the bonding mechanism between the associated bond donor, D_2Ch or D_3Pn, and the bond acceptor, A^-, is analyzed through quantitative Kohn-Sham molecular orbital theory. Trends in chemical stability of $D_2Ch{\bullet\bullet\bullet}A^-$ and $D_3Pn{\bullet\bullet\bullet}A^-$ complexes are also provided based on a set of consistent data, which complements previous data on $DX{\bullet\bullet\bullet}A^-$ halogen bonds and $DH{\bullet\bullet\bullet}A^-$ hydrogen bonds (X, D, A = F, Cl, Br), allowing the systematic comparison between PnB, ChB, XB, and HB. Finally, a summary containing all key findings shown in Chapters 3 to 5 can be found in Chapter 6.

2 | Theoretical Background

2.1 Quantum Chemistry

Chemistry is the field of science that deals with the structure, properties, and transformation of molecules. Theoretical chemistry is the area of chemistry that describes and explains chemical phenomena proceeding from the laws of physics (CRAMER, 2004; JENSEN, 2006). Only one-electron systems have an analytical solution, whereas numerical approaches have been employed to deal with many-bodies systems (CRAMER, 2004; JENSEN, 2006). In addition to advances in computational processing and technology, quantum chemistry has strengthened bonds with high-performance computers to solve numerical problems, giving rise to Computational Chemistry, which focuses on the solution of problems in chemistry and on the development of new concepts.

The Nobel prize winner Erwin Schrödinger has developed a quantum mechanical description of microparticles based on their wave-like behavior which has as its central working equation the so-called Schrödinger equation [see Eq. (2.1)] (COHEN-TANNOUDJI; DIU; LALOË; 2005; SZABO; OSTLUND, 1996)

$$H|\Psi\rangle = E|\Psi\rangle \tag{2.1}$$

In the above equation, H is the Hamiltonian (or energy) operator, the eigenfunction $|\Psi\rangle$ is the wave function describing the system of interest, and the eigenvalue E is the total energy of that system.

There is no analytical solution for the Schrödinger equation for atomic or molecular systems of more than one electron and, thus, approximations need to be introduced. The Born-Oppenheimer approximation considers the electrons to be moving in the field of fixed nuclei, leading to a simplified Hamiltonian operator H for the electronic problem which comprises the terms written in Eq. (2.2).

$$H = T_e + V_{en} + V_{ee} + V_{nn} \tag{2.2}$$

In the above equation, the first term is the kinetic energy of the electrons (T_e), and the last three terms are the Coulombic potential energies resulting from the interaction between electrons and nuclei (V_{en}), between electrons (V_{ee}), and between nuclei (V_{nn}).

The solution for the Schrödinger equation can be exact for a non-relativistic one-electron system, leading to a set of eigenfunctions, that is, the atomic orbitals (AO). However, the analytical solution for many-electron systems, which is the case for many chemical investigations, is not possible due to the V_{ee} term. This problem is solved by expressing the electron-electron Coulombic repulsion as the average potential generated by the other electrons, leading to the Hartree-Fock (HF) method (SZABO; OSTLUND, 1996).

The HF method introduces the *N*-electron antisymmetric HF wavefunction Ψ_{HF} that is given by a single Slater determinant of orthonormal one-electron spin orbitals χ_i, the so-called HF orbitals [Eq. (2.3)].

$$\Psi_{HF}(1, \ldots, N) = \frac{1}{\sqrt{N!}} \begin{vmatrix} \chi_1(1) & \chi_2(1) & \cdots & \chi_n(1) \\ \chi_1(2) & \chi_2(2) & \cdots & \chi_n(2) \\ \vdots & \vdots & \vdots & \vdots \\ \chi_1(N) & \chi_2(N) & \cdots & \chi_n(N) \end{vmatrix} \tag{2.3}$$

The HF wavefunction yields the lowest possible expectation value for the exact Hamiltonian operator, E_{HF}, by invoking the variational method [Eq. (2.4)]. The latter ensures that the expectation value of the Hamiltonian for a non-exact but neat (*e.g.*, normalized and square-integrable) trial wavefunction is never lower than the exact ground-state energy, E^0, a circumstance that allows for the application of variational techniques for minimizing the expectation value to find the best possible approximation of the exact energy.

$$E_{HF} = \langle \Psi_{HF}(1, \ldots, N) \mid H \mid \Psi_{HF}(1, \ldots, N) \rangle. \tag{2.4}$$

The HF orbitals χ_i are eigenfunctions of the Hartree-Fock equation [Eq. (2.5)], which features the Fock operator $f(i)$ that also yields the associated HF orbital energies ε_i as eigenvalues.

$$f(i)\chi_i = \varepsilon_i\chi_i \tag{2.5}$$

The Fock operator comprises the one-electron Hamiltonian operator $h(i)$ plus the Hartree-Fock potential $\upsilon^{HF}(i)$, which is the effective potential experienced by the ith electron in the presence of all other electrons (Eq. 2.6).

$$f(i) = h(i) + \upsilon^{HF}(i) \tag{2.6}$$

The Hartree-Fock approximation is a good starting point for computational methods of quantum chemistry. It has a reasonably low computational cost but accounts for roughly 99% of the total energy. The remaining 1% is called Coulomb correlation and is not negligible for describing chemical phenomena, leading to errors in the computed energy and electron density distribution (JENSEN, 2006). Then, more computational demanding post-Hartree-Fock methods need to be invoked to obtain more accurate solutions.

Among the methods that include Coulomb correlation, the second order Møller-Plesset Perturbation method (MP2) has the lowest computational cost and accounts for 80–90% of the correlation energy. Coupled Cluster (CC) methods, for instance, may account in practice for almost all Coulomb correlation, but the applicability of this method is limited to relatively small systems due to its massive computational cost.

2.2 Density Functional Theory

The cost-benefit ratio is rarely in favor of the highly correlated methods in the routine investigations of chemical phenomena. The density functional theory (DFT) has been extensively used in theoretical calculations due to its high suitability to solve different chemical problems, combining computational efficiency and accuracy. The fundamental theorem by Hohenberg and Kohn states that the ground state energy E is uniquely determined by the associated electron density $\rho(r)$ (HOHENBERG; KOHN, 1964). Later, Kohn and Sham established a practical computational formalism for DFT (KOCH; HOLTHAUSEN, 2001). In essence, it is stated that a reference system of N noninteraction electrons moves in an effective external potential $\upsilon_s(r)$, which is such that the squared moduli of the Kohn-Sham (KS) orbitals φ_i correspond to the exact ground state density [see Eq. (2.7) and (2.8)].

$$\left[-\frac{1}{2}\nabla^2+\upsilon_s(r)\right]\varphi_i=\varepsilon_i\varphi_i \tag{2.7}$$

$$\rho(r)=\sum_i^N\left|\varphi_i\right|^2 \tag{2.8}$$

The effective external potential $\upsilon_s(r)$, often referred to as Kohn-Sham potential, accounts for the attractive potential $\upsilon_n(r)$ of the nuclei, the repulsive Coulombic potential $V_\rho(r)$ due to the charge distribution within $\rho(r)$, and the exchange and correlation potential $\upsilon_{XC}(r)$ [Eq. (2.9)].

$$\upsilon_s(r)=\upsilon_n(r)+V_\rho(r)+\upsilon_{XC}(r) \tag{2.9}$$

If $\upsilon_{XC}(r)$ was known, which is not the case, the KS-DFT would lead to the exact energy obtained by the Schrödinger equation [Eq. (2.1)]. Thus, approximations have been developed to obtain the exchange-correlation energy E_{XC} associated with υ_{XC}, using the XC density functionals. The available density functionals use several approximations, for example, the local density approximation (LDA), the generalized gradient approximation (GGA), or a combination of both together with HF exchange (hybrid functionals) and MP2 corrections (double hybrid functionals). The best choice for a particular density functional depends on the system and the physical property of interest and can be inferred from comparison against reference data from accurate experiment or highly correlated *ab initio* computations (BAUZÁ et al, 2013; BENTO; SOLÀ; BICKELHAUPT, 2008; DE AZEVEDO SANTOS et al, 2021c; ŘEZÁC; HOBZA, 2016; SWART; SOLÀ; BICKELHAUPT, 2010).

2.3 Understanding Chemical Bonding

One of the greatest advantages of computational chemistry comes to the surface when the topic is fundamental research. With the right tools, it is possible to find answers for phenomena occurring at the atomic level that may never be fully explained by experiments. In this section, a compact description of the quantitative Kohn-Sham molecular orbital (MO) analysis is found.

This analysis provides a causal explanation to chemical phenomena through quantum chemical meaningful descriptors using Kohn-Sham density functional theory (KS-DFT).

The activation strain model (ASM) is a robust fragment-based method of understanding chemical reactions, but also chemical bonding (BICKELHAUPT; BAERENDS, 2000; FERNÁNDEZ; BICKELHAUPT, 2014; HAMLIN et al, 2021; VERMEEREN et al, 2020; WOLTERS; BICKELHAUPT, 2015). The bonding mechanism between two fragments can be associated with two steps: (i) the fragments need to deform, abandoning their equilibrium geometry, into the atomic arrangement they adopt in the bonded complex; and (ii) the actual chemical interaction between the deformed fragments takes place. The chemical interaction between two fragments starts with both fragments A and B at their own equilibrium geometry, separated by an infinite distance. The associated energy of the fragments A or B at their own equilibrium geometry is written as $E_{\text{geom}}(\text{frag})$ that is, $E_{\text{A}}(\text{A})$ and $E_{\text{B}}(\text{B})$. The final stage is achieved by bringing the two fragments together reaching the equilibrium geometry of the overall complex AB. The energy associated with this new system or complex, namely AB, is written as $E_{\text{AB}}(\text{AB})$. Therefore, the energy associated with the chemical interaction between A and B to form the complex AB is the bond energy ΔE defined by Eq. (2.10). The energy associated with steps (i) and (ii) can be quantified and lead to the same expression as Eq. (2.10).

$$\Delta E = E_{\text{AB}}(\text{A}) - E_{\text{A}}(\text{A}) - E_{\text{B}}(\text{B}) \tag{2.10}$$

The total strain energy ΔE_{strain} is the change in energy associated with the geometrical deformation of both fragments A and B from their equilibrium geometries to the geometry that both fragments adopt at the equilibrium geometry of the complex. In Eq. (2.11), $E_{\text{AB}}(\text{A})$ and $E_{\text{AB}}(\text{B})$ are the respective energies of A and B at the geometry they adopt in complex AB, and $\Delta E_{\text{strain}}(\text{A})$ and $\Delta E_{\text{strain}}(\text{B})$ are the individual strain energies of A and B, respectively.

$$\begin{aligned}
\Delta E_{\text{strain}}(\text{A}) &= E_{\text{AB}}(\text{A}) - E_{\text{A}}(\text{A}) \\
\Delta E_{\text{strain}}(\text{B}) &= E_{\text{AB}}(\text{B}) - E_{\text{B}}(\text{B}) \\
\Delta E_{\text{strain}} &= \Delta E_{\text{strain}}(\text{A}) + \Delta E_{\text{strain}}(\text{B})
\end{aligned} \tag{2.11}$$

The interaction energy accounts for all chemical interactions between the deformed fragments and it is defined by Eq. (2.12). Note that sum of Eq. (2.11) and (2.12) yields exactly the right expression in Eq. (2.10). Therefore, the bond energy ΔE between two fragments can be described by the sum of the total strain energy ΔE_{strain} and the interaction energy ΔE_{int}.

$$\Delta E_{\text{int}} = E_{\text{AB}}(\text{AB}) - E_{\text{AB}}(\text{A}) - E_{\text{AB}}(\text{B}) \tag{2.12}$$

The application of the ASM to chemical interactions extends the decomposition of the ΔE along the reaction coordinate (ξ) [Eq. (2.13)]. ξ can be a critical geometrical parameter, that is, a parameter that directly characterizes the progress of the reaction, onto which, *e.g.*, the intrinsic reaction coordinate (IRC) is projected (VAN ZEIST et al, 2008). A schematic activation strain diagram (ASD) is illustrated in Figure 2.1. Note that the $\Delta E_{\text{strain}}(\xi)$ is always destabilizing and counteracted by the stabilizing $\Delta E_{\text{int}}(\xi)$. The system will reach the equilibrium, that is, the energy minimum for ΔE, when the slope of $\Delta E_{\text{strain}}(\xi)$ equals the negative of the slope of $\Delta E_{\text{int}}(\xi)$.

$$\Delta E(\xi) = \Delta E_{\text{strain}}(\xi) + \Delta E_{\text{int}}(\xi) \tag{2.13}$$

The $\Delta E_{\text{int}}(\xi)$ between the deformed fragments A and B can be further decomposed into three quantum chemically meaningful terms via the canonical energy decomposition analysis (EDA) using KS-DFT (BICKELHAUPT; BAERENDS, 2000; FERNÁNDEZ; BICKELHAUPT, 2014; HAMLIN et al, 2021; VERMEEREN et al, 2020; WOLTERS; BICKELHAUPT, 2015).

$$\Delta E_{\text{int}}(\xi) = \Delta V_{\text{elstat}}(\xi) + \Delta E_{\text{Pauli}}(\xi) + \Delta E_{\text{oi}}(\xi) \tag{2.14}$$

Figure 2.1 – Generic activation strain diagram for chemical bond formation between two fragments projected onto the reaction coordinate.

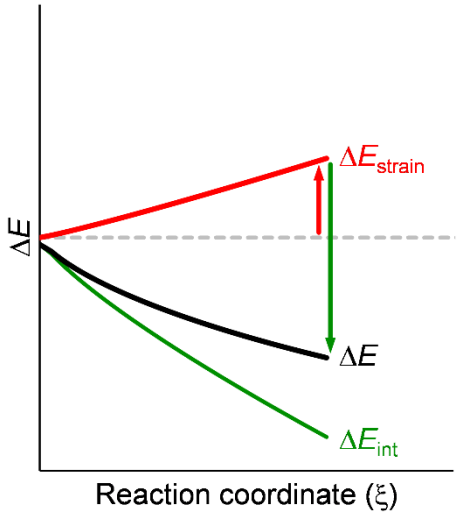

The first term in Eq. (2.14) is the electrostatic interaction $\Delta V_{\text{elstat}}(\xi)$ between the interpenetrating and unperturbed charge distributions of A and B (BICKELHAUPT; BAERENDS, 2000; HAMLIN et al, 2021). $\Delta V_{\text{elstat}}(\xi)$ constitutes of four well-defined terms [Eq. (2.15)]: (i) $\Delta V_{\text{elstat},n\text{A}n\text{B}}(\xi)$ is the classical Coulomb repulsion between the nuclei of A and B; (ii) $\Delta V_{\text{elstat},n\text{A}\rho\text{B}}(\xi)$ is the electrostatic attraction between the nucleus of A and the unperturbed charge density of B; (iii) $\Delta V_{\text{elstat},n\text{B}\rho\text{A}}(\xi)$ is the electrostatic attraction between the nucleus of B and the unperturbed charge density of A; and (iv) $\Delta V_{\text{elstat},\rho\text{A}\rho\text{B}}(\xi)$ is the electrostatic repulsion between the unperturbed charge densities of A and B. The net $\Delta V_{\text{elstat}}(\xi)$ term is usually attractive and only at very short distances $\Delta V_{\text{elstat},n\text{A}n\text{B}}(\xi)$ dominates, resulting in a net repulsive electrostatic interaction (KRAPP; BICKELHAUPT; FRENKING, 2006; RODRIGUES SILVA et al, 2021b).

$$\Delta V_{\text{elstat}}(\xi) = \sum_{\substack{\alpha \in \text{A} \\ \beta \in \text{B}}} \frac{Z_A Z_B}{R_{\alpha\beta}} - \int \sum_{\alpha \in A} \frac{Z_A \rho_B(r)}{|R_\alpha - r|} \mathrm{d}r - \int \sum_{\beta \in B} \frac{Z_B \rho_A(r)}{|R_\beta - r|} \mathrm{d}r + \int\int \frac{\rho_A(r_1)\rho_B(r_2)}{r_{12}} \mathrm{d}r_1 \mathrm{d}r_2$$

$$\Delta V_{\text{elstat}}(\xi) = \Delta V_{\text{elstat},n\text{A}n\text{B}}(\xi) + \Delta V_{\text{elstat},n\text{A}\rho\text{B}}(\xi) + \Delta V_{\text{elstat},n\text{B}\rho\text{A}}(\xi) + \Delta V_{\text{elstat},\rho\text{A}\rho\text{B}}(\xi) \quad (2.16)$$

The Pauli repulsion term $\Delta E_{\text{Pauli}}(\xi)$ stems from the rise in kinetic energy after antisymmetrizing and renormalizing the product wave function $\Psi_\text{A}\Psi_\text{B}$ of the complex AB (see

Figure 2.2) (BICKELHAUPT; BAERENDS, 2000; HAMLIN et al, 2021). Note that this is a necessary operation for the Pauli principle to be obeyed. The resulting wave function is Ψ^0 and the associated interaction energy is $\Delta E^0 = E^0(\mathrm{AB}) - E_{\mathrm{AB}}(\mathrm{A}) - E_{\mathrm{AB}}(\mathrm{B})$, which is typically destabilizing. ΔE^0 can be defined by the sum of its associated potential energy ΔV^0 and kinetic energy ΔT^0 [Eq. (2.16)]. Since the actual electrostatic interaction between A and B is known [Eq. (2.15)], it is assumed that ΔV^0 comprises $\Delta V_{\mathrm{elstat}}$ and the residual potential energy $\Delta V_{\mathrm{Pauli}}$ due to the change in density from $\rho_{\mathrm{A}} + \rho_{\mathrm{B}}$ to ρ^0, where $\Delta E_{\mathrm{Pauli}}$ is $\Delta V_{\mathrm{Pauli}} + \Delta T^0$. $\Delta V_{\mathrm{Pauli}}$ reflects the charge flow out of the overlap region and towards the nuclei of fragments A and B, and it is always attractive. Therefore, the only destabilizing term in $\Delta E_{\mathrm{Pauli}}$ is ΔT^0 that increases with the overlap between the closed-shell orbitals. Note that the nature of Pauli repulsion is purely quantum mechanical (*i.e.*, it originates from the antisymmetry principle for fermions), and it is not the electrostatic repulsion between overlapping charge densities.

$$\Delta E^0 = \Delta V^0 + \Delta T^0$$
$$\Delta E^0 = \Delta V_{\mathrm{elstat}} + \Delta V_{\mathrm{Pauli}} + \Delta T^0$$
$$\Delta E^0 = \Delta V_{\mathrm{elstat}} + \Delta E_{\mathrm{Pauli}} \qquad (2.16)$$

Figure 2.2 – Generic molecular orbital diagram for the complex AB stemming from the interaction between the two closed shell fragments A and B.

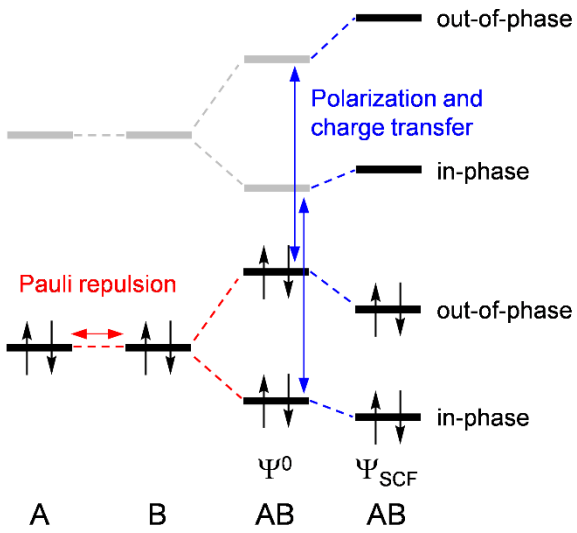

The orbital interactions term $\Delta E_{\mathrm{oi}}(\xi)$ accounts for all polarization and charge transfer effects. It is a direct consequence of relaxing Ψ^0 through a SCF calculation to give the final Ψ^{SCF} wave function of the AB complex, allowing the mixing of all virtual and occupied orbitals

(Figure 2.2) (BICKELHAUPT; BAERENDS, 2000; HAMLIN et al, 2021). Thus, the final expression to ΔE_{oi} is given by Eq. (2.17). The strength of the charge transfer or HOMO–LUMO interactions depends on two main factors: (i) how much the HOMO and the LUMO overlap, given by the quantity ⟨HOMO | LUMO⟩ or $S_{HOMO–LUMO}$; and (ii) the difference in energy between the HOMO and the LUMO (*i.e.* the energy gap, $\Delta\varepsilon$). In other words, $\Delta E_{oi} \propto S^2/\Delta\varepsilon$. Larger $S_{HOMO–LUMO}$ and smaller $\Delta\varepsilon$ results in higher stabilization by charge transfer and, thus, the higher covalent character of the associated chemical interaction.

$$\Delta E_{oi} = E_{AB}(AB) - E^0_{AB}(AB) \tag{2.17}$$

ASM combined with EDA, together with the underlying quantitative canonical MO model, provides a sound quantitative analysis on the chemical interactions and can be performed using the Amsterdam Density Functional (ADF) package (ADF, 2017) This is the main computational strategy used in this thesis to reveal the nature of chalcogen bonds and pnictogen bonds, as well as to point out the limitations of oversimplified pictures to explain intermolecular interactions.

2.4 From Chemical Bonding to Intermolecular Interactions

Among the attractive forces between two fragments to form a chemical bond, there is the electrostatic attraction and the charge transfer (GLENDENING, 1996; MAO et al, 2021; STASYUK et al, 2018). The latter arises from the flow of electrons from one fragment into another and gives the covalent character of chemical bonds. The physical mechanism behind this is one occupied orbital of one fragment which overlaps with an unoccupied orbital of another fragment (Scheme 2.1). For that reason, the stabilization by charge transfer becomes more and more significant at short interatomic separations but is gradually offset by the repulsive forces, mostly originated by the steric Pauli repulsion since the overlap between occupied orbitals will also increase and the electrons cannot occupy the same space due to the exclusion principle (Scheme 2.1) (ALBRIGHT, 2013; BICKELHAUPT; BAERENDS, 2000). At exceptionally long interatomic separations, the steric Pauli repulsion decreases, as well as the charge transfer, and the weak electrostatic attraction, together with dispersion forces, dominates. Ultimately, the balance between repulsive and attractive forces will not only

determine the strength of a chemical bond but also the bond length (KRAPP; BICKELHAUPT; FRENKING, 2006; ZHAO et al, 2019; RODRIGUES SILVA et al, 2021a).

Scheme 2.1 – Generic MO diagram of DH•••A⁻ hydrogen bonds (D, A = halogen). Orbital interactions in blue and Pauli repulsion in red (WOLTERS; BICKELHAUPT, 2012).

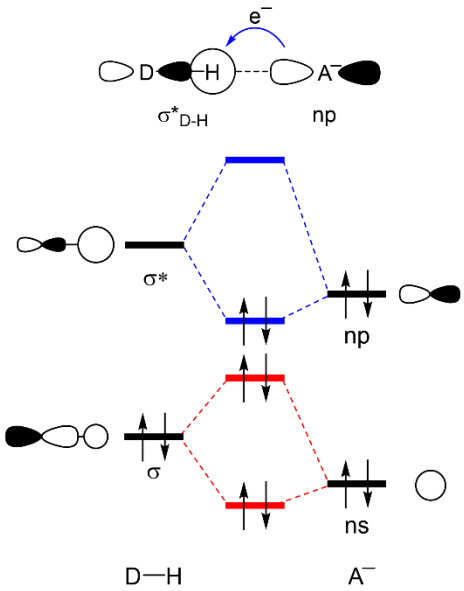

The same physical forces governing the interactions between atoms are also present in interactions between polyatomic fragments, that is, systems made of two or various molecules. Intermolecular interactions are physically similar to chemical bonds but weaker and longer due to, in general, larger HOMO–LUMO gaps and higher steric demand. In addition, the long bond separation also leads to weaker electrostatic attraction. For example, the dissociation energy of the hydrogen-bonded water dimer H_2O•••HOH is ca. 3 kcal mol^{-1}, massively weaker than the HO–H bonds with homolytic bond dissociation energy of ca. 103 kcal mol^{-1} (LUO, 2007). In addition, the O•••H separation is around 1.95 Å in the water dimer, whereas the O–H bond length is around 0.96 Å (LEFORESTIER; SZALEWICZ; VAN DER AVOIRD, 2012; ROCHER-CASTERLINE, 2011; SHANK et al, 2009) (see Figure 2.3). Nevertheless, the strength of intermolecular interactions is often related to, exclusively, the electrostatic properties of molecules. That is, highly polar molecules can engage in strong long-range attractive electrostatic interactions. On the other hand, the interaction between nonpolar molecules is so weak that other minor effects, such as dispersion, become relevant (KOLLMAN, 1977; LENNARD-JONES, 1931). Because of this purely electrostatic picture, augmented by dispersion interactions, intermolecular interactions are often referred to as Non-

Covalent Interactions (NCI) (ALKORTA; ELGUERO; FRONTERA, 2020; POLITZER; MURRAY, 2015). Recently, oversimplified *electrostatic-only* models have been used to explain the nature of not only hydrogen bonds (HB), but also pnictogen bonds (PnB), chalcogen bonds (ChB), and halogen bonds (XB) (CLARK et al, 2007; POLITZER; MURRAY, 2015, 2017, 2019, 2020; POLITZER; MURRAY; CLARK, 2013; POLITZER et al, 2017). In the σ-hole model, molecules holding a H, Pn, Ch, or X atom are treated as a surface with a molecular electrostatic potential (MEP), in which its positive region can engage in attractive electrostatic interactions with a negative point charge-like Lewis base. Note that this point of view completely neglects the fact that two interacting molecules are not surfaces or point charges, but two interpenetrating charge distributions. In addition, the bonding mechanism of intermolecular interactions depends on a much more complex interplay of factors.

Figure 2.3 – Oxygen-hydrogen bond lengths in the water dimer (O, red; H, white).

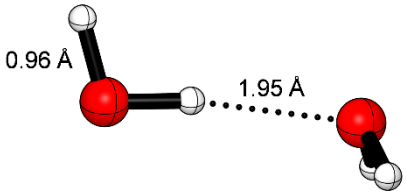

The anionic hydrogen bonds DH•••A^- have a stability of ca. 80 kcal mol^{-1} for D = I and A^- = F^-. This stability decreases if A^- is a weaker Lewis basis, ca. 20 kcal mol^{-1} for A^- = I^-, but also surprisingly decreases if the polarity of the D–H bond increases. The hydrogen-bond strength between the highly polar FH fragment and the halide F^- is ca. 50 kcal mol^{-1}, that is, 30 kcal mol^{-1} weaker than for the less polar IH fragment (see Figure 2.4a). This can be counterintuitive from the point of view of the above-mentioned oversimplified electrostatic model because the latter is simply incomplete and misses an important fact: *intermolecular interactions can also be covalent*.

Just like in chemical bonds, the molecular wave functions overlap, similarly to the atomic wave functions, to assume states of lower energies. In the case of DH•••A^-, the lowest unoccupied molecular orbital (LUMO; σ* acceptor orbital) of the DH fragment and the highest occupied molecular orbital (HOMO; np lone pair orbital) of the halide A^- overlaps to form a new state, even lower in energy, to stabilize the system (see Scheme 2.1). This type of interaction is often referred to as donor–acceptor or HOMO–LUMO interactions, in which the bond donor is often a Lewis base that donates charge into the bond acceptor, a Lewis acid

(RODRIGUES SILVA et al, 2020). As aforementioned, the magnitude of the charge transfer and, thus, the covalent character of intermolecular interactions, depends on the overlap between the filled and unfilled orbitals (*e.g.*, HOMO and LUMO, respectively) and on their difference in energy (Δε). The IH fragment can engage in stronger hydrogen bonds than FH simply because the σ* I–H antibonding acceptor orbital on the IH fragment is lower in energy than the σ* F–H antibonding acceptor orbital on the FH fragment, resulting in smaller HOMO–LUMO Δε and, therefore, more stabilization by charge transfer (see Figure 2.4b) (WOLTERS; BICKELHAUPT, 2012). In other words, on top of having strong electrostatic attraction, the hydrogen bonds are substantially covalent in nature, and a pure electrostatic picture provides an incomplete description of HB (MOROKUMA, 1971; SWART; FONSECA GUERRA; BICKELHAUPT, 2004; WOLTERS; BICKELHAUPT, 2012).

Figure 2.4 – a) Molecular electrostatic potential of the DH fragment at 0.01 a.u. (blue, positive; red, negative; see color scale) and b) HOMO–LUMO interactions within the DH•••F⁻ hydrogen bonded complexes (D = F, I; F, green; I, purple; H, white) computed at ZORA-BP86/TZ2P level. This is a reproduction of the results from Wolters and Bickelhaupt (WOLTERS; BICKELHAUPT, 2012).

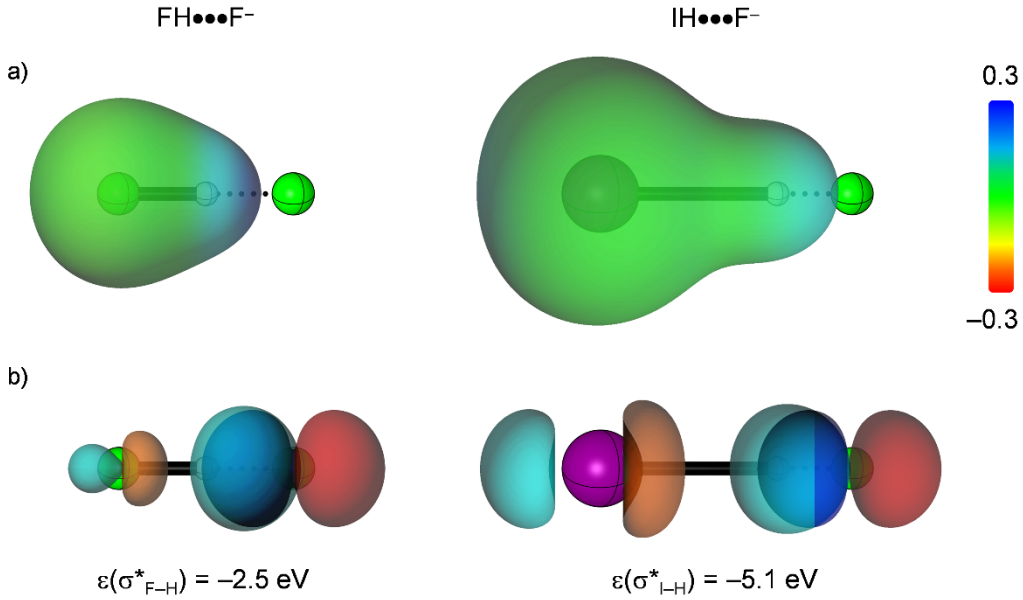

The manifestation of the charge transfer is confirmed by the red-shifting of the D–H bonds, that is, the elongation of D–H bonds as a consequence of the charge donation into the σ* D–H acceptor orbital (CHANG et al, 2016; WOLTERS; BICKELHAUPT, 2012). Note that the σ* D–H acceptor orbital has an anti-bonding D–H character and, therefore, goes down in energy as the D–H bond expands (see Scheme 2.1) (WOLTERS; BICKELHAUPT, 2012). For this reason, the HOMO–LUMO interactions become stronger as the D–H bond weakens and

can expand to a higher degree, because the associated σ* D–H acceptor orbital quickly drops in energy, resulting in smaller Δε. Then, the D–H bond expansion causes the vibrational frequency on the infrared spectrum related to the D–H bond stretch to decrease (*i.e.* to red-shift). The nature of the redshift lies in an important quantum chemical phenomenon, that is, the orbital interactions that are not exclusive to hydrogen bonds but occurs in all types of intermolecular interactions (WOLTERS; BICKELHAUPT, 2012; DE AZEVEDO SANTOS et al, 2021a; 2021b). The following Chapters of this thesis show that, similarly to the hydrogen bonds, PnB, ChB, and XB are significantly covalent in nature, and NCI is not a suitable terminology to refer to these intermolecular interactions. In this thesis, it is introduced the designation “Intermolecular Covalent Interactions (ICI)”, which appropriately suggests the covalent nature of PnB, ChB, and XB.

2.5 References

ADF. Version 2017.103. [S.1]: SCM Theoretical Chemistry, 2017. http://www.scm.com.

ALBRIGHT, T. A.; BURDETT, J. K.; WHANGBO, M. -H. **Orbital Interactions in Chemistry**. 2. ed. Chichester: John Wiley & Sons, Ltd, 2013.

ALKORTA, I.; ELGUERO, J.; FRONTERA, A. Not Only Hydrogen Bonds: Other Noncovalent Interactions. **Crystals**, Basel, v. 10, n. 3, p. 180, 2020.

BAUZÁ, A. et al. On the Reliability of Pure and Hybrid DFT Methods for the Evaluation of Halogen, Chalcogen, and Pnicogen Bonds Involving Anionic and Neutral Electron Donors. **Journal of Chemical Theory and Computation**, Washington, v. 9, n. 11, p. 5201–5210, 2013.

BENTO, P. A.; SOLÀ, M.; BICKELHAUPT, F. M. E2 and S_N2 Reactions of $X^- + CH_3CH_2X$ (X = F, Cl); an *ab Initio* and DFT Benchmark Study. **Journal of Chemical Theory and Computation**, Washington, v. 4, n. 6, p. 929–940, 2008.

BICKELHAUPT, F. M.; BAERENDS, E. J. Kohn-Sham Density Functional Theory: Predicting and Understanding Chemistry. In: **Reviews in Computational Chemistry**, New York, John Wiley and Sons, Inc., v. 15, p. 1–86, 2000.

CHANG, X. et al. Red-Shifting versus Blue-Shifting Hydrogen Bonds: Perspective from Ab Initio Valence Bond Theory. **The Journal of Physical Chemistry A**, Washington, v. 120, n. 17, p. 2749–2756, 2016.

CLARK, T.; HENNEMANN, M.; MURRAY, J. S.; POLITZER, P. Halogen bonding: the σ-hole. **Journal of Molecular Modeling**, New York, v. 13, n. 2, p. 291–296, 2007.

COHEN-TANNOUDJI, C.; DIU, B.; LALOË, F. **Quantum Mechanics**. vol. 1 ed. [s.l.] John Wiley & Sons. Inc., 2005.

CRAMER, C. J. **Essentials of Computational Chemistry: Theories and Models**. 2. ed. Chichester: John Wiley & Sons, Ltd, 2004.

DE AZEVEDO SANTOS, L. et al. A Quantitative Molecular Orbital Perspective of the Chalcogen Bond. **ChemistryOpen**, Weinheim, v. 10, n. 4, p. 391–401, 2021.

DE AZEVEDO SANTOS, L. et al. The Pnictogen Bond: A Quantitative Molecular Orbital Picture. **Physical Chemistry Chemical Physics**, Cambridge, accepted, 2021.

DE AZEVEDO SANTOS, L. et al. Chalcogen bonds: Hierarchical *ab initio* benchmark and density functional theory performance study. **Journal of Computational Chemistry**, Hoboken, v. 42, n. 10, p. 688–698, 2021.

FERNÁNDEZ, I.; BICKELHAUPT, F. M. The activation strain model and molecular orbital theory: understanding and designing chemical reactions. **Chemical Society Reviews**, Cambridge, v. 43, n. 14, p. 4953–4967, 2014.

GLENDENING, E. D. Natural Energy Decomposition Analysis: Explicit Evaluation of Electrostatic and Polarization Effects with Application to Aqueous Clusters of Akali Metal Cations and Neutrals. **Journal of the American Chemical Society**, Washington, v. 118, n. 10, p. 2473–2482, 1996.

HAMLIN, T. A. et al. Energy decomposition analysis in the context of quantitative molecular orbital theory. In: **Complementary Bonding Analyses**, Berlin, De Gruyter, p. 199–212, 2021.

HOHENBERG, P.; KOHN, W. Inhomogeneous Electron Gas. **Physical Review**, College Park, v. 136, n. 3, p. 864–871, 1964.

JENSEN, F. **Introduction to Computational Chemistry**. 2. ed. Chichester: John Wiley & Sons, Ltd, 2006.

KOCH, W.; HOLTHAUSEN, M. C. **A Chemist's Guide to Density Functional Theory**. 2. ed. Weinheim: Wiley-VCH, 2001.

KOLLMAN, P. A. Noncovalent Interactions. **Accounts of Chemical Research**, Washington, v. 10, n. 10, p. 365–371, 1977.

KRAPP, A.; BICKELHAUPT, F. M.; FRENKING, G. Orbital Overlap and Chemical Bonding. **Chemistry - A European Journal**, Weinheim, v. 12, n. 36, p. 9196–9216, 2006.

LEFORESTIER, C.; SZALEWICZ, K.; VAN DER AVOIRD, A. Spectra of water dimer from a new *ab initio* potential with flexible monomers. **The Journal of Chemical Physics**, Melville, v. 137, n. 1, p. 014305, 2012.

LENNARD-JONES, J. E. Cohesion. **The Proceedings of the Physical Society**, Bristol, v. 43, n. 240, p. 461–482, 1931.

LIDE, D. R. **CRC Handbook of Chemistry and Physics**. 84 ed. Boca Raton: CRC Press, 2003.

LUO, Y. R. **Comprehensive Handbook of Chemical Bond Energies**. Boca Raton: CRC Press, 2007.

MAO, Y. et al. From Intermolecular Interaction Energies and Observable Shifts to Component Contributions and Back Again: A Tale of Variational Energy Decomposition Analysis. **Annual Review of Physical Chemistry**, Palo Alto, v. 72, p. 1–28, 2021.

MOROKUMA, K. Molecular Orbital Studies of hydrogen Bonds. III. C=O•••H–O Hydrogen Bond in H_2CO•••H_2O and H_2CO•••$2H_2O$. **The Journal of Chemical Physics**, Melville, v. 55, n. 3, p. 1236–1244, 1971.

POLITZER, P.; MURRAY, J. S. A Unified View of Halogen Bonding, Hydrogen Bonding and Other σ-Hole Interactions. In: **Noncovalent Forces. Challenges and advances in Computational Chemistry and Physics**, Cham, Springer, v. 19, p. 291–321, 2015.

POLITZER, P.; MURRAY, J. S. Molecular electrostatic potentials and noncovalent interactions. **WIREs Computational Molecular Science**, Hoboken, v. 7, n. 6, p. e13260, 2017.

POLITZER, P.; MURRAY, J. S. An Overview of Strengths and Directionalities of Noncovalent Interactions: σ-Holes and π-Hole. **Crystals**, Basel, v. 9, n. 3, p. 165, 2019.

POLITZER, P.; MURRAY, J. S. Electrostatics and Polarization in σ- and π-Hole Noncovalent Interactions: An Overview. **ChemPhysChem**, Weinheim, v. 21, n. 7, p. 579–588, 2020.

POLITZER, P.; MURRAY, J. S.; CLARK, T. Halogen bonding and other σ-hole interactions: a perspective. **Physical Chemistry Chemical Physics**, Cambridge, v. 15, n. 27, p. 11178–11189, 2013.

POLITZER, P. et al. The σ-hole revisited. **Physical Chemistry Chemical Physics**, Cambridge, v. 19, n. 48, p. 32166–32178, 2017.

ŘEZÁC, J.; HOBZA, P. Benchmark Calculations of Interaction Energies in Noncovalent Complexes and Their Applications. **Chemical Reviews**, Washington, v. 116, n. 9, p. 5038–5071, 2016.

ROCHER-CASTERLINE, B. E. et al. Communication: Determination of the bond dissociation energy (D_0) of the water dimer, $(H_2O)_2$, by velocity map imaging. **The Journal of Chemical Physics**, Melville, v. 134, n. 21, p. 211101, 2011.

RODRIGUES SILVA, D. et al. Nature and Strength of Lewis Acid/Base Interaction in Boron and Nitrogen Trihalides. **Chemistry – An Asian Journal**, Weinheim, v. 15, n. 23, p. 4043–4054, 2020.

RODRIGUES SILVA, D. et al. The *Gauche* Effect in XCH_2CH_2X Revisited. **ChemPhysChem**, Weinheim, v. 22, p. 641–648, 2021.

RODRIGUES SILVA, D. et al. Dipolar Repulsion in α-Halocarbonyl Compounds Revisited. **Physical Chemistry Chemical Physics**, Cambridge, submitted, 2021.

SHANK, A. et al. Accurate *ab initio* and "hybrid" potential energy surfaces, intramolecular vibrational energies, and classical ir spectrum of the water dimer. **The Journal of Chemical Physics**, Melville, v. 130, n. 14, p. 144314, 2009.

STASYUK, O. A. et al. Comparison of the DFT-SAPT and Canonical EDA Schemes for the Energy Decomposition of Various Types of Noncovalent Interactions. **Journal of Chemical Theory and Computation**, Washington, v. 14, n. 7, p. 3440–3450, 2018.

SWART, M.; FONSECA GUERRA, C.; BICKELHAUPT, F. M. Hydrogen Bonds of RNA Are Stronger than Those of DNA, but NMR Monitors Only Presence of Methyl Substituent in Uracil/Thymine. **Journal of the American Chemical Society**, Washington, v. 126, n. 51, p. 16718–16719, 2004.

SWART, M.; SOLÀ, M.; BICKELHAUPT, F. M. Density Functional Calculations of E2 and S_N2 Reactions: Effects of the Choice of Method, Algorithm, and Numerical Accuracy. **Journal of Chemical Theory and Computation**, Washington, v. 6, n. 10, p. 3145–3152, 2010.

SZABO, A.; OSTLUND, N. S. **Modern Quantum Chemistry: Introduction to Advanced Electronic Structure Theory**. Mineola: Dover Publications, Inc., 1996.

VAN ZEIST, W. -J. et al. Reaction Coordinates and the Transition-Vector Approximation to the IRC. **Journal of Chemical Theory and Computation**, Washington, v. 4, n. 6, p. 920–928, 2008.

VERMEEREN, P. et al. Understanding chemical reactivity using the activation strain model. **Nature Protocols**, London, v. 15, n. 2, p. 649–667, 2020.

WOLTERS, L. P.; BICKELHAUPT, F. M. Halogen Bonding versus Hydrogen Bonding: A Molecular Orbital Perspective. **ChemistryOpen**, Weinheim, v. 1, n. 2, p. 96–105, 2012.

WOLTERS, L. P.; BICKELHAUPT, F. M. The activation strain model and molecular orbital theory. **WIREs Computational Molecular Science**, Hoboken, v. 5, n. 4, p. 324–343, 2015.

ZHAO, L. et al. Chemical Bonding and Bonding Models of Main-Group Compounds. **Chemical Reviews**, Washington, v. 119, n. 14, p. 8781–8845, 2019.

SECTION B

3 | Hierarchical *Ab Initio* Benchmark on Chalcogen Bonds

Part of this chapter previously appeared as

Chalcogen Bonds: Hierarchical Ab Initio Benchmark and DFT Performance Study

L. de Azevedo Santos, T. C. Ramalho, T. A. Hamlin, F. Matthias Bickelhaupt

J. Comp. Chem. **2021**, *10*, 688–698

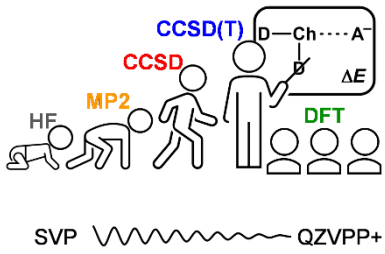

Abstract | We have performed a hierarchical *ab initio* benchmark and DFT performance study of $D_2Ch{\bullet\bullet\bullet}A^-$ chalcogen bonds (Ch = S, Se; D, A = F, Cl). The *ab initio* benchmark study is based on a series of ZORA-relativistic quantum chemical methods [HF, MP2, CCSD, CCSD(T)], and all-electron relativistically contracted variants of Karlsruhe basis sets (ZORA-def2-SVP, ZORA-def2-TZVPP, ZORA-def2-QZVPP) with and without diffuse functions. The highest-level ZORA-CCSD(T)/ma-ZORA-def2-QZVPP counterpoise-corrected complexation energies (ΔE_{CPC}) are converged within 1.1–3.4 kcal mol^{-1} and 1.5–3.1 kcal mol^{-1} with respect to the method and basis set, respectively. Next, we used the ZORA-CCSD(T)/ma-ZORA-def2-QZVPP (ΔE_{CPC}) as reference data for analyzing the performance of 13 different ZORA-relativistic DFT approaches in combination with the Slater-type QZ4P basis set. We find that the three-best performing functionals are M06-2X, B3LYP, and M06, with mean absolute errors (MAE) of 4.1, 4.2, and 4.3 kcal mol^{-1}, respectively. The MAE for BLYP-D3BJ and PBE amount to 8.5 and 9.3 kcal mol^{-1}, respectively.

Keywords | Benchmark study, Chalcogen bonds, Coupled-cluster, Density functional calculations, Noncovalent interactions

3.1 Introduction

Chalcogen bonding has emerged as a key noncovalent interaction with several applications including supramolecular chemistry,[1] biochemistry[2] and catalysis.[3] The chalcogen-bond (ChB) is defined as the net-attractive noncovalent interaction, in a $D_2Ch\bullet\bullet\bullet A$ complex, between a chalcogen-bond donor D_2Ch, a Lewis-acid, and a chalcogen-bond acceptor A^- (or A), a Lewis-base, in which Ch stands for a chalcogen atom, i.e., an atom of group 16 (Scheme 3.1).[4a] The "σ-hole interaction" between a positive region on the electrostatic potential surface on the chalcogen atom and a negatively charged density on the ChB acceptor is usually invoked to characterize the ChB.[4] Despite this, recent studies have shown that the strength of the ChB is, instead, correlated to the electron-accepting capacity of the σ*-type LUMO of the chalcogen molecule.[5] The debate over the origin and fundamental bonding mechanism of the ChB continues to stimulate much interest in the literature.

Density functional theory (DFT) based Kohn-Sham molecular orbital analysis has been paramount for our understanding of bonding mechanisms and the nature of chemical phenomena.[6] Selection of the appropriate density functional approximation to investigate chalcogen bonding is critical to ensure trust-worthy results, but unfortunately this is not entirely straightforward, as the question of which approximate functional works best is highly dependent on the property and system of interest.

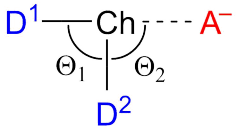

Scheme 3.1. Chalcogen-bonded $D_2Ch\bullet\bullet\bullet A^-$ model complexes (Ch = S, Se; D, A = F, Cl).

The first purpose of this work is to provide a detailed benchmark study of high-level relativistic *ab initio* methods and focus on the investigation of ChB, using the D_2Ch molecules as chalcogen-bond donors and the halides A^- as chalcogen-bond acceptors (see Scheme 3.1). Our model complexes systematically varies the substituent (D), the chalcogen atom (Ch), the acceptor (A^-), and is the perfect archetype for strongly bound chalcogen systems studied experimentally.[2a,3c] This is done by computing the $D_2Ch\bullet\bullet\bullet A^-$ complexation energies ΔE for the first time in a procedure involving both a hierarchical series of *ab initio* methods [HF, MP2, CCSD, and CCSD(T)][7] in combination with a hierarchical series of Gaussian-type basis sets

of increasing flexibility, polarization (up to *g* functions), and diffuseness, thereby eclipsing the two other benchmarks based on a single-shot CCSD(T) approach.[7i,7j] Interestingly, the predictions of ΔE by both benchmarks for the same systems can differ by up to 10 kcal mol^{-1}. The basis set superposition error (BSSE) has been accounted for through the counterpoise correction (CPC) of Boys and Bernardi.[8]

The second purpose of this work is to evaluate the performance of 13 different density functionals in combination with ADF's Slater-type QZ4P basis set (*vide infra*) for predicting the ChB energy ΔE against our best *ab initio* benchmark. Thus, we perform an extensive analysis to highlight the importance of diffuse and polarization functions in the basis set, the role of the BSSE, and the necessity of Coulomb correlation as well as the extent to which the approach has converged with respect to the level of correlation treatment and basis set quality. Our analyses identify the B3LYP and M06-2X functionals, along with the M06 DFT approach as appropriate and computationally efficient alternatives to expensive high-level *ab initio* computations of chalcogen-bonded complexes.

3.2 Methods

Ab Initio Geometries and Energies

All *ab initio* calculations were carried out using ORCA.[9] The atomic orbitals were described by the all-electron scalar relativistically contracted variants of Gaussian-type def2-XVP(P) (X = S, TZ, QZ) basis sets with polarization functions (up to *g* functions) in the series BS1 to BS3 (see Table 3.1).[10] The series BS1+ to BS3+ result from BS1 to BS3 after adding extra *s* and *p* minimally augmented (ma) diffuse functions (see Table 3.1).[10c] For each of the six basis sets (BS#), the equilibrium geometry was computed using coupled-cluster singles and doubles with perturbative triples, i.e., at CCSD(T)/BS#.[11] Then, for each BS# and corresponding CCSD(T)/BS# geometry, energies were evaluated along the following hierarchical series of quantum chemical methods: Hartree-Fock theory (HF/BS#), second-order Møller-Plesset perturbation theory (MP2/BS#),[12] coupled-cluster with single and double excitations (CCSD/BS#)[13] and CCSD(T)/BS#.[11] The scalar relativistic effects were accounted for using the scalar zeroth-order regular approximation (ZORA).[14] Inclusion of relativistic effects are necessary for heavier chalcogen-bonded systems and without ZORA, our counterpoise-corrected complexation energies ΔE_{CPC} are significantly under-bound. For example, for $Cl_2Se{\bullet\bullet\bullet}Cl^-$ the ΔE_{CPC} is –31.2 kcal mol^{-1} at CCSD(T)/BS3+ and –34.3 kcal mol^{-1} at ZORA-CCSD(T)/BS3+. For the lighter chalcogen systems, such as $F_2S{\bullet\bullet\bullet}F^-$, this effect is

smaller and ΔE_{CPC} is –45.1 kcal mol^{-1} at CCSD(T)/BS3+ and –45.2 kcal mol^{-1} at ZORA-CCSD(T)/BS3+.

Table 3.1. Number of relativistically contracted basis functions for ZORA-def2- basis sets without (BS) and with (BS+) diffuse functions for F, S, Cl and Se elements.

Basis set	Label	F	S and Cl	Se
ZORA-def2-SVP	BS1	3s2p1d	6s3p1d	9s6p3d
ZORA-def2-TZVPP	BS2	6s3p2d1f	8s4p3d1f	10s8p4d1f
ZORA-def2-QZVPP	BS3	8s4p3d2f1g	11s7p4d2f1g	14s11p4d4f1g
ma-ZORA-def2-SVP	BS1+	4s3p1d	7s4p1d	10s7p3d
ma-ZORA-def2-TZVPP	BS2+	7s4p2d1f	9s5p3d1f	11s9p4d1f
ma-ZORA-def2-QZVPP	BS3+	9s5p3d2f1g	12s8p4d2f1g	15s12p4d4f1g

DFT Geometries and Energies

All DFT calculations were carried out using the Amsterdam Density Functional (ADF) program.[15] The equilibrium geometries and energies of chalcogen-bonded complexes were computed at different DFT levels using (i) the GGA based functionals: PBE,[16] BP86,[17] and BLYP;[17a,18] (ii) the hybrid functionals: B3LYP[19] and BHANDH (50% HF exchange, 50% LDA exchange, and 100% LYP correlation[18]); (iii) the meta-GGA based functionals: SSB-D[20] and M06-L;[21] (iv) the meta-hybrid functionals: M06,[21] M06-2X,[21] and M06-HF.[21] The long range dispersion corrections were included into the B3LYP, BLYP, and SSB-D functionals with Grimme's empirical D3 correction using the Becke-Johnson (BJ) damping function.[22] Energies and geometries were computed for each of the various DFT approaches with the QZ4P basis set.[23] This is a large, uncontracted and relativistically optimized, all-electron (i.e., no frozen core approximation) basis set of Slater-type orbitals (STOs), which is of quadruple-ζ quality for all atoms and has been augmented with the following sets of polarization and diffuse functions: two 3*d* and two 4*f* on fluorine, three 3*d* and two 4*f* on sulfur and chlorine, two 4*d* and three 4*f* on selenium. The molecular density was fitted by the systematically improvable ZLM fitting scheme. Scalar relativistic effects were accounted for using the zeroth-order regular approximation (ZORA).[14]

3.3 Results and Discussion

Ab Initio Geometries

First, we examine the equilibrium geometries of $D_2Ch{\bullet\bullet\bullet}A^-$ complexes (Ch = S, Se; D, A = F, Cl) which were fully optimized at the ZORA-CCSD(T) level along with a hierarchic series of Gaussian-type basis sets both with and without diffuse functions (see Table 3.1). The isolated halide and C_{2v} symmetric D_2Ch neutral fragment form the stable T-shaped, chalcogen-bonded complexes $D_2Ch{\bullet\bullet\bullet}A^-$ which are of C_{2v} (D = A) or C_s symmetry (D ≠ A) (see Figure 3.1). All species have been verified through a vibrational analysis to represent equilibrium structures (no imaginary frequencies). Thus, we have a set of geometries that have been optimized at the same relativistic *ab initio* level along with each basis set considered in this work, without any structural or symmetry constraint (for complete structural details, see Appendices 3.1 and 3.2).

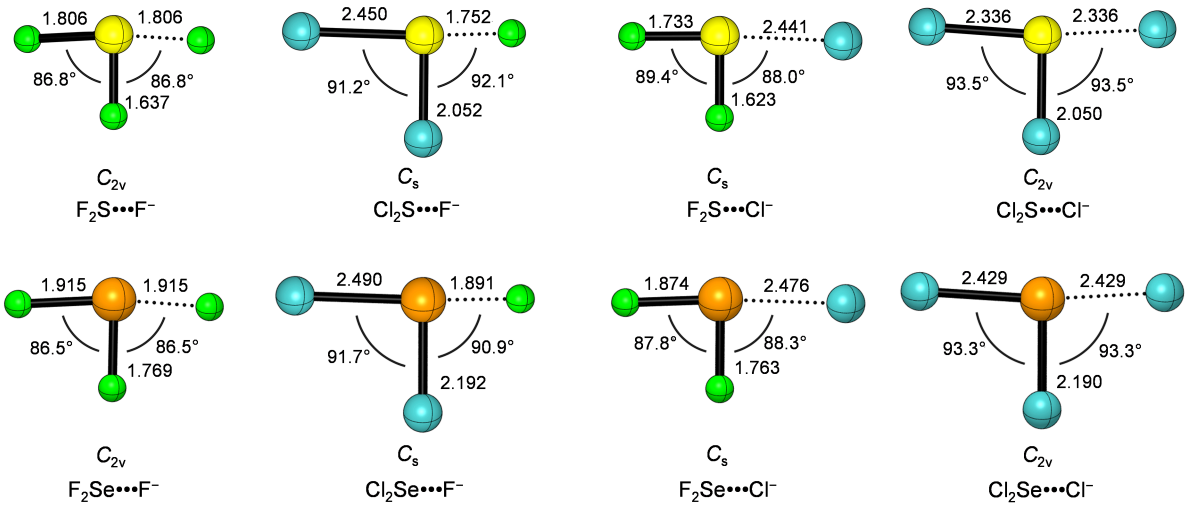

Figure 3.1. Geometries (in Å and degrees) and point group symmetries of $D_2Ch{\bullet\bullet\bullet}A^-$ complexes computed at ZORA-CCSD(T)/BS3+.

The chalcogen bond distance in the $D_2Ch{\bullet\bullet\bullet}A^-$ complexes become longer as the chalcogen atom (Ch) varies from S to Se and as the accepting halide (A^-) varies from F^- to Cl^-, and shorter as the substituent D varies from F to Cl (see Figure 1). Furthermore, the Θ_1 and Θ_2 angles (see Scheme 3.1) are slightly smaller than 90° for D = F and slightly larger than 90° for D = Cl. The key structural parameters (chalcogen bond distance and angles) converge faster as a function of basis-set flexibility and polarization if diffuse functions are included in the basis set. For example, chalcogen bond lengths converge within 0.004–0.015 Å along the BS1 to BS3 series and within 0.000–0.010 Å along the BS1+ to BS3+ series (see Appendices 3.1 and 3.2).

Interestingly, the differences in bond distances and angles of the $D_2Ch{\bullet\bullet\bullet}A^-$ complexes between using quadruple-ζ basis sets basis sets with (BS3+) or without diffuse functions (BS3) are small, only ca. 0.001 Å and 0.1°. In the following, all ZORA-CCSD(T) calculated geometries are used in the series of high-level *ab initio* calculations that constitute our benchmark study of chalcogen bonds (ChB) complexation energies.

Ab Initio Chalcogen Bond Energies

Here, we report the first systematic investigation of the complexation energies, with (ΔE_{CPC}) and without (ΔE) counterpoise corrections, as a function of a hierarchical series of *ab initio* methods and basis sets. The results of our *ab initio* computations are collected in Tables 3.2–3.5 (ΔE_{CPC}, ΔE, and BSSE) and graphically displayed in Figures 3.2–3.5 (ΔE_{CPC} and BSSE). In general, we find that the same trends in chalcogen-bond strengths emerge at all levels of theory, that is, chalcogen bonds become stronger as the chalcogen Ch varies from S to Se, the halide A^- varies from Cl^- to F^-, and the substituents D from F to Cl (see Figure 3.2). Our best reference data, obtained using counterpoise-corrected ZORA-CCSD(T)/BS3+ energies, show that the $D_2Ch{\bullet\bullet\bullet}A^-$ chalcogen-bond strength increases along $F_2S{\bullet\bullet\bullet}F^-$ to $F_2Se{\bullet\bullet\bullet}F^-$ from –45.2 to –56.4 kcal mol^{-1} and along $F_2Se{\bullet\bullet\bullet}Cl^-$ to $F_2Se{\bullet\bullet\bullet}F^-$ from –31.6 to –56.4 kcal mol^{-1}. On the other hand,

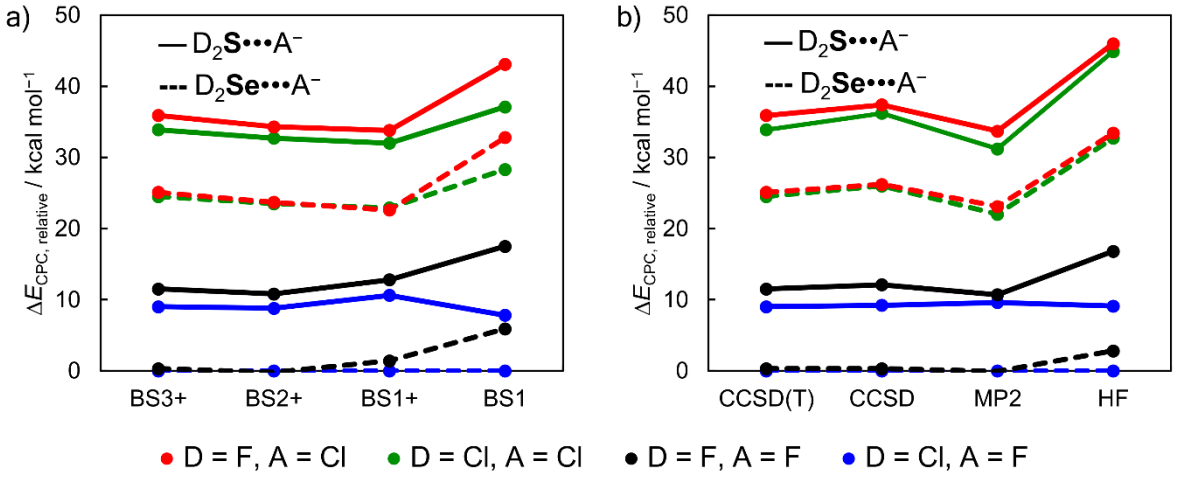

Figure 3.2. Trends in $D_2Ch{\bullet\bullet\bullet}A^-$ chalcogen-bond strength relative to the most stable $Cl_2Se{\bullet\bullet\bullet}F^-$ complex along a) ZORA-CCSD(T)/BS# and b) ZORA-method/BS3+. Sulfur complexes in full lines and selenium complexes in dashed lines.

along $F_2S{\bullet\bullet\bullet}Cl^-$ to $Cl_2S{\bullet\bullet\bullet}Cl^-$, the chalcogen-bond strength only marginally strengthens from –20.8 to –22.8 kcal mol^{-1}. For smaller basis sets in combination with ZORA-CCSD(T), this minor difference in stability along the variation on the substituent D becomes even smaller and,

for BS1+ basis sets, the selenium bonds $D_2Se{\bullet\bullet\bullet}F^-$ become marginally stronger for D = F. Our best level ZORA-CCSD(T)/BS3+ has converged within 1.5–3.1 kcal mol^{-1} in respect to the basis set series and, in combination with the BS3+ basis set, ΔE_{CPC} have converged within 1.1–3.4 kcal mol^{-1} along the series of *ab initio* methods.

Table 3.2. Complexation energies (in kcal mol^{-1}) of $D_2S{\bullet\bullet\bullet}A^-$ chalcogen-bonded complexes with (ΔE_{CPC}) and without (ΔE) counterpoise corrections.[a]

		$F_2S{\bullet\bullet\bullet}F^-$		$F_2S{\bullet\bullet\bullet}Cl^-$		$Cl_2S{\bullet\bullet\bullet}F^-$		$Cl_2S{\bullet\bullet\bullet}Cl^-$	
Method	**Basis set**	ΔE_{CPC}	ΔE	ΔE_{CPC}	ΔE	ΔE_{CPC}	ΔE	ΔE_{CPC}	ΔE
HF	BS1	–45.0	–63.3	–15.6	–21.9	–60.0	–78.7	–20.3	–27.5
	BS2	–39.7	–42.7	–10.6	–12.0	–47.1	–50.2	–11.7	–13.3
	BS3	–38.1	–39.3	–8.7	–9.0	–45.9	–47.1	–9.8	–10.1
MP2	BS1	–46.3	–72.8	–19.8	–28.9	–56.1	–84.0	–25.9	–36.9
	BS2	–47.6	–54.8	–23.0	–26.0	–49.0	–56.8	–25.4	–28.9
	BS3	–47.2	–50.8	–23.0	–24.2	–48.5	–52.5	–25.6	–27.1
CCSD	BS1	–44.0	–70.0	–18.2	–27.5	–54.0	–81.1	–23.2	–34.2
	BS2	–44.6	–51.0	–18.9	–21.7	–47.5	–54.4	–20.1	–23.4
	BS3	–44.7	–47.7	–18.6	–19.6	–47.8	–51.1	–19.9	–21.0
CCSD(T)	BS1	–44.5	–71.4	–18.9	–28.5	–54.2	–82.4	–24.9	–36.3
	BS2	–46.3	–53.5	–21.0	–24.2	–48.8	–56.5	–23.0	–26.7
	BS3	–46.6	–50.2	–21.1	–22.3	–49.3	–53.2	–23.3	–24.7
HF	BS1+	–37.0	–39.5	–11.2	–12.5	–46.9	–49.6	–12.9	–14.2
	BS2+	–37.3	–37.5	–8.5	–8.6	–44.7	–44.9	–9.4	–9.6
	BS3+	–37.4	–37.4	–8.2	–8.2	–45.1	–45.1	–9.3	–9.3
MP2	BS1+	–40.1	–46.0	–19.1	–23.8	–41.6	–48.9	–21.0	–26.3
	BS2+	–43.6	–46.4	–21.2	–23.0	–44.4	–47.4	–23.3	–25.4
	BS3+	–45.6	–47.2	–22.6	–23.5	–46.7	–48.4	–25.1	–26.1
CCSD	BS1+	–38.0	–44.0	–16.6	–21.3	–40.8	–48.0	–17.5	–22.8
	BS2+	–41.4	–44.0	–17.1	–18.8	–43.9	–46.7	–17.9	–19.8
	BS3+	–43.5	–44.8	–18.2	–19.0	–46.4	–47.8	–19.4	–20.2
CCSD(T)	BS1+	–39.1	–45.6	–18.1	–23.1	–41.3	–49.1	–19.9	–25.5
	BS2+	–42.8	–45.8	–19.3	–21.4	–44.8	–48.1	–20.9	–23.2
	BS3+	–45.2	–46.9	–20.8	–21.7	–47.7	–49.5	–22.8	–23.8

[a] Computed at ZORA-Method/BS#//ZORA-CCSD(T)/BS#.

Table 3.3. Complexation energies (in kcal mol^{-1}) of $D_2Se{\bullet\bullet\bullet}A^-$ chalcogen-bonded complexes with (ΔE_{CPC}) and without (ΔE) counterpoise corrections.[a]

		$F_2Se{\bullet\bullet\bullet}F^-$		$F_2Se{\bullet\bullet\bullet}Cl^-$		$Cl_2Se{\bullet\bullet\bullet}F^-$		$Cl_2Se{\bullet\bullet\bullet}Cl^-$	
Method	**Basis set**	ΔE_{CPC}	ΔE	ΔE_{CPC}	ΔE	ΔE_{CPC}	ΔE	ΔE_{CPC}	ΔE
HF	BS1	–58.5	–78.5	–26.5	–34.1	–66.9	–86.7	–31.0	–38.8
	BS2	–53.4	–56.8	–23.1	–24.8	–56.0	–59.6	–23.7	–25.6
	BS3	–52.1	–53.3	–21.2	–21.6	–55.0	–56.3	–22.0	–22.4
MP2	BS1	–57.6	–86.6	–30.2	–41.4	–64.1	–93.3	–35.1	–47.0
	BS2	–57.8	–65.7	–33.3	–36.9	–58.0	–66.3	–34.5	–38.4
	BS3	–57.9	–61.4	–33.6	–34.8	–58.1	–61.9	–34.9	–36.3
CCSD	BS1	–55.9	–84.1	–28.7	–40.0	–61.7	–90.1	–32.6	–44.5
	BS2	–55.9	–62.8	–29.8	–33.2	–56.2	–63.5	–30.0	–33.7
	BS3	–56.4	–59.3	–29.8	–30.8	–57.0	–60.1	–30.2	–31.3
CCSD(T)	BS1	–56.1	–85.3	–29.2	–40.9	–62.0	–91.4	–33.7	–46.0
	BS2	–56.9	–64.7	–31.5	–35.3	–57.3	–65.5	–32.2	–36.3
	BS3	–57.7	–61.2	–31.9	–33.0	–58.4	–62.1	–32.8	–34.1
HF	BS1+	–51.8	–54.1	–23.0	–24.2	–54.8	–57.0	–24.7	–25.9
	BS2+	–51.1	–51.3	–21.0	–21.1	–53.6	–53.8	–21.5	–21.6
	BS3+	–51.4	–51.4	–20.8	–20.8	–54.2	–54.2	–21.5	–21.5
MP2	BS1+	–52.7	–58.4	–30.6	–35.6	–51.4	–57.5	–30.6	–36.0
	BS2+	–54.2	–56.8	–31.7	–33.6	–53.8	–56.6	–32.4	–34.6
	BS3+	–56.4	–57.8	–33.2	–34.1	–56.3	–57.8	–34.3	–35.3
CCSD	BS1+	–51.2	–56.8	–28.0	–33.0	–50.0	–56.0	–27.5	–32.9
	BS2+	–52.9	–55.4	–28.1	–29.9	–52.8	–55.5	–27.9	–29.9
	BS3+	–55.3	–56.5	–29.4	–30.1	–55.6	–56.8	–29.6	–30.4
CCSD(T)	BS1+	–51.9	–58.0	–29.3	–34.7	–50.5	–57.1	–29.0	–34.8
	BS2+	–53.8	–56.7	–29.9	–32.1	–53.6	–56.7	–30.1	–32.5
	BS3+	–56.4	–57.9	–31.6	–32.4	–56.7	–58.3	–32.2	–33.2

[a] Computed at ZORA-Method/BS#//ZORA-CCSD(T)/BS#.

Despite the trend in $D_2Ch{\bullet\bullet\bullet}A^-$ chalcogen-bond strength being qualitatively the same at all levels of *ab initio* theory in our double hierarchical series (in QM method and in basis set), major variations of up to ca. 20 kcal mol^{-1} in absolute values are observed between the various levels (see Tables 3.2 and 3.3). For example, with $Cl_2S{\bullet\bullet\bullet}F^-$ the ΔE_{CPC} varies from –60.0 to –49.6 kcal mol^{-1} at both ZORA-HF/BS1 and ZORA-CCSD(T)/BS3+ levels, respectively. The high accuracy of our best level ZORA-CCSD(T)/BS3+ can be attributed to four main factors: (i) inclusion of additional *s* and *p* diffuse functions to accurately describe anions, as one would expect; (ii) use of a highly flexible basis set with diffuse functions to minimize BSSE; (iii) introduction of Coulomb correlation; and (iv) inclusion of polarization functions especially for highly correlated methods.

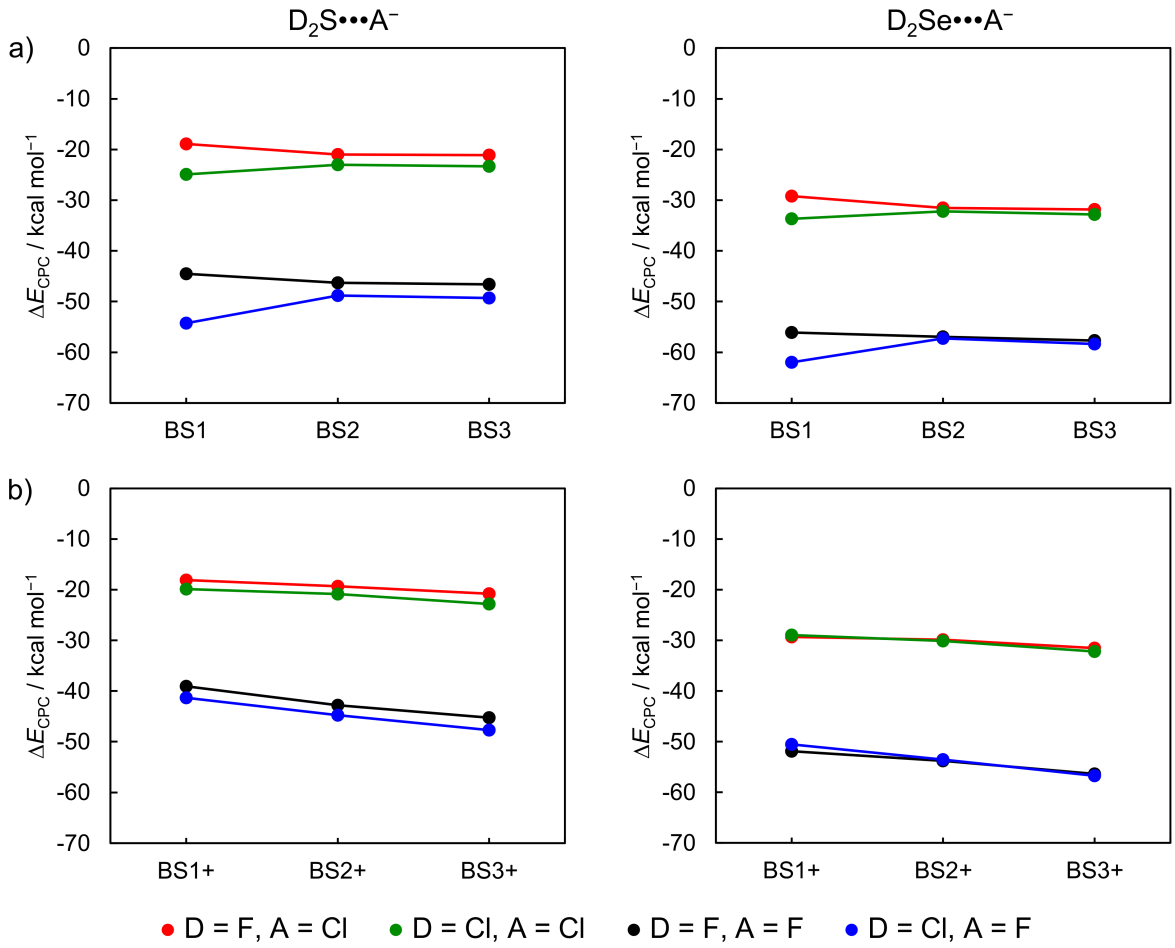

Figure 3.3. Counterpoise-corrected ZORA-CCSD(T) complexation energies (ΔE_{CPC}) for $D_2Ch•••A^-$ chalcogen-bonded complexes along a) BS1 to BS3 and b) BS1+ to BS3+ basis sets.

We first examine ΔE_{CPC} as a function of the basis set. In general, a strengthening of the $D_2Ch•••A^-$ chalcogen bond occurs as the flexibility of the basis set is increased, and ΔE_{CPC} is only converged at larger basis sets (see Figure 3.3). An exception to this trend is observed for ChB ΔE_{CPC} values computed with the small basis set BS1, which lacks diffuse functions. For example, the ΔE_{CPC} for $Cl_2Se•••F^-$ that is already –62.0 kcal mol^{-1} at ZORA-CCSD(T)/BS1 slightly weakens to –58.4 kcal mol^{-1} at ZORA-CCSD(T)/BS3 (see Figure 3.3a), whereas the ΔE_{CPC} is –50.5 kcal mol^{-1} at ZORA-CCSD(T)/BS1+ and strengthens to –56.7 kcal mol^{-1} at ZORA-CCSD(T)/BS3+ (see Figure 3.3b). This is caused by the breathing orbitals of the anionic halide fragments going from diffuse in the isolated anion to more compact upon forming the ChB complex, which leads to charge delocalization over the molecular system.[24a,25] In the absence of diffuse functions, the complexation energy is overestimated due to the artificially high energy of the anion because the charge density cannot breath, i.e., expand, in order to relieve electron–electron repulsion in the negatively charged species. This explains the possibly

misleading conclusion that the ΔE_{CPC} converges faster along the BS1 to BS3 series compared to the BS1+ to BS3+ series and, therefore, the use of the basis set series without diffuse functions would be more appropriate. Later on, we illustrate that this is only a consequence of these complexation energies being 'corrected' by the BSSE.

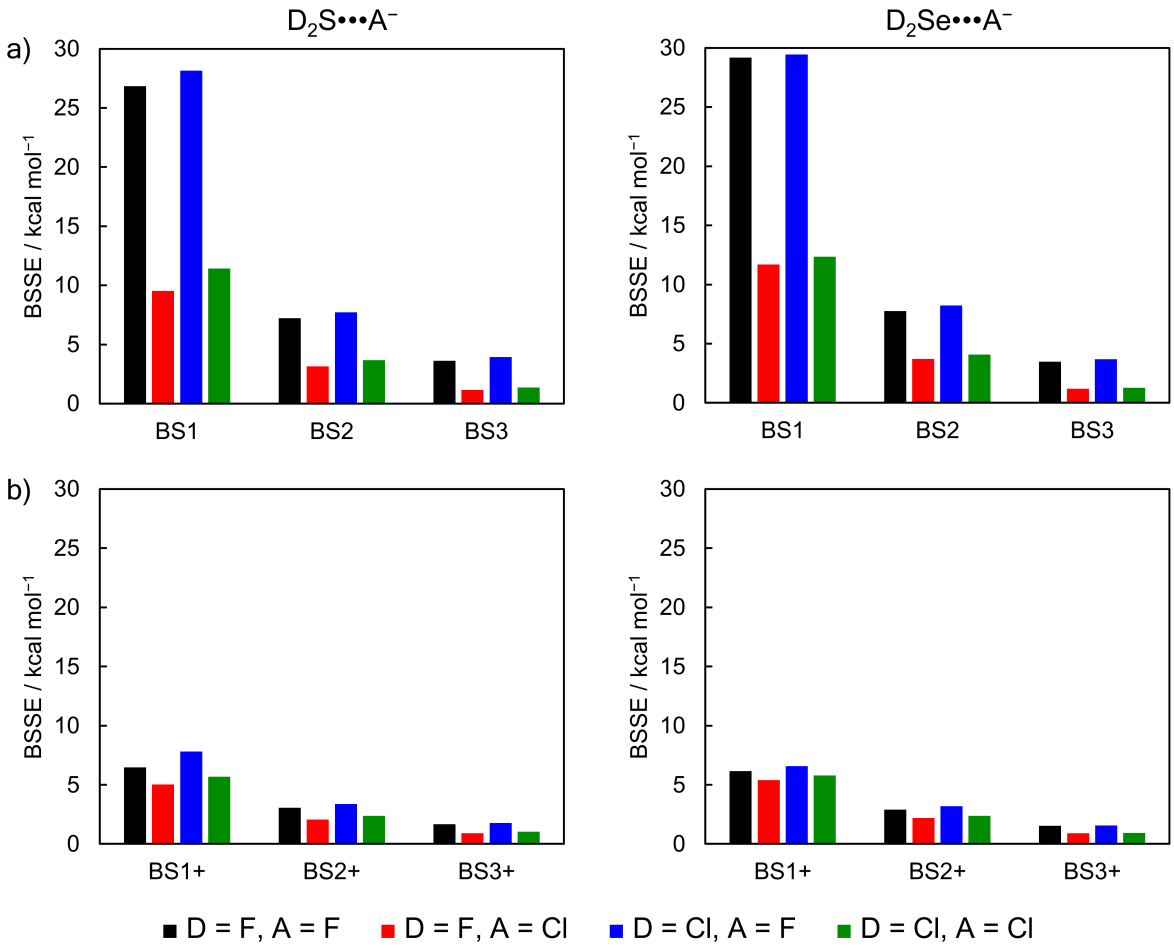

Figure 3.4. Basis set superposition error (BSSE) calculated at ZORA-CCSD(T) level for $D_2Ch•••A^-$ chalcogen-bonded complexes along a) BS1 to BS3 and b) BS1+ to BS3+ basis sets.

The BSSE becomes significantly smaller with the addition of diffuse functions and decreases from 1.2–3.9 kcal mol^{-1} at ZORA-CCSD(T)/BS3 to 0.9–1.8 kcal mol^{-1} at ZORA-CCSD(T)/BS3+ (see Tables 3.4 and 3.5). However, the BSSE is large, in particular, for highly correlated methods and smaller basis sets without diffuse functions, that is, at the ZORA-CCSD(T)/BS1 level (see Figure 3.4). As a result, the ZORA-CCSD(T) ΔE_{CPC} are better for the BS1+ to BS3+ series but become similar to the series without diffuse functions as the BSSE simultaneously decreases as the basis sets size increases. Both basis sets series, indeed, converge to a similar value independently of the number of diffuse functions, but this result is

fortuitous due to the BSSE correction that damps any fluctuations along the BS1 to BS3 series. In fact, the uncorrected ZORA-CCSD(T) complexation energies ΔE converges significantly faster along the BS1+ to BS3+ series (within 0.3–1.5 kcal mol^{-1}) compared to the BS1 to BS3 series (within 1.9–3.5 kcal mol^{-1}) (see Tables 3.2 and 3.3). This is, again, due to the poor description of the anionic reactants by basis sets without diffuse functions. This effect is particularly apparent at HF where Coulomb correlation is absent, mainly for systems involving the compact atom F^-.[24a] For example, the ΔE for $Cl_2Se{\bullet\bullet\bullet}F^-$ that is –86.7 kcal mol^{-1} at ZORA-HF/BS1 significantly weakens to –57.0 kcal mol^{-1} at ZORA-HF/BS1+, whereas, for $Cl_2Se{\bullet\bullet\bullet}Cl^-$, the ΔE is –38.8 kcal mol^{-1} at ZORA-HF/BS1 and weakens to –25.9 kcal mol^{-1} at ZORA-HF/BS1+ (see Table 3.3).

Table 3.4. Basis set superposition error (BSSE, in kcal mol^{-1}) of $D_2S{\bullet\bullet\bullet}A^-$ chalcogen-bonded complexes.[a]

Method	Basis set	$F_2S{\bullet\bullet\bullet}F^-$	$F_2S{\bullet\bullet\bullet}Cl^-$	$Cl_2S{\bullet\bullet\bullet}F^-$	$Cl_2S{\bullet\bullet\bullet}Cl^-$
HF	BS1	18.3	6.3	18.7	7.3
	BS2	3.0	1.4	3.1	1.5
	BS3	1.1	0.3	1.2	0.4
MP2	BS1	26.6	9.1	27.9	10.9
	BS2	7.3	3.0	7.8	3.5
	BS3	3.7	1.2	4.0	1.4
CCSD	BS1	25.9	9.2	27.1	11.0
	BS2	6.4	2.8	6.9	3.3
	BS3	3.0	1.0	3.3	1.1
CCSD(T)	BS1	26.8	9.5	28.1	11.4
	BS2	7.2	3.2	7.7	3.7
	BS3	3.6	1.2	3.9	1.4
HF	BS1+	2.5	1.3	2.7	1.3
	BS2+	0.2	0.1	0.2	0.1
	BS3+	0.0	0.0	0.0	0.0
MP2	BS1+	5.9	4.7	7.3	5.3
	BS2+	2.7	1.9	3.0	2.1
	BS3+	1.6	0.9	1.7	1.1
CCSD	BS1+	6.0	4.7	7.2	5.3
	BS2+	2.6	1.7	2.8	2.0
	BS3+	1.3	0.7	1.4	0.8
CCSD(T)	BS1+	6.5	5.0	7.8	5.7
	BS2+	3.0	2.1	3.4	2.4
	BS3+	1.7	0.9	1.8	1.0

[a] Computed at ZORA-Method/BS#//ZORA-CCSD(T)/BS#.

Table 3.5. Basis set superposition error (BSSE, in kcal mol^{-1}) of $D_2Se{\bullet\bullet\bullet}A^-$ chalcogen-bonded complexes.[a]

Method	Basis set	$F_2Se{\bullet\bullet\bullet}F^-$	$F_2Se{\bullet\bullet\bullet}Cl^-$	$Cl_2Se{\bullet\bullet\bullet}F^-$	$Cl_2Se{\bullet\bullet\bullet}Cl^-$
HF	BS1	20.0	7.6	19.8	7.8
	BS2	3.4	1.7	3.6	1.9
	BS3	1.1	0.4	1.2	0.4
MP2	BS1	29.0	11.2	29.2	11.8
	BS2	7.8	3.5	8.3	3.9
	BS3	3.5	1.2	3.8	1.3
CCSD	BS1	28.2	11.3	28.4	11.9
	BS2	6.9	3.3	7.3	3.7
	BS3	2.9	1.0	3.1	1.1
CCSD(T)	BS1	29.2	11.7	29.5	12.3
	BS2	7.8	3.7	8.2	4.1
	BS3	3.5	1.2	3.7	1.3
HF	BS1+	2.3	1.2	2.2	1.2
	BS2+	0.2	0.1	0.3	0.2
	BS3+	0.0	0.0	0.0	0.0
MP2	BS1+	5.7	5.0	6.1	5.4
	BS2+	2.6	2.0	2.9	2.2
	BS3+	1.4	0.9	1.5	1.0
CCSD	BS1+	5.7	5.1	6.0	5.4
	BS2+	2.4	1.8	2.7	2.0
	BS3+	1.2	0.7	1.2	0.7
CCSD(T)	BS1+	6.1	5.4	6.6	5.8
	BS2+	2.9	2.2	3.2	2.4
	BS3+	1.5	0.9	1.6	0.9

[a] Computed at ZORA-Method/BS#//ZORA-CCSD(T)/BS#.

Lastly, inclusion of Coulomb correlation is critical to achieve accurate chalcogen-bond energies. At HF, the $D_2Ch{\bullet\bullet\bullet}A^-$ complexes are weakly bound and enter into stronger chalcogen bonds as Coulomb correlation is introduced (see Figure 3.5). For example, from HF to CCSD(T), the ΔE_{CPC} for $F_2S{\bullet\bullet\bullet}F^-$ strengthens from –38.1 to –46.6 kcal mol^{-1} for BS3 and from –37.4 to –45.2 kcal mol^{-1} for BS3+ (see Table 3.2). We also note that the stabilization of ΔE_{CPC} due to the increasing of basis set size is more pronounced for high correlated methods. For example, from BS1+ to BS3+, the ΔE_{CPC} for $F_2Se{\bullet\bullet\bullet}F^-$ slightly varies from –51.8 to –51.4 kcal mol^{-1} at HF level and strengthens from –51.9 to –56.4 kcal mol^{-1} at CCSD(T) level (see Tables 3.2 and 3.3). This is due to the well-known fact that correlated *ab initio* methods strongly depend on the extent of polarization functions to generate configurations through which the wavefunction can describe the correlation hole.[7c] On the other hand, at the HF level without Coulomb correlation, there is much less sensitivity of ΔE_{CPC} towards increasing the flexibility and polarization functions of the basis set. Taken altogether, our benchmark approach, based

on hierarchical series, reveals that our best estimates are converged with regards to correlation and basis set within 1.1–3.4 kcal mol^{-1} and 1.5–3.1 kcal mol^{-1}, respectively, and provides the most accurate benchmark to date, surpassing the recently published benchmark based on a single-shot CCSD(T) approach.[7i] In the next section, we discuss the ability of DFT to describe Coulomb correlation compared to our ZORA-CCSD(T)/BS3+ benchmark.

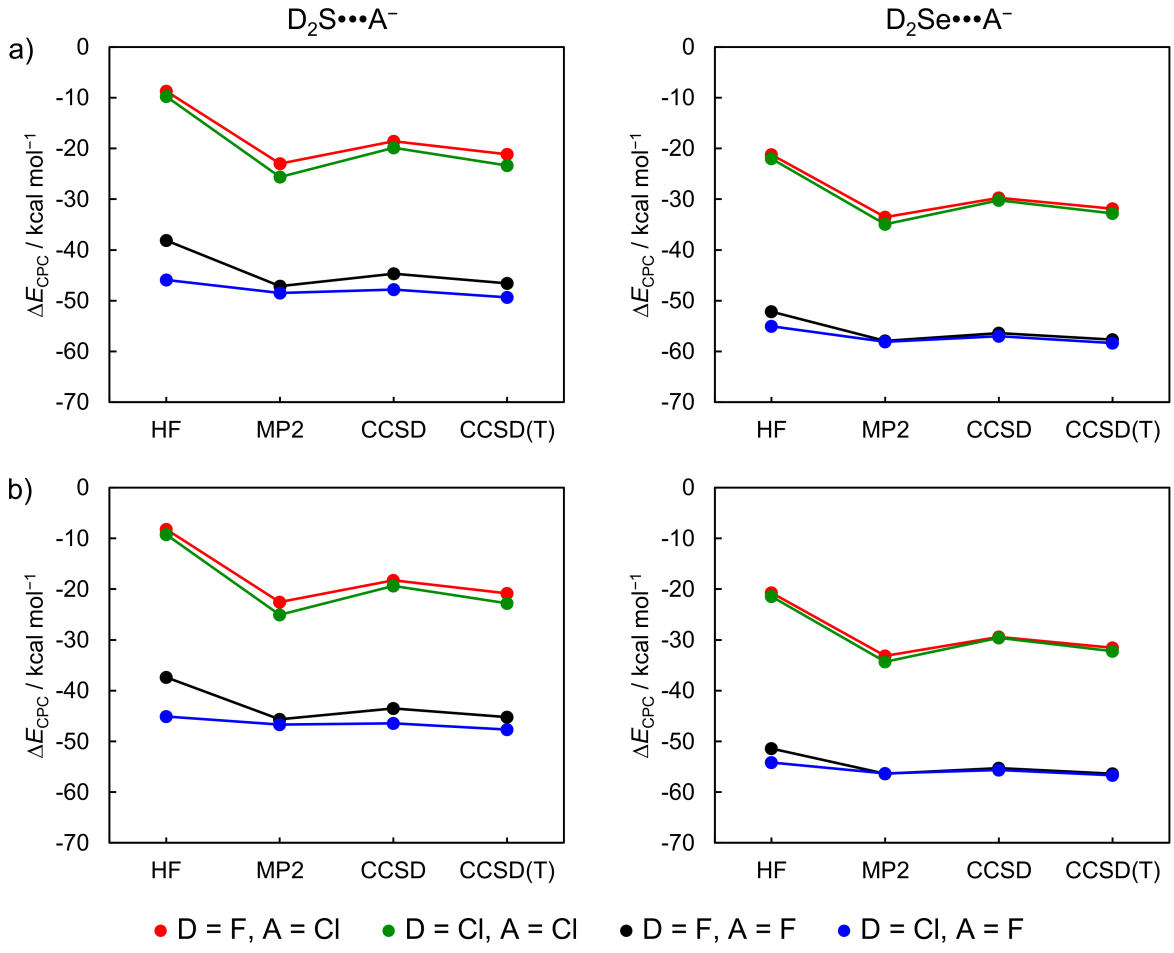

Figure 3.5. Counterpoise-corrected ZORA-CCSD(T) complexation energies (ΔE_{CPC}) for $D_2Ch•••A^-$ chalcogen-bonded complexes along the ab initio method in combination with a) BS3 and b) BS3+.

Performance of Density Functional Approximations

Finally, we have computed the complexation energies ΔE for various GGAs, meta-GGAs, hybrid, and meta-hybrid functionals in combination with the all-electron QZ4P basis set and ZORA for relativistic effects on optimized geometries at the same level. The performance of the density functionals is discussed by comparing the resulting ΔE with our best *ab initio* ZORA-CCSD(T)/BS3+ level. These results are graphically illustrated by the bar diagrams in

Figure 3.6 (mean absolute error, mean error, and largest deviation) and collected in Appendices 3.3 and 3.4 (complexation energies, mean absolute error, mean error, and largest deviation).

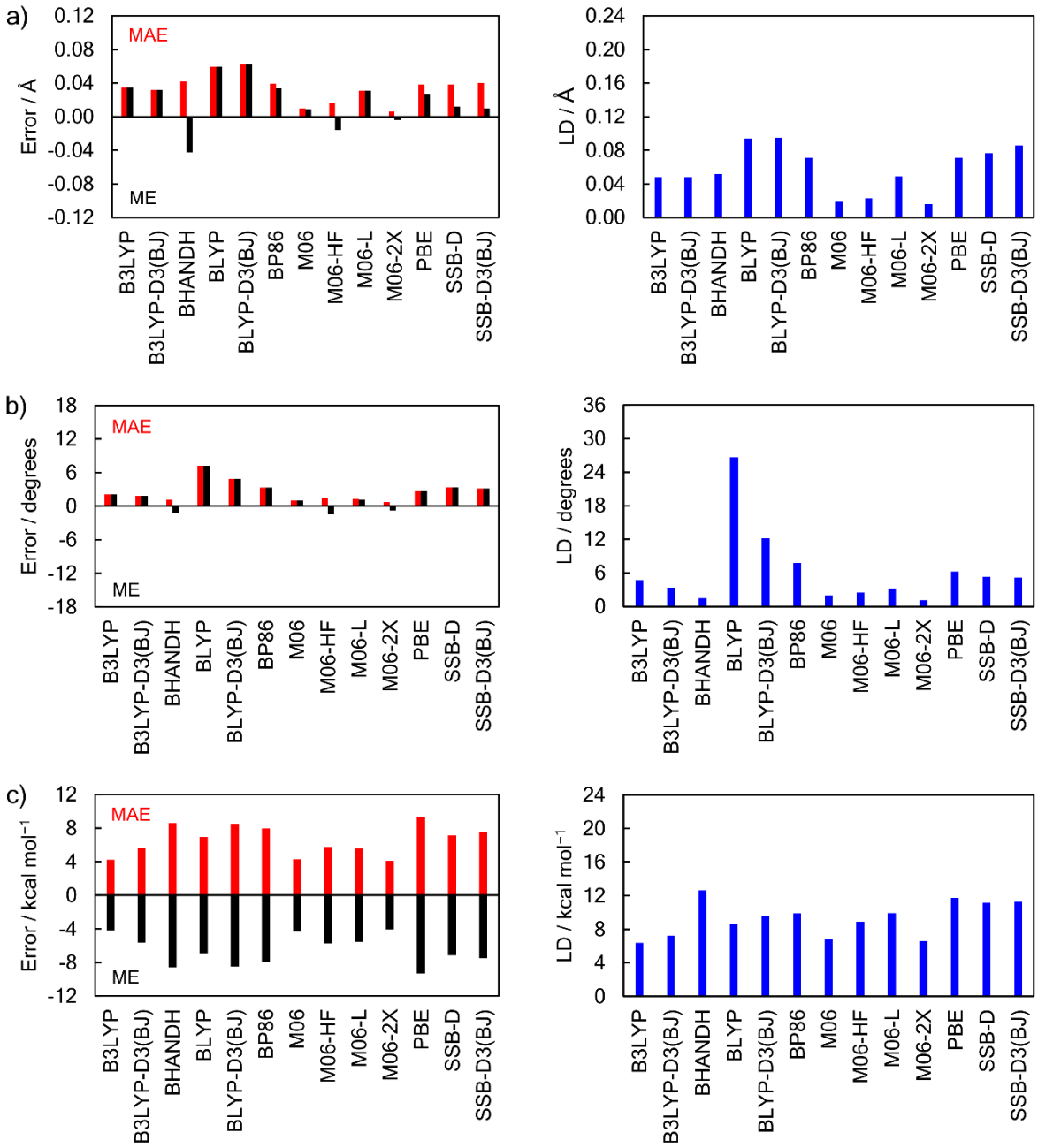

Figure 3.6. Mean absolute error (MAE, red), mean error (ME, black), and largest deviation (LD, blue) of the ZORA-DFT/QZ4P functionals relative to the ZORA-CCSD(T)/BS3+ a) Ch•••A^- bond lengths, b) bond angles Θ_2, and c) D_2Ch•••A^- counterpoise-corrected complexation energies.

The ΔE computed at the DFT levels follow the same trends as those at ZORA-CCSD(T)/BS3+, that is, chalcogen bonds D_2Ch•••A^- become stronger as the chalcogen Ch

varies from S to Se, the halide A^- varies from Cl^- to F^- and the substituents D from F to Cl. SSB-D and SSB-D3(BJ) are exceptions, whereby the ChB becomes more stabilizing when D varies from Cl to F (see Appendix 3.3). The main trends in bond lengths and angles are also in line with the *ab initio* methods where the $D_2Ch{\bullet\bullet\bullet}A^-$ chalcogen bond becomes longer as Ch varies from S to Se and as A^- varies from F^- to Cl^- and shorter as D varies from F to Cl (see Appendices 3.5 and 3.6). In general, we find that the density functionals give longer chalcogen bonds and bigger bond angles Θ_2 (Scheme 3.1) compared to our best level ZORA-CCSD(T)/BS3+ geometries (see Figure 3.6). The best overall agreement with our best *ab initio* level geometries is with the meta-hybrid M06, M06-HF, M06-2X functionals (MAE of 0.006–0.017 Å for bond lengths and MAE of 0.7–1.5 degrees for bond angles). The GGAs BLYP and BLYP-D3(BJ) perform the worst and have the largest MAEs up to 0.063 Å and 7.2 degrees.

The mean absolute error (MAE), mean error (ME), and largest deviation (LD) for the 13 density functionals are computed relative to ZORA-CCSD(T)/BS3+. Three main observations emerge: (i) M06-2X, B3LYP, and M06 perform the best; (ii) BHANDH, BLYP-D3(BJ), and BP86 perform the worst; and (iii) all 13 density functionals overestimate the ΔE compared to ZORA-CCSD(T)/BS3+. The best overall agreement with the *ab initio* benchmark is with the meta-hybrid functionals, M06-2X and M06 (MAE of 4.1–4.3 kcal mol^{-1} and LD of 6.6–6.8 kcal mol^{-1}) and by the popular B3LYP hybrid functional (MAE 4.2 kcal mol^{-1} and LD of 6.4 kcal mol^{-1}) (see Figure 3.6c). GGAs perform the worst and have the largest MAEs up to 9.3 kcal mol^{-1}. BLYP is the best GGA with a MAE of 6.9 kcal mol^{-1} and LD of 8.6 kcal mol^{-1}. Addition of an explicit dispersion correction (D3) and damping function (BJ) for the BLYP and B3LYP functionals results in less accurate ΔE values and increases the MAE to 8.5 and 5.7 kcal mol^{-1}, respectively.

The ME is negative, and its absolute value is equal to the MAE for all density functionals, i.e., the stabilization of the $D_2Ch{\bullet\bullet\bullet}A^-$ chalcogen-bonded complexes is overestimated by all functionals in this study. Nevertheless, our best performing density functionals together with the Slater-type QZ4P basis set have the same trends in chemical stability and geometry as our ZORA-CCSD(T)/BS3+ benchmark, with relatively small deviations from the *ab initio* ΔE_{CPC}. For larger chalcogen-bonded systems, the smaller Slater-type TZ2P basis set may be used, which also provides satisfactory results in comparison with our best *ab initio* level. For our three-best density functionals, B3LYP, M06-2X, and M06, the ΔE is ca. 2 kcal mol^{-1} more over-binding for TZ2P than for QZ4P (see Table 3.6), that is, the overestimation on the stability of chalcogen-bonded systems increases. This results in larger errors relative to our best estimate and the B3LYP, M06-2X, and M06 density functionals in

combination with TZ2P basis set turn out have similar accuracy as the ZORA-BLYP/QZ4P. Thus, we identify not only B3LYP and M06-2X,[7i] but also M06, in combination with the all-electron QZ4P basis set, to be reasonable approaches for computing the complexation energies of chalcogen bonds without relying on expensive *ab initio* methods.

Table 3.6. ZORA-DFT/BS complexation energies (in kcal mol^{-1}) of representative $D_2Ch{\bullet\bullet\bullet}A^-$ chalcogen-bonded complexes.

DFT/BS	$F_2S{\bullet\bullet\bullet}Cl^-$	$Cl_2Se{\bullet\bullet\bullet}F^-$
B3LYP/TZ2P	–26.0	–65.3
M06/TZ2P	–25.6	–66.1
M06-2X/TZ2P	–25.5	–64.0
B3LYP/QZ4P	–23.5	–62.3
M06/QZ4P	–23.1	–63.6
M06-2X/QZ4P	–23.7	–61.9
Benchmark[a]	–20.8	–56.7

[a] ΔE_{CPC} computed at ZORA-CCSD(T)/BS3+.

3.4 Conclusion

We have computed a ZORA-CCSD(T)/BS3+ benchmark for the archetypal chalcogen-bonded model complexes $D_2Ch{\bullet\bullet\bullet}A^-$ (Ch = S, Se; D, A = F, Cl) that derives from a hierarchical series of relativistic *ab initio* methods and basis sets. The counterpoise-corrected ZORA-CCSD(T)/ma-ZORA-def2-QZVPP level is converged within 1.5–3.1 kcal mol^{-1} and 1.1–3.4 kcal mol^{-1} with respect to the basis set size and *ab initio* method, respectively. Our benchmark data show that chalcogen bonds (ChB) in $D_2Ch{\bullet\bullet\bullet}A^-$ become stronger for the heavier chalcogen Ch, the lighter halide A^-, and for the less electronegative halogen substituent D.

Basis sets including diffuse functions are required for the calculation of accurate complexation energies for the chalcogen-bonded complexes $D_2Ch{\bullet\bullet\bullet}A^-$ involving anions. Addition of diffuse functions yields smaller BSSE and faster convergence with respect to the basis set size and *ab initio* method. However, as the BSSE simultaneously decreases as the flexibility of the basis set size increases, the uncorrected and counterpoise-corrected complexation energies become similar for larger basis sets, with or without diffuse functions. Coulomb correlation is also crucial, and, for highly correlated methods, addition of polarization functions is necessary to accurately describe the correlation hole.

The performance of 13 relativistic (ZORA) density functionals for describing the complexation energies of ChB was evaluated. Best agreement with our hierarchical *ab initio* benchmark is achieved by hybrid and meta-hybrid DFT functions, which overestimate the bond strength with mean absolute errors up to 4.3 kcal mol^{-1}. Neither GGA nor meta-GGA DFT approaches can achieve this accuracy. The BLYP functional, which is the best performing GGA approach, overestimates complexation energies by 6.9 kcal mol^{-1}. Taken altogether, M06-2X and M06 and B3LYP in combination with the all-electron QZ4P basis are accurate, efficient, and non-expensive methods for the routine investigation of chalcogen bonds.

3.5 References

[1] (a) R. Gleiter, G. Haberhauer, D. B. Werz, F. Rominger, C. Bleiholder, *Chem. Rev*. **2018**, *118*, 2010. (b) L. -J. Riwar, N. Trapp, K. Root, R. Zenobi, F. Diederich, *Angew. Chem.* **2018**, *130*, 17506; *Angew. Chem. Int. Ed*. **2018**, *57*, 17259. (c) R. Shukla, D. Chopra, *Cryst. Growth Des*. **2016**, *16*, 6734. (d) J. Fanfrlík, A. Přáda, Z. Padělková, A. Pecina, J. Macháček, M. Lepšík, J. Holub, A. Růžička, D. Hnyk, P. Hobza, *Angew. Chem. Int. Ed*. **2014**, *53*, 10139. (e) S. P. Thomas, V. Kumar, K. Alhameedi, T. N. Guru Row, *Chem. Eur. J*. **2019**, *25*, 3591. (f) P. Scilabra, J. S. Murray, G. Terraneo, G. Resnati, *Cryst. Growth Des*. **2019**, *19*, 1149. (g) F. -U. Rahman, D. Tzeli, I. D. Petsalakis, G. Theodorakopoulos, P. Ballester, J. Rebek Jr., Y. Yu, *J. Am. Chem. Soc.* **2020**, *142*, 5876. (h) R. Zeng, Z. Gong, Q. Yan, *J. Org. Chem.* **2020**, *85*, 8397. (i) P. C. Ho, J. Z. Wang, F. Meloni, I. Vargas-Baca, *Coord. Chem. Rev.* **2020**, *422*, 213464. (j) S. Mehrparvar, C. Wölper, R. Gleiter, G. Haberhauer, *Angew. Chem.* **2020**, *132*, 17303; *Angew. Chem. Int. Ed*. **2020**, *59*, 17154.

[2] (a) S. Benz, M. Macchione, Q. Verolet, J. Mareda, N. Sakai, S. Matile, *J. Am. Chem. Soc*. **2016**, *138*, 9093. (b) M. Macchione, M. Tsemperouli, A. Goujon, A. R. Mallia, N. Sakai, K. Sugihara, S. Matile, *Helv. Chim. Acta* **2018**, *101*, e1800014. (c) M. Iwaoka in *Noncovalent Forces. Challenges and Advances in Computational Chemistry and Physics*, (Eds: S. Scheiner), Springer, Cham, **2015**, p 265. (d) L. M. Lee, M. Tsemperouli, A. I. Poblador-Bahamonde, S. Benz, N. Sakai, K. Sugihara, S. Matile, *J. Am. Chem. Soc*. **2019**, *141*, 810. (e) P. B. Lutz, C. A. Bayse, *J. Inorg. Biochem*. **2016**, *157*, 94. (f) M. Iwaoka, N. Babe, *Phosphorus*, *Sulfur, and Silicon* **2015**, *190*, 1257. (g) S. P. Thomas, D. Jayatilaka, T. N. Guru Row, *Phys. Chem. Chem. Phys*. **2015**, *17*, 25411. (h) A. Lange, M. Günther, F. M. Büttner, M. O. Zimmermann, J. Heidrich, S. Hennig, S. Zahn, C. Schall, A. Sievers-Engler, F. Ansideri, P. Koch, M. Lämmerhofer, T. Stehle, S. A. Laufer, F. M. Boeckler, *J. Am. Chem. Soc*. **2015**, *137*, 14640. (i) B. Galmés, A. Juan-Bals, A. Frontera, G. Resnati, *Chem. Eur. J.* **2020**, *26*, 4599.

[3] (a) J. Bamberger, F. Ostler, O. G. Mancheño, *ChemCatChem* **2019**, *11*, 5198. (b) K. T. Mahmudov, M. N. Kopylovich, M. F. C. Guedes Da Silva, A. J. L. Pombeiro, *Dalt. Trans*. **2017**, *46*, 10121. (c) S. Benz, J. López-Andarias, J. Mareda, N. Sakai, S. Matile, *Angew. Chem.* **2017**, *129*, 830; *Angew. Chem. Int. Ed*. **2017**, *56*, 812. (d) W. Wang, H. Zhu, L. Feng, Q. Yu, J. Hao, R. Zhu, Y. Wang, *J. Am. Chem. Soc.* **2020**, *142*, 3117. (e) Y. Li, L. Meng, C. Sun, Y. Zeng, *J. Phys. Chem. A* **2020**, *124*, 3815.

[4] (a) L. Vogel, P. Wonner, S. M. Huber, *Angew. Chem.* **2019**, *131*, 1896; *Angew. Chem. Int. Ed.* **2019**, *58*, 1880. (b) W. Wang, B. Ji, Y. Zhang, *J. Phys. Chem. A* **2009**, *113*, 8132. (c) M. E. Brezgunova, J. Lieffrig, E. Aubert, S. Dahaoui, P. Fertey, S. Lebègue, J. G. Ángyán, M. Fourmigué, E. Espinosa, *Cryst. Growth Des.* **2013**, *13*, 3283. (d) P. Politzer, J. S. Murray, M. C. Concha, *J. Mol. Model.* **2008**, *14*, 659. (e) T. Clark, M. Hennemann, J. S. Murray, P. Politzer, *J. Mol. Model.* **2007**, *13*, 291. (f) J. Lu, S. Scheiner, *J. Phys. Chem. A* **2020**, *124*, 7716. (g) S. Scheiner, M. Michalczyk, W. Zierkiewicz, *Coord. Chem. Rev.* **2020**, *405*, 213136. (h) T. Fellowes, B. L. Harris, J. M. White, *Chem. Commun.* **2020**, *56*, 3313. (i) G. Haberhauer, R. Gleiter, *Angew. Chem.* **2020**, *132*, 2; *Angew. Chem. Int. Ed*. **2020**, *59*, 2. (j) A. Bauzá, A. Frontera, *ChemPhysChem*, **2020**, *21*, 26.

[5] (a) L. P. Wolters, F. M. Bickelhaupt, *ChemistryOpen.* **2012**, *1*, 96. (b) M. Bortoli, S. M. Ahmad, T. A. Hamlin, F. M. Bickelhaupt, L. Orian, *Phys. Chem. Chem. Phys.* **2018**, *20*, 27592. (c) D. J. Pascoe, K. B. Ling, S. L. Cockroft, *J. Am. Chem. Soc.* **2017**, *139*, 15160. (d) S. M. Huber, J. D. Scanlon, E. Jimenez-Izal, J. M. Ugalde, I. Infante, *Phys. Chem. Chem. Phys.* **2013**, *15*, 10350.

[6] (a) L. P. Wolters, F. M. Bickelhaupt, *WIREs Comput. Mol. Sci.* **2015**, *5*, 324. (b) F. M. Bickelhaupt, *J. Comput. Chem.* **1999**, *20*, 114. (c) O. A. Stasyuk, R. Sedlak, C. Fonseca Guerra, P. Hobza, *J. Chem. Theory Comput.* **2018**, *14*, 3440. (d) T. A. Hamlin, I. Fernandez, F. M. Bickelhaupt, *Angew. Chem.* **2019**, *131*, 9015; *Angew. Chem. Int. Ed.* **2019**, *58*, 8922. (e) P. Vermeeren, S. C. C. van der Lubbe; C. Fonseca Guerra, F. M. Bickelhaupt, T. A. Hamlin, *Nat. Protoc.* **2020**, *15*, 649.

[7] (a) A. Forni, S. Pieraccini, S. Rendine, M. Sironi, *J. Comput. Chem.* **2014**, *35*, 386. (b) J. Řezáč, P. Hobza, *Chem. Rev.* **2016**, *116*, 5038. (c) G. T. de Jong, M. Solà, L. Visscher, F. M. Bickelhaupt, *J. Chem. Phys.* **2004**, *121*, 9982. (d) G. T. de Jong, D. P. Geerke, A. Diefenbach, F. M. Bickelhaupt, *Chem. Phys.* **2005**, *313*, 261. (e) Y. Kim, S. Song, E. Sim, K. Burke, *J. Phys. Chem. Lett.* **2019**, *10*, 295. (f) J. Witte, J. B. Neaton, M. Head-Gordon, *J. Chem. Phys.* **2016**, *144*, 194306. (g) D. G. Truhlar, *Chem. Phys. Lett.* **1998**, *294*, 45. (h) H. Eshuis, F. Furche, *J. Chem. Phys.* **2012**, *136*, 084105. (i) A. Bauzá, I. Alkorta, A. Frontera, J. Elguero, *J. Chem. Theory Comput.* **2013**, *9*, 5201. (j) A. Otero-de-la-Roza, E. R. Johnson, G. A. DiLabio, *J. Chem. Theory Comput.* **2014**, *10*, 5436.

[8] S. F. Boys, F. Bernardi, *Mol. Phys.* **1970**, *19*, 553.

[9] F. Neese, *WIREs Comput. Mol. Sci.* **2012**, *2*, 73.

[10] (a) F. Weigend, R. Ahlrichs, *Phys. Chem. Chem. Phys.* **2005**, *7*, 3297. (b) D. A. Pantazis, X. Chen, C. R. Landis, F. Neese, *J. Chem. Theory* **2008**, *4*, 908. (c) J. Zheng, X. Xu, D. G. Truhlar, *Theor. Chem. Acc.* **2011**, *128*, 295.

[11] K. Raghavachari, G. W. Trucks, J. A. Pople, M. Head-Gordon, *Chem. Phys. Lett.* **1989**, *157*, 479.

[12] C. Møller, M. S. Plesset, *Phys. Rev.* **1934**, *46*, 618.

[13] G. D. Purvis, R. J. Bartlett, *J. Chem. Phys.* **1982**, *76*, 1910.

[14] E. van Lenthe, E. J. Baerends, J. G. Snijders, *J. Chem. Phys.* **1994**, *101*, 9783.

[15] (a) G. te Velde, F. M. Bickelhaupt, E. J. Baerends, C. Fonseca Guerra, S. J. A. van Gisbergen, J. G. Snijders, T. Ziegler, *J. Comput. Chem.* **2001**, *22*, 931. (b) C. Fonseca Guerra, J. G. Snijders, G. te Velde, E. J. Baerends, *Theor. Chem. Acc.* **1998**, *99*, 391. (c) ADF2017, SCM Theoretical Chemistry, Vrije Universiteit, Amsterdam, The Netherlands 2017.

[16] P. J. Perdew, K. Burke, M. Ernzerhof, *Phys. Rev. Lett.* **1996**, *77*, 3865.

[17] (a) A. D. Becke, *Phys. Rev. A* **1988**, *38*, 3098. (b) J. P. Perdew, *Phys. Rev. B* **1986**, *33*, 8822.

[18] (a) C. Lee, W. Yang, R. G. Parr, *Phys. Rev. B* **1988**, *37*, 785. (b) B. G. Johnson, P. M. W. Gill, J. A. Pople, *J. Chem. Phys.* **1993**, *98*, 5612. (c) T. V. Russo, R. L. Martin, P. J. Hay, *J. Chem. Phys.* **1994**, *101*, 7729.

[19] P. J. Stephens, F. J. Devlin, C. F. Chabalowski, M. J. Frisch, *J. Phys. Chem.* **1994**, *98*, 11623.

[20] (a) M. Swart, M. Solà, F. M. Bickelhaupt, *J. Chem. Phys.* **2009**, *131*, 094103. (b) M. Swart, M. Solà, F. M. Bickelhaupt, *J. Comput. Methods Sci. Eng.* **2009**, *9*, 69.

[21] (a) Y. Zhao, D. G. Truhlar, *Theor. Chem. Acc.* **2008**, *120*, 215. (b) Y. Zhao, D. G. Truhlar, *J. Chem. Phys.* **2006**, *125*, 194101.

[22] S. Grimme, S. Ehrlich, L. Goerigk, *J. Comput. Chem.* **2011**, *32*, 1456.

[23] E. van Lenthe, E. J. Baerends, *J. Comput. Chem.* **2003**, *24*, 1142.

[24] (a) M. Swart, M. Solà, F. M. Bickelhaupt, *J. Chem. Theory Comput.* **2010**, *6*, 3145. (b) B. J. Lynch, Y. Zhao, D. G. Truhlar, *J. Phys. Chem. A* **2013**, *107*, 1384. (c) T. Clark, J. Chandrasekhar, G. W. Spitznagel, P. v. R. Schleyer, *J. Comput. Chem.* **1983**, *4*, 294. (d) F. Jensen, *J. Chem. Phys.* **2002**, *117*, 9234. (e) A. Bauzá, D. Quiñonero, P. M. Deyà, A. Frontera, *J. Phys. Chem. A* **2013**, *117*, 2651.

[25] W. -J. van Zeist, R. Yi, F. M. Bickelhaupt. *Sci. China Chem.* **2010**, *53*, 210.

3.6 Appendices

Appendix 3.1. *Ab initio* bond lengths and angles (in Å and degrees) of $D_2S\cdots A^-$ chalcogen-bonded complexes.[a]

	$F_2S\cdots F^-$					$F_2S\cdots Cl^-$				
Basis set	r_{Ch-A^-}	$r_{Ch-D}{}^1$	$r_{Ch-D}{}^2$	Θ_1	Θ_2	r_{Ch-A^-}	$r_{Ch-D}{}^1$	$r_{Ch-D}{}^2$	Θ_1	Θ_2
BS1	1.792	1.792	1.660	86.3	86.3	2.533	1.719	1.637	90.1	87.7
BS2	1.809	1.809	1.644	86.9	86.9	2.452	1.739	1.629	89.4	88.4
BS3	1.805	1.805	1.637	86.8	86.8	2.446	1.732	1.623	89.4	88.1
BS1+	1.856	1.856	1.679	87.4	87.4	2.511	1.783	1.666	89.7	88.7
BS2+	1.809	1.809	1.640	86.9	86.9	2.450	1.736	1.626	89.4	88.1
BS3+	1.806	1.806	1.637	86.8	86.8	2.441	1.733	1.623	89.4	88.0
	$Cl_2S\cdots F^-$					$Cl_2S\cdots Cl^-$				
	r_{Ch-A^-}	$r_{Ch-D}{}^1$	$r_{Ch-D}{}^2$	Θ_1	Θ_2	r_{Ch-A^-}	$r_{Ch-D}{}^1$	$r_{Ch-D}{}^2$	Θ_1	Θ_2
BS1	1.734	2.526	2.108	90.7	92.2	2.393	2.393	2.100	93.5	93.5
BS2	1.759	2.457	2.068	91.7	92.1	2.349	2.349	2.064	94.0	94.0
BS3	1.752	2.451	2.053	91.2	92.1	2.337	2.337	2.050	93.5	93.5
BS1+	1.804	2.526	2.106	92.8	92.8	2.416	2.416	2.107	95.2	95.2
BS2+	1.755	2.460	2.062	91.6	92.2	2.346	2.346	2.060	93.9	93.9
BS3+	1.752	2.450	2.052	91.2	92.1	2.336	2.336	2.050	93.5	93.5

[a] Computed at ZORA-CCSD(T)/Basis set.

Appendix 3.2. *Ab initio* bond lengths and angles (in Å and degrees) of $D_2Se\cdots A^-$ chalcogen-bonded complexes.[a]

	$F_2Se\cdots F^-$					$F_2Se\cdots Cl^-$				
Basis set	r_{Ch-A^-}	$r_{Ch-D}{}^1$	$r_{Ch-D}{}^2$	Θ_1	Θ_2	r_{Ch-A^-}	$r_{Ch-D}{}^1$	$r_{Ch-D}{}^2$	Θ_1	Θ_2
BS1	1.902	1.902	1.784	86.4	86.4	2.521	1.859	1.773	88.5	88.5
BS2	1.919	1.919	1.775	86.5	86.5	2.489	1.877	1.767	88.0	88.8
BS3	1.915	1.915	1.770	86.5	86.5	2.479	1.873	1.763	87.9	88.5
BS1+	1.956	1.956	1.810	87.5	87.5	2.507	1.922	1.805	88.5	89.2
BS2+	1.917	1.917	1.770	86.4	86.4	2.480	1.876	1.763	87.7	88.4
BS3+	1.915	1.915	1.769	86.5	86.5	2.476	1.874	1.763	87.8	88.3
	$Cl_2Se\cdots F^-$					$Cl_2Se\cdots Cl^-$				
	r_{Ch-A^-}	$r_{Ch-D}{}^1$	$r_{Ch-D}{}^2$	Θ_1	Θ_2	r_{Ch-A^-}	$r_{Ch-D}{}^1$	$r_{Ch-D}{}^2$	Θ_1	Θ_2
BS1	1.871	2.525	2.246	91.8	91.5	2.461	2.461	2.238	93.8	93.8
BS2	1.893	2.501	2.205	92.4	91.2	2.439	2.439	2.203	94.1	94.1
BS3	1.889	2.492	2.193	91.8	91.0	2.430	2.430	2.190	93.3	93.3
BS1+	1.939	2.524	2.243	93.1	91.5	2.476	2.476	2.243	94.6	94.6
BS2+	1.891	2.496	2.200	92.0	90.9	2.435	2.435	2.197	93.5	93.5
BS3+	1.891	2.490	2.192	91.7	90.9	2.429	2.429	2.190	93.3	93.3

[a] Computed at ZORA-CCSD(T)/Basis set.

Appendix 3.3. Complexation energies (in kcal mol^{-1}) of $D_2Ch\cdots A^-$ chalcogen-bonded complexes.[a]

A^-	B3LYP	B3LYP[b]	BHANDH	BLYP	BLYP[b]	BP86	M06	M06-HF	M06-L	M06-2X	PBE	SSB-D	SSB[b]
						$F_2S\cdots A^-$							
F^-	–51.2	–51.9	–57.4	–53.8	–54.6	–55.1	–50.1	–53.8	–52.6	–51.5	–57.0	–56.4	–56.5
Cl^-	–23.5	–25.3	–26.0	–26.7	–28.9	–27.9	–23.1	–26.8	–23.6	–23.7	–29.6	–27.6	–28.2
						$Cl_2S\cdots A^-$							
F^-	–54.1	–54.9	–60.3	–56.3	–57.2	–57.4	–53.1	–56.6	–55.4	–54.3	–58.5	–55.4	–55.5
Cl^-	–25.8	–28.2	–27.5	–29.6	–32.3	–30.4	–25.3	–28.3	–24.9	–25.0	–31.4	–26.8	–27.5
						$F_2Se\cdots A^-$							
F^-	–61.7	–62.4	–68.2	–63.4	–64.3	–64.6	–62.4	–62.3	–63.9	–61.7	–66.5	–66.3	–66.4
Cl^-	–33.8	–35.7	–37.6	–36.1	–38.3	–37.5	–34.6	–36.4	–34.5	–33.8	–39.1	–37.3	–37.7
						$Cl_2Se\cdots A^-$							
F^-	–62.3	–63.1	–67.9	–64.4	–65.2	–65.3	–63.6	–60.0	–66.6	–61.9	–66.5	–64.8	–64.9
Cl^-	–34.8	–37.1	–37.3	–38.4	–40.4	–38.7	–35.7	–35.3	–36.3	–34.0	–39.7	–36.1	–36.7

[a] Computed at ZORA-DFT/QZ4P. [b] Includes the D3(BJ) dispersion correction.

Appendix 3.4. The mean error (ME), mean absolute error (MAE), and largest deviation (LD) of ZORA-DFT/QZ4P approaches relative to the geometries (in Å and degrees) and counterpoise corrected complexation energies (in kcal mol^{-1}) of $D_2Ch\cdots A^-$ complexes computed at ZORA-CCSD(T)/BS3+.

	r_{Ch-A^-}			Θ_2			ΔE		
DFT	**ME**	**MAE**	**LD**	**ME**	**MAE**	**LD**	**ME**	**MAE**	**LD**
B3LYP	0.034	0.034	0.048	2.1	2.1	4.7	–4.2	4.2	6.4
B3LYP-D3(BJ)	0.032	0.032	0.048	1.8	1.8	3.4	–5.7	5.7	7.2
BHANDH	–0.042	0.042	0.052	–1.2	1.2	1.5	–8.6	8.6	12.6
BLYP	0.060	0.060	0.094	7.2	7.2	26.7	–6.9	6.9	8.6
BLYP-D3(BJ)	0.063	0.063	0.095	4.9	4.9	12.2	–8.5	8.5	9.5
BP86	0.034	0.040	0.071	3.3	3.3	7.8	–7.9	7.9	9.9
M06	0.009	0.010	0.019	1.0	1.0	2	–4.3	4.3	6.8
M06-HF	–0.016	0.017	0.023	–1.5	1.5	2.5	–5.8	5.8	8.9
M06-L	0.031	0.031	0.049	1.2	1.3	3.2	–5.5	5.5	9.9
M06-2X	–0.004	0.006	0.016	–0.7	0.7	1.1	–4.1	4.1	6.6
PBE	0.028	0.038	0.071	2.7	2.7	6.2	–9.3	9.3	11.7
SSB-D	0.012	0.039	0.077	3.4	3.4	5.3	–7.2	7.2	11.2
SSB-D3(BJ)	0.010	0.040	0.086	3.2	3.2	5.2	–7.5	7.5	11.3

Appendix 3.5. Representative DFT bond lengths and angles (in Å and degrees) of $D_2S\cdots A^-$ chalcogen-bonded complexes.[a]

	$F_2S\cdots F^-$					$F_2S\cdots Cl^-$				
DFT	r_{Ch-A}^-	r_{Ch-D}^1	r_{Ch-D}^2	Θ_1	Θ_2	r_{Ch-A}^-	r_{Ch-D}^1	r_{Ch-D}^2	Θ_1	Θ_2
B3LYP	1.833	1.833	1.655	87.5	87.5	2.466	1.769	1.640	89.4	89.1
BLYP-D3(BJ)	1.873	1.873	1.693	88.7	88.7	2.458	1.827	1.678	90.3	90.7
M06	1.813	1.813	1.631	87.0	87.0	2.452	1.735	1.617	89.3	88.2
M06-2X	1.795	1.795	1.631	86.2	86.2	2.442	1.722	1.617	88.7	87.2
PBE	1.843	1.843	1.675	87.9	87.9	2.401	1.803	1.663	89.1	89.4
Benchmark[b]	1.806	1.806	1.637	86.8	86.8	2.441	1.733	1.623	89.4	88.0
	$Cl_2S\cdots F^-$					$Cl_2S\cdots Cl^-$				
	r_{Ch-A}^-	r_{Ch-D}^1	r_{Ch-D}^2	Θ_1	Θ_2	r_{Ch-A}^-	r_{Ch-D}^1	r_{Ch-D}^2	Θ_1	Θ_2
B3LYP	1.786	2.476	2.082	93.9	93.3	2.384	2.384	2.074	96.3	96.3
BLYP-D3(BJ)	1.847	2.468	2.125	95.9	95.3	2.411	2.411	2.117	98.5	98.5
M06	1.748	2.477	2.051	92.1	93.0	2.339	2.339	2.048	94.4	94.4
M06-2X	1.736	2.461	2.046	90.9	91.7	2.339	2.339	2.042	93.2	93.2
PBE	1.823	2.415	2.083	94.2	93.5	2.364	2.364	2.077	96.7	96.7
Benchmark[b]	1.752	2.450	2.052	91.2	92.1	2.336	2.336	2.050	93.5	93.5

[a] Computed at ZORA-DFT/QZ4P level. [b] Computed at ZORA-CCSD(T)/BS3+.

Appendix 3.6. Representative DFT bond lengths and angles (in Å and degrees) of $D_2Se\cdots A^-$ chalcogen-bonded complexes.[a]

	$F_2Se\cdots F^-$					$F_2Se\cdots Cl^-$				
DFT	r_{Ch-A}^-	r_{Ch-D}^1	r_{Ch-D}^2	Θ_1	Θ_2	r_{Ch-A}^-	r_{Ch-D}^1	r_{Ch-D}^2	Θ_1	Θ_2
B3LYP	1.946	1.946	1.794	87.7	87.7	2.511	1.912	1.788	88.9	90.4
BLYP-D3(BJ)	1.983	1.983	1.835	89.5	89.5	2.526	1.956	1.829	90.8	92.4
M06	1.931	1.931	1.773	87.3	87.3	2.495	1.888	1.765	88.6	89.6
M06-2X	1.910	1.910	1.765	85.4	85.4	2.481	1.868	1.757	86.8	87.4
PBE	1.958	1.958	1.815	88.3	88.3	2.473	1.936	1.808	89.3	90.7
Benchmark[b]	1.915	1.915	1.769	86.5	86.5	2.476	1.874	1.763	87.8	88.3
	$Cl_2Se\cdots F^-$					$Cl_2Se\cdots Cl^-$				
	r_{Ch-A}^-	r_{Ch-D}^1	r_{Ch-D}^2	Θ_1	Θ_2	r_{Ch-A}^-	r_{Ch-D}^1	r_{Ch-D}^2	Θ_1	Θ_2
B3LYP	1.927	2.520	2.231	96.1	93.7	2.468	2.468	2.232	98.0	98.0
BLYP-D3(BJ)	1.971	2.528	2.286	99.4	98.0	2.483	2.483	2.307	105.5	105.5
M06	1.903	2.504	2.200	93.8	92.5	2.438	2.438	2.198	95.3	95.3
M06-2X	1.885	2.494	2.186	91.2	89.9	2.428	2.428	2.190	92.5	92.5
PBE	1.952	2.484	2.237	96.5	94.9	2.452	2.452	2.241	99.5	99.5
Benchmark[b]	1.891	2.490	2.192	91.7	90.9	2.429	2.429	2.190	93.3	93.3

[a] Computed at ZORA-DFT/QZ4P level. [b] Computed at ZORA-CCSD(T)/BS3+.

4 | The Chalcogen Bond

Part of this chapter previously appeared as

A Quantitative MO Perspective of the Chalcogen Bond
L. de Azevedo Santos, S. C. C. van der Lubbe, T. A. Hamlin, T. C. Ramalho,
F. Matthias Bickelhaupt
ChemistryOpen. **2021**, *10*, 391–401

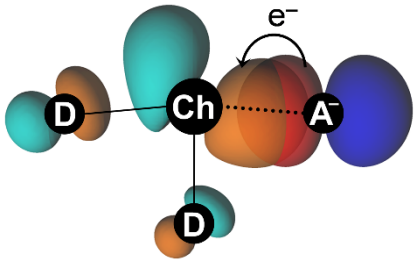

LUMO–HOMO

Abstract | We have quantum chemically analyzed the structure and stability of archetypal chalcogen-bonded model complexes $D_2Ch{\bullet\bullet\bullet}A^-$ (Ch = O, S, Se, Te; D, A = F, Cl, Br) using relativistic density functional theory at ZORA-M06/QZ4P. Our purpose is twofold: (i) to compute accurate trends in chalcogen-bond strength based on a set of consistent data; and (ii) to rationalize these trends in terms of detailed analyses of the bonding mechanism based on quantitative Kohn-Sham molecular orbital (KS-MO) theory in combination with a canonical energy decomposition analysis (EDA). At odds with the commonly accepted view of chalcogen bonding as a predominantly electrostatic phenomenon, we find that chalcogen bonds, just as hydrogen and halogen bonds, have a significant covalent character stemming from strong HOMO–LUMO interactions. Besides providing significantly to the bond strength, these orbital interactions are also manifested by the structural distortions they induce as well as the associated charge transfer from A^- to D_2Ch.

Keywords | Activation strain model, Chalcogen bonding, Density functional calculations, Energy decomposition analysis, Noncovalent Interactions

4.1 Introduction

The chalcogen-bond (ChB) is the net-attractive intermolecular interaction, often referred to as noncovalent interaction, between a Lewis-basic chalcogen-bond acceptor A and a Lewis-acidic chalcogen-bond donor D_2Ch featuring a chalcogen (group 16) atom Ch to which A binds.[1] Nearly 40 years ago, the first systematic study appeared of the chalcogen bond in which S•••Y (*e.g.*, Y = S, O, F, Cl, or Br) nonbonded atomic contacts were investigated.[2] Early studies generally characterized chalcogen bonds as being predominantly electrostatic in nature.[3] Later on, the significance of charge transfer from the occupied orbital of a Lewis base into an empty σ*-type orbital of a chalcogen molecule controlling the chalcogen bond strength was recognized.[4] Chalcogen-bonding has since found applications in various fields of chemistry,[1] including, supramolecular,[5] biochemistry,[6] spectroscopy[7] and catalysis.[8]

In this study, we have computationally analyzed a range of chalcogen-bonded $D_2Ch•••A^-$ complexes (Ch = O, S, Se, Te; D, A = F, Cl, Br; see Scheme 4.1), using relativistic density functional theory (DFT) at ZORA-M06/QZ4P. One purpose of our work is to provide a set of consistent structural and energy data from which reliable trends can be inferred for a wide range of model systems. The primary objective is to achieve a detailed understanding of the nature of chalcogen bonds by studying the associated electronic structure and bonding mechanism and compare them with the better-known halogen bonds and hydrogen bonds.[9]

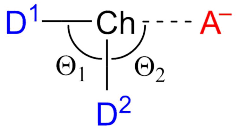

Scheme 4.1. Chalcogen–bonded $D_2Ch\cdots A^-$ model complexes (Ch = O, S, Se, Te; D, A = F, Cl, Br).

To this end, we first explore how the geometries and energies of our model complexes $D_2Ch\cdots A^-$ vary as the chalcogen atom (Ch), or the chalcogen bond accepting Lewis base (A^-) are varied. To understand the origin of the computed trends, activation strain analyses[10] are performed on the formation of the chalcogen-bond complexes. As part of these analyses, the interaction energy and the underlying bonding mechanism are furthermore examined in the context of quantitative Kohn-Sham molecular orbital (MO) theory in combination with an energy decomposition analysis (EDA).[11,12] Our systematic and detailed analyses along the entire reaction profile for each of the chalcogen-bond complexation reactions provide in-depth

insights. In particular, they demonstrate that chalcogen bonds are not at all purely electrostatic phenomena but are, to a substantial extent, covalent in nature.

4.2 Theoretical Methods

Computational details

All calculations were carried out using the Amsterdam Density Functional (ADF) 2017.103 program.[13] The equilibrium geometries and energies of chalcogen-bonded complexes were computed at DFT level using the meta-hybrid functional M06.[14] In addition, a large uncontracted relativistically optimized QZ4P Slater type orbitals (STOs) basis set containing diffuse functions was used. The QZ4P all-electron basis set,[15] no frozen-core approximation, is of quadruple-ζ quality for all atoms and has been augmented with the following sets of polarization and diffuse functions: two 3*d* and two 4*f* on oxygen and fluorine, three 3*d* and two 4*f* on sulfur and chlorine, two 4*d* and three 4*f* on selenium and bromine, one 5*d* and three 4*f* on tellurium and iodine. The molecular density was fitted by the systematically improvable Zlm fitting scheme. The scalar relativistic effects were accounted for by using the zeroth-order regular approximation (ZORA) Hamiltonian.[16] It has been shown that these computational settings give accurate bond lengths and energies.[17]

Analysis of the bonding mechanism

Insight into the bonding mechanism is obtained through activation strain analyses of the various chalcogen bond formation reactions. These complexation reactions are computationally modeled by increasing the distance between A^- and the Ch atom of the D_2Ch fragment, allowing the system to geometrically relax at each point. The $D_2Ch{\bullet\bullet\bullet}A^-$ distance is increased from the actual bond length value in the chalcogen-bonded complex ($r_{Ch\cdots A^-}$) to a value of 4.300 Å. Thus, each analysis starts from an optimized $D_2Ch{\bullet\bullet\bullet}A^-$ complex, which is then transformed to the D_2Ch molecule and a halide at a relatively large distance.

These complexation reactions are analyzed using the activation strain model. The activation strain model of chemical reactivity[10] is a fragment-based approach to understand the energy profile of a chemical process in terms of the original reactants. Thus, the potential energy surface $\Delta E(\zeta)$ is decomposed along the reaction coordinate ζ (or just at one point along ζ) into the strain energy $\Delta E_{strain}(\zeta)$, which is associated with the geometrical deformation of the

individual reactants as the process takes place, plus the actual interaction energy $\Delta E_{int}(\zeta)$ between the deformed reactants [Eq. (4.1)].

$$\Delta E(\zeta) = \Delta E_{strain}(\zeta) + \Delta E_{int}(\zeta) \tag{4.1}$$

In the equilibrium geometry, that is, for $\zeta = \zeta_{eq}$, this yields an expression for the bond energy $\Delta E(\zeta_{eq}) = \Delta E_{strain}(\zeta_{eq}) + \Delta E_{int}(\zeta_{eq})$. The PyFrag program was used to facilitate the analyses along the reaction coordinate ζ of the bond formation processes.[18] The interaction energy $\Delta E_{int}(\zeta)$ between the deformed reactants is further analyzed in the conceptual framework provided by the quantitative Kohn–Sham MO model.[11] To this end, it is decomposed in three physically meaningful terms [Eq. (4.2)] using a quantitative energy decomposition scheme developed by Ziegler and Rauk.[12]

$$\Delta E_{int}(\zeta) = \Delta V_{elstat}(\zeta) + \Delta E_{Pauli}(\zeta) + \Delta E_{oi}(\zeta) \tag{4.2}$$

$$\Delta V_{elstat}(\zeta) = \Delta V_{elstat,\rho_1\rho_2}(\zeta) + \Delta V_{elstat,n_1\rho_2}(\zeta) + \Delta V_{elstat,\rho_1 n_2}(\zeta) + \Delta V_{elstat,n_1 n_2}(\zeta) \tag{4.3}$$

The usually attractive term ΔV_{elstat} corresponds to the classical Coulomb interaction between the unperturbed charge distributions of the deformed reactants and has four components [Eq. (4.3)]: i) the electrostatic repulsion between the electron densities of fragments 1 and 2, $\Delta V_{elstat,\rho_1\rho_2}$; ii) the electrostatic attraction between the nucleus of fragment 1 and the electron density of fragment 2, $\Delta V_{elstat,n_1\rho_2}$; iii) the electrostatic attraction between the electron density of fragment 1 and the nucleus of fragment 2, $\Delta V_{elstat,\rho_1 n_2}$; and iv) the electrostatic repulsion between the nuclei of fragments 1 and 2, $\Delta V_{elstat,n_1 n_2}$. The Pauli repulsion energy (ΔE_{Pauli}) comprises the destabilizing interactions between occupied orbitals of the reactants and is responsible for steric repulsion. The orbital-interaction energy (ΔE_{oi}) accounts for charge transfer, that is, the interaction between occupied orbitals of one fragment with unoccupied orbitals of the other fragment, including the interactions of the highest occupied and lowest unoccupied MOs (HOMO–LUMO), and polarization, that is, empty–occupied orbital mixing on one fragment, due to the presence of another fragment.

The electron density distribution is analyzed using the Voronoi deformation density (VDD) method for computing atomic charges.[19] The VDD atomic charge on atom X in a molecule (Q_X^{VDD}) is computed as the (numerical) integral of the deformation density in the volume of the Voronoi cell of atom X [Eq. (4.4)]. The Voronoi cell of atom X is defined as the compartment of space bounded by the bond midplanes on and perpendicular to all bond axes between nucleus X and its neighboring nuclei.

$$Q_{\mathrm{X}}^{\mathrm{VDD}} = -\int_{\text{Voronoi cell of X}} \left[\rho(\mathrm{r}) - \rho_{\text{promolecule}}(\mathrm{r})\right] d\mathrm{r} \tag{4.4}$$

Here, the deformation density is the difference between ρ(r), *i.e.*, the electron density of the overall molecule or complex, and $\rho_{\text{promolecule}}(\mathrm{r}) = \Sigma_{\mathrm{Y}}\rho_{\mathrm{Y}}(\mathrm{r})$, *i.e.*, the superposition of spherical average-of-configuration atomic densities $\rho_{\mathrm{Y}}(\mathrm{r})$ of each atom Y in the fictitious promolecule without chemical interactions, in which all atoms are considered neutral. The interpretation of the VDD charge $Q_{\mathrm{Ch}}{}^{\mathrm{VDD}}$ is rather straighforward and transparent: instead of measuring the amount of charge associated with a particular atom Ch, $Q_{\mathrm{Ch}}{}^{\mathrm{VDD}}$ directly monitors how much charge flows out of ($Q_{\mathrm{Ch}}{}^{\mathrm{VDD}} > 0$) or into ($Q_{\mathrm{Ch}}{}^{\mathrm{VDD}} < 0$) the Voronoi cell of atom Ch due to chemical interactions.

The VDD scheme can also be used to directly compute how much charge flows into or out of an atomic Voronoi cell X in an overall complex (*e.g.*, $[D_2Ch{\bullet\bullet\bullet}A]^{-}$) relative to two (poly)atomic molecular fragments (*e.g.*, D_2Ch and A^{-}), instead of spherical atoms, as shown in [Eq. (4.5)].

$$\Delta Q_{\mathrm{X}}^{\mathrm{VDD}} = -\int_{\text{Voronoi cell of X in complex}} \left[\rho_{\text{complex}}(\mathrm{r}) - \rho_{\text{fragment 1}}(\mathrm{r}) - \rho_{\text{fragment 2}}(\mathrm{r})\right] d\mathrm{r} \tag{4.5}$$

$\Delta Q_{\mathrm{X}}{}^{\mathrm{VDD}}$ is a measure of how the atomic charge of atom X changes due to the bonding between the fragment. In this work, [Eq. (4.5)] is used to compute the flow of electrons from the halide A^{-} to the chalcogen-bond donating molecule D_2Ch (see $\Delta Q_{\mathrm{D_2Ch}}{}^{\mathrm{VDD}}$ in Table 4.1).

4.3 Results and Discussion

Chalcogen bond strength and structure

The results of our ZORA-M06/QZ4P calculations are shown in Table 4.1 for a representative selection of oxygen-, sulfur-, and tellurium-bonded model complexes $D_2Ch{\bullet\bullet\bullet}A^{-}$, covering D, A = F, Cl, and Br (the complete dataset for all model systems is provided in Appendices 4.1 and 4.2). In the first place, we note that all model reactions are associated with single-well potential energy surfaces (PES), that is, there is no energy barrier separating the reactants from their resulting complex. In the cases where D ≠ A, C_s symmetric complexes with D^1–Ch bond lengths longer than D^2–Ch and with bond angles $\Theta_1 \neq \Theta_2$ are formed. For the cases where D =

A, C_{2v} symmetric complexes with equal bond distances $r_{Ch–D^1} = r_{Ch\cdots A}$ and equal bond angles $\Theta_1 = \Theta_2$ are formed (see Table 4.1).

Table 4.1. Activation strain analyses (in kcal mol^{-1}) of a representative set of $D_2Ch\bullet\bullet\bullet A^-$ at the equilibrium geometries (in Å, deg.)[a]

$D_2Ch\bullet\bullet\bullet A^-$	ΔE	ΔE_{strain}	ΔE_{int}	$\Delta Q_{D_2Ch}^{VDD}$	$r_{Ch\cdots A}$	$\Delta r_{D^1–Ch}$	$\Delta r_{D^2–Ch}$	Θ_1	Θ_2	$\Delta\Theta_1$
$F_2O\bullet\bullet\bullet F^-$	–21.9	28.3	–50.2	–0.37	1.784	0.408	–0.002	97.6	97.6	–6.1
$F_2O\bullet\bullet\bullet Cl^-$	–9.9	28.1	–37.9	–0.35	2.183	0.402	0.007	98.8	101.3	–4.9
$F_2O\bullet\bullet\bullet Br^-$	–11.5	45.0	–56.5	–0.48	2.113	0.582	0.023	98.6	103.4	–5.1
$Cl_2O\bullet\bullet\bullet F^-$	–16.0	24.3	–40.3	–0.41	1.838	0.500	–0.032	104.4	99.5	–7.9
$Cl_2O\bullet\bullet\bullet Cl^-$	–6.5	24.5	–31.0	–0.41	2.172	0.491	–0.012	105.5	105.5	–6.6
$Cl_2O\bullet\bullet\bullet Br^-$	–11.0	46.5	–57.5	–0.62	1.966	0.878	0.009	105.7	110.8	–6.6
$Br_2O\bullet\bullet\bullet F^-$	–12.9	4.5	–17.4	–0.26	2.162	0.153	0.007	106.1	86.6	–8.0
$Br_2O\bullet\bullet\bullet Cl^-$	–6.0	1.5	–7.6	–0.19	2.673	0.084	0.021	111.9	94.0	–2.2
$Br_2O\bullet\bullet\bullet Br^-$	–6.2	20.6	–26.7	–0.44	2.243	0.425	0.026	108.2	108.2	–5.9
$F_2S\bullet\bullet\bullet F^-$	–50.1	16.2	–66.3	–0.35	1.813	0.227	0.045	87.0	87.0	–11.2
$F_2S\bullet\bullet\bullet Cl^-$	–23.1	8.5	–31.7	–0.21	2.452	0.149	0.031	89.3	88.2	–8.9
$F_2S\bullet\bullet\bullet Br^-$	–19.8	7.1	–26.9	–0.19	2.647	0.135	0.028	90.1	88.7	–8.1
$Cl_2S\bullet\bullet\bullet F^-$	–53.1	24.5	–77.5	–0.47	1.748	0.461	0.035	92.1	93.0	–11.5
$Cl_2S\bullet\bullet\bullet Cl^-$	–25.3	14.8	–40.1	–0.34	2.339	0.323	0.032	94.4	94.4	–9.2
$Cl_2S\bullet\bullet\bullet Br^-$	–22.4	14.4	–36.9	–0.34	2.506	0.322	0.030	94.9	95.1	–8.7
$Br_2S\bullet\bullet\bullet F^-$	–51.7	22.2	–73.9	–0.51	1.743	0.487	0.028	92.8	93.9	–11.1
$Br_2S\bullet\bullet\bullet Cl^-$	–24.7	12.2	–36.8	–0.36	2.346	0.320	0.027	95.6	95.3	–8.3
$Br_2S\bullet\bullet\bullet Br^-$	–22.3	12.3	–34.6	–0.36	2.507	0.327	0.027	96.0	96.0	–7.9
$F_2Te\bullet\bullet\bullet F^-$	–72.4	7.9	–80.3	–0.32	2.054	0.162	0.038	84.2	84.2	–9.7
$F_2Te\bullet\bullet\bullet Cl^-$	–42.5	5.9	–48.5	–0.24	2.608	0.134	0.035	85.2	86.3	–8.7
$F_2Te\bullet\bullet\bullet Br^-$	–38.1	5.6	–43.7	–0.24	2.777	0.130	0.034	85.2	86.6	–8.7
$Cl_2Te\bullet\bullet\bullet F^-$	–73.3	10.8	–84.1	–0.39	2.039	0.285	0.047	90.0	88.5	–8.2
$Cl_2Te\bullet\bullet\bullet Cl^-$	–43.0	8.6	–51.6	–0.30	2.582	0.249	0.045	91.4	91.4	–6.8
$Cl_2Te\bullet\bullet\bullet Br^-$	–38.6	8.4	–47.1	–0.30	2.745	0.246	0.045	91.4	91.8	–6.8
$Br_2Te\bullet\bullet\bullet F^-$	–72.0	9.9	–81.9	–0.41	2.040	0.227	0.045	90.8	88.5	–8.3
$Br_2Te\bullet\bullet\bullet Cl^-$	–42.0	7.6	–49.6	–0.32	2.582	0.461	0.035	92.5	92.0	–6.6
$Br_2Te\bullet\bullet\bullet Br^-$	–37.7	7.6	–45.3	–0.32	2.751	0.487	0.028	92.8	92.8	–6.3

[a] Computed at ZORA-M06/QZ4P. For full set of data, see Appendices 4.1 and 4.2.

In general, chalcogen bonds become stronger on descending group 16 in the periodic table, in agreement with previous *ab initio* results.[4b,17] The heavier $D_2Ch\bullet\bullet\bullet A^-$ chalcogen bonds (*i.e.*, Ch = S, Se, and Te) become weaker and longer as the accepting halide (A^-) varies from F^- to Br^-. In the case of the tellurium-bonded complexes $D_2Te\cdots A^-$, for example, the ΔE

weakens from around –73 kcal mol^{-1} for $A^- = F^-$ to around –38 kcal mol^{-1} for $A^- = Br^-$ (see Table 4.1). However, the oxygen chalcogen bonds $D_2O{\bullet\bullet\bullet}A^-$ display a more complex dependency of ΔE upon variation of the accepting halide A^-. From $A^- = F^-$ to Cl^-, the oxygen-bond strength still weakens, similar to the situation for the heavier chalcogen bonds. However, thereafter, from $A^- = Cl^-$ to Br^-, the oxygen-bond strength does not weaken but instead becomes stronger. This is most clearly seen in the series constituted by the complex $F_2O{\bullet\bullet\bullet}A^-$ between an oxygen molecule and a halide ion. Here, ΔE for the oxygen-bond strength varies along $A^- = F^-$, Cl^-, and Br^- with values of –21.9, –9.9, and –11.5 kcal mol^{-1}, respectively (see Table 4.1).

When the substituent D is varied from D = F to D = Br, the heavier chalcogen bond strength (*i.e.* Ch = S, Se, and Te) changes only slightly (see Table 4.1 and Appendix 4.1). For example, along the series from $F_2Te{\bullet\bullet\bullet}F^-$ to $Br_2Te{\bullet\bullet\bullet}F^-$, the tellurium bond strength varies only from a ΔE value of –72.4 to –72.0 kcal mol^{-1}, the tellurium-bond distance $r_{Ch\cdots A}$ decreases in value from 2.054 to 2.040 Å, and the stretch Δr_{D^1-Ch} increases in value from 0.162 to 0.227 Å. An exception to this is again the oxygen bond $D_2O{\bullet\bullet\bullet}A^-$, which becomes weaker and longer as D is varied from F to Br (see Table 4.1). For example, along the series from $F_2O{\bullet\bullet\bullet}F^-$ to $Br_2O{\bullet\bullet\bullet}F^-$, the oxygen-bond strength weakens from a ΔE value of –21.9 to only –12.9 kcal mol^{-1}, the oxygen-bond distance $r_{Ch\cdots A}$ increases in value from 1.784 to 2.162 Å, and the stretch Δr_{D^1-Ch} decreases in value from 0.408 to 0.153 Å.

Bond analyses with variation of Ch

The strengthening of chalcogen bonds $D_2Ch{\bullet\bullet\bullet}A^-$, as Ch varies along O, S, Se, and Te, with no change in the donating atom (D) and the accepting halide (A^-), is related to the increasing electronegativity difference across the D–Ch bonds as Ch descends in the periodic table, which is translated into two main effects. Firstly, this causes the Ch atom to become increasingly positive along O, S, Se, and Te (see VDD atomic charges in Table 4.2), resulting in a greater electrostatic attraction. Secondly, this causes, among other effects that will be explained later, the σ* D–Ch antibonding 4a' acceptor orbital to have higher amplitude on Ch (see Figure 4.1), resulting in stronger HOMO–LUMO orbital interactions.

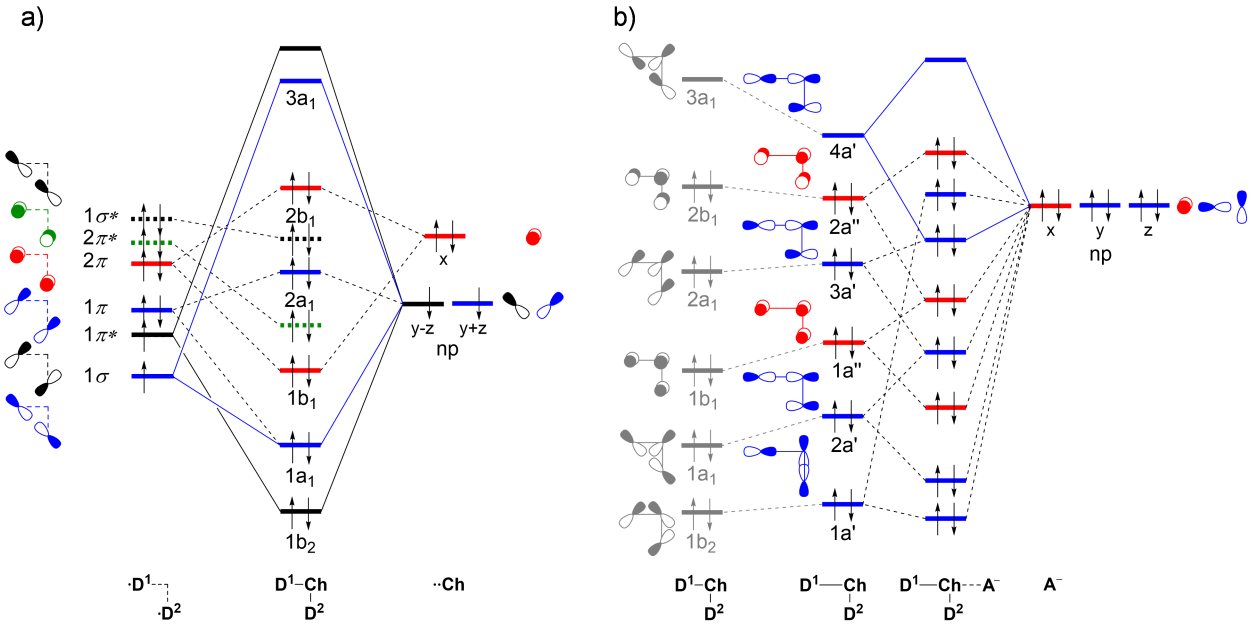

Figure 4.1. Schematic molecular orbital diagram for a) isolated D_2Ch fragments at C_{2v} symmetry (blue: a_1; green: a_2; red: b_1; black: b_2) and b) D_2Ch•••A^- complexes. The first column in (b) refers to the isolated D_2Ch fragment and the second column refers to the D_2Ch fragment deformed to its C_s symmetric geometry in the complex (blue: a'; red: a''), in which one D–Ch bond has been elongated. See Appendix 4.3 for the 3D isosurfaces of the orbitals.

Table 4.2. Bond lengths (in Å), bond angle (in deg.), VDD charge (in a.u.), orbital energies (in eV) and the homolytic bond dissociation energy without ZPE (in kcal mol^{-1}) of isolated D_2Ch fragments[a]

D_2Ch	$r_{D–Ch}$	Θ_1	Q_{Ch}^{VDD}	$\varepsilon(1a_1)$	$\varepsilon(3a_1)$	$\varepsilon(1b_1)$	$\varepsilon(2b_1)$	$BDE_{D–Ch}$[b]
F_2O	1.376	103.7	0.09	–16.6	–2.0	–15.8	–9.6	38.0
Cl_2O	1.681	112.3	–0.06	–13.8	–3.3	–13.2	–8.1	34.9
Br_2O	1.818	114.1	–0.13	–12.6	–3.3	–12.0	–7.7	33.7
F_2S	1.586	98.2	0.18	–15.0	–0.7	–14.5	–7.1	92.2
Cl_2S	2.016	103.6	0.12	–12.1	–2.5	–11.4	–7.1	64.0
Br_2S	2.180	103.9	0.04	–11.3	–2.7	–10.5	–7.0	51.4
F_2Se	1.730	96.3	0.28	–13.9	–1.6	–13.4	–7.2	87.6
Cl_2Se	2.155	101.1	0.21	–11.6	–2.7	–10.8	–7.0	63.2
Br_2Se	2.312	101.7	0.13	–10.8	–2.8	–10.1	–6.9	50.6
F_2Te	1.892	93.9	0.31	–13.0	–2.0	–12.7	–6.6	92.8
Cl_2Te	2.333	98.2	0.29	–11.0	–2.6	–10.3	–6.6	69.3
Br_2Te	2.492	99.1	0.22	–10.3	–2.7	–9.6	–6.4	55.7

[a] Computed at ZORA-M06/QZ4P; [b] Energy for the reaction $D_2Ch \rightarrow DCh^{\bullet} + D^{\bullet}$.

The trend in bond strength ΔE is mainly determined by the interaction energy ΔE_{int}. For example, from F_2O•••F^- to F_2Te•••F^-, ΔE is strengthened from –21.9 to –72.4 kcal mol^{-1} while ΔE_{int} is strengthened from –50.2 to –80.3 kcal mol^{-1} (see Table 4.1). The trend in ΔE is further enhanced by the strain energy (ΔE_{strain}), which becomes less destabilizing from Ch = O to Te.

However, the differences are smaller than the differences in ΔE_{int}. For example, from $F_2O{\bullet\bullet\bullet}F^-$ to $F_2Te{\bullet\bullet\bullet}F^-$, ΔE_{strain} is weakened by 20.4 kcal mol^{-1} (from 28.3 to 7.9 kcal mol^{-1}; see Table 4.1), while ΔE_{int} becomes 30.1 kcal mol^{-1} more stable.

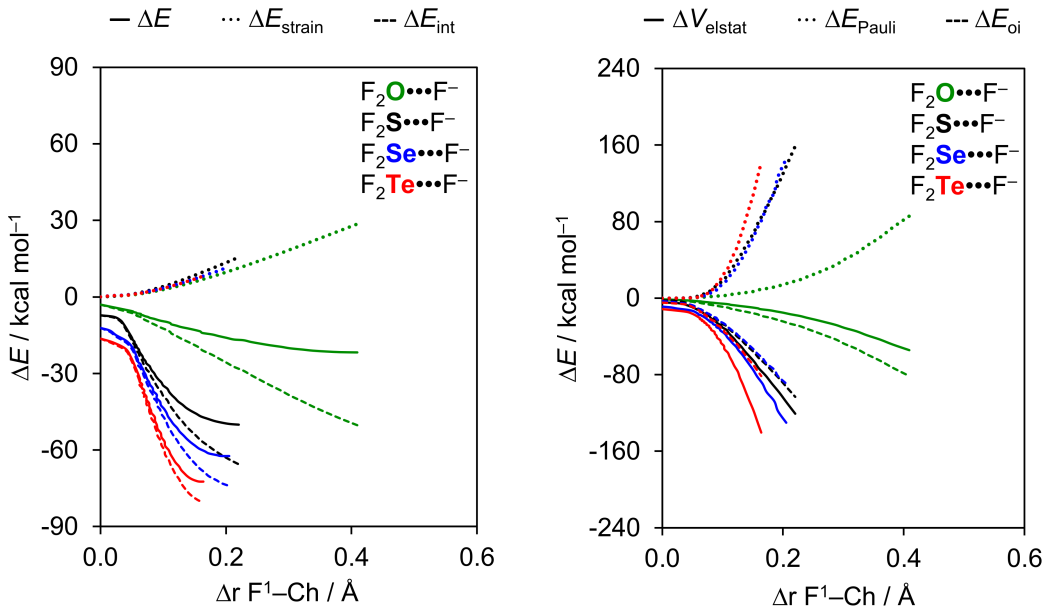

Figure 4.2. Activation strain (left panel) and energy decomposition (right panel) analyses of $F_2Ch{\bullet\bullet\bullet}F^-$ chalcogen–bonded complexes (green, Ch = O; black, Ch = S; blue, Ch = Se; red, Ch = Te).

To understand the origin of these trends, we have carried out activation strain analyses along the entire reaction coordinate ζ, projected onto the stretch in D^1–Ch bond, Δr_{Ch-D^1}, that occurs as the chalcogen-bond accepting A^- atom approaches the D_2Ch molecule (see Theoretical Methods section). The resulting activation strain diagrams (ASD) including EDA terms of the interaction are shown for a representative example series, namely, $F_2O{\bullet\bullet\bullet}F^-$ to $F_2Te{\bullet\bullet\bullet}F^-$, in Figure 4.2 (for the complete dataset, see Appendix 4.2). Again, the trend in bond energy ΔE is mainly determined by $\Delta E_{int}(\zeta)$, which strengthens when going from Ch = O to Te (Figure 4.2, left). On the other hand, the $\Delta E_{strain}(\zeta)$ curves almost coincide. However, the strain curves reach a final point at ζ_{eq}, that is, the equilibrium geometry of the complex; and here the strain energy $\Delta E_{strain}(\zeta_{eq})$ becomes more destabilizing from Ch = Te to O. Note that the trend in strain energies at the equilibrium geometries along the series of $F_2Ch{\bullet\bullet\bullet}F^-$ complexes (see Table 4.1) arises mainly from changes in the steepness of the interaction curves, not from the relatively minor variation in the strain curves (see Figure 4.2). Thus, as the $F_2Ch{\bullet\bullet\bullet}F^-$ interaction gets weaker along Ch = Te, Se, S and O, the interaction curve becomes shallower

and the balance between strain and interaction curve, *i.e.*, the stationary point of the complex, occurs at longer and longer F–Ch distances and, consequently, more destabilizing $\Delta E_{strain}(\zeta_{eq})$ (see Table 4.1).

To understand the trends in $\Delta E_{int}(\zeta)$, we further decomposed the ΔE_{int} into the individual energy components (Figure 4.2, right). The electrostatic energy $\Delta V_{elstat}(\zeta)$ is the least stabilizing for Ch = O and then strengthens along S, Se, and Te. This can be understood by the increasing differences in electronegativity across the D–Ch bonds when going from O to Te, resulting in a larger positive charge on Ch. For example, the VDD atomic charge on Ch in F_2O, F_2S, F_2Se, and F_2Te amounts to +0.09, +0.18, +0.28, and +0.31 a.u., respectively, and becomes even more positive as the D^1–Ch bond elongates (see Figure 4.3a). Nevertheless, our analyses reveal that the chalcogen bonding mechanism is absolutely not purely electrostatic but instead has a relatively large covalent component (ΔE_{oi}), stemming mainly from the HOMO–LUMO interaction between the occupied halide np_y atomic orbital (AO) and the σ* D–Ch antibonding 4a' acceptor orbital (see Figure 4.1). The associated charge transfer from A^- to D_2Ch is reflected by the $\Delta Q_{D_2Ch}{}^{VDD}$, which is negative, *i.e.*, D_2Ch gains charge from A^- upon complexation, for all $D_2Ch{\bullet\bullet\bullet}A^-$ complexes (see Table 4.1). For example, $\Delta Q_{D_2Ch}{}^{VDD}$ is –0.37 a.u. for $F_2O{\bullet\bullet\bullet}F^-$ and –0.32 a.u. for $F_2Te{\bullet\bullet\bullet}F^-$. The HOMO–LUMO charge transfer nature of the chalcogen bond is also clearly reflected by the associated deformation density. This is illustrated by the 3D plots of the deformation densities associated with chalcogen-bond formation in $F_2S{\bullet\bullet\bullet}F^-$ and $F_2Te{\bullet\bullet\bullet}F^-$ (see Figure 4.4). As can be seen, there is charge depletion on the Lewis base F^- (and in between the $Ch{\bullet\bullet\bullet}F^-$ bond due to the Pauli repulsion[10a]) and charge accumulation on D_2Ch. Note the 3D shape of the regions of charge depletion and accumulation: they reflect the shape of the 2p-type lone pair from which the F^- Lewis base donates and the σ* D–Ch antibonding 4a' acceptor orbital on D_2Ch into which this charge is donated, respectively, in the HOMO–LUMO interaction. For the chalcogen bonded complexes, the orbital interaction term ranges from 37% for $F_2Te{\bullet\bullet\bullet}F^-$ to as much as 76% for $Br_2O{\bullet\bullet\bullet}F^-$ of the total bonding interactions (ΔE_{oi} + ΔV_{elstat}; see Appendix 4.2). As can be seen in our energy decomposition diagram, the orbital interaction curves $\Delta E_{oi}(\zeta)$ become more stabilizing from Ch = O to Te (Figure 4.2, right). The stronger orbital interaction for the heavier chalcogens is the result of the larger LUMO–HOMO overlap (*i.e.* $\langle 4a'|np_y\rangle$; see Figure 4.1 for the MO diagram which shows the np_y orbital of A^- pointing towards the D^1–Ch bond of the D_2Ch fragment) as Ch becomes more electropositive. For example, in the $Cl_2Ch{\bullet\bullet\bullet}Cl^-$ series, $\langle 4a'|np_y\rangle$ increases from 0.12 to 0.20 to 0.22 to 0.24 along Ch = O, S, Se, and Te in the equilibrium geometry (see Appendix 4.2). The larger percent

contribution of the covalent component on oxygen bonds is simply because the electrostatic attraction is relatively weak, caused by the smaller positive charge on O (see Table 4.2).

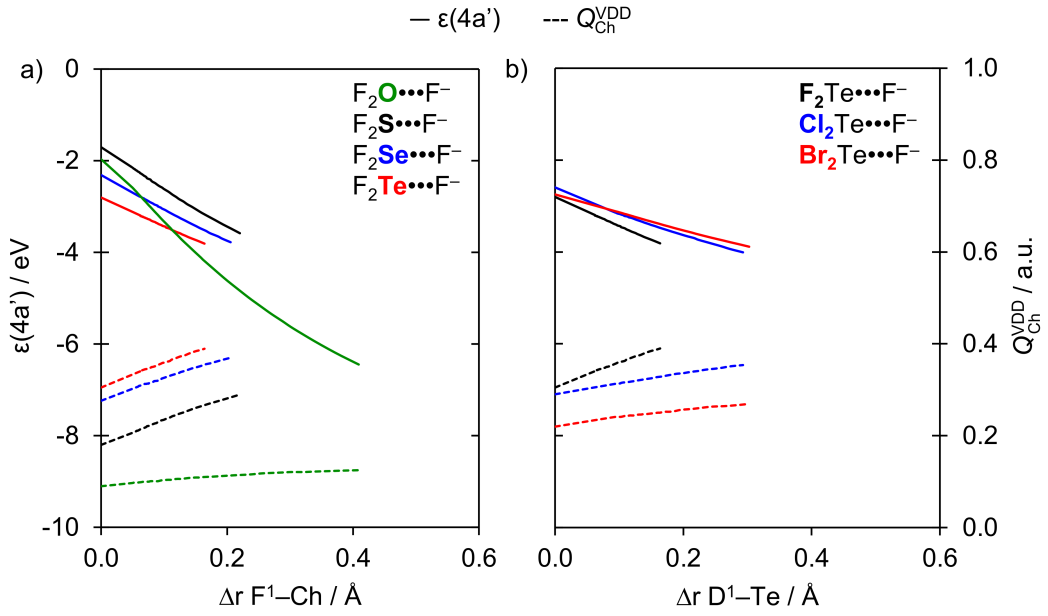

Figure 4.3. Energy of the 4a' orbital (in eV) and the VDD charge on Ch atom (in a.u.) in the neutral fragment D_2Ch projected onto a) the F^1–Ch bond stretch (green, Ch = O; black, Ch = S; blue, Ch = Se; red, Ch = Te) and b) the D^1–Te bond stretch (black, D = F; blue, D = Cl; red, D = Br).

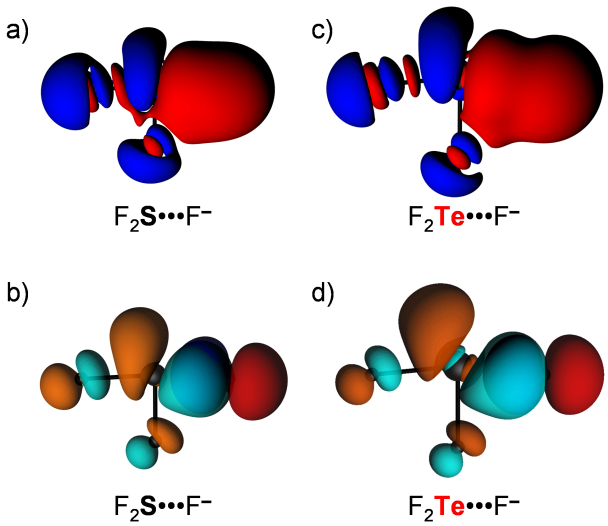

Figure 4.4. Deformation density ($\Delta\rho(r) = \rho_{[D_2Ch\cdots A^-]}(r) - \rho_{D_2Ch}(r) - \rho_{A^-}(r)$; red = depletion; blue = accumulation) plot (a and c) and HOMO–LUMO interaction (b and d) for a representative series of $D_2Ch\bullet\bullet\bullet A^-$ chalcogen bonds.

Whereas $\Delta E_{oi}(\zeta)$ becomes more stabilizing from Ch = O to Te, it becomes comparable in magnitude for all chalcogens in the equilibrium geometry $\Delta E_{oi}(\zeta_{eq})$. This is a consequence of the fact that the F^1–Ch bond expansion becomes more pronounced when going from Ch = Te to O. The increasing F^1–Ch bond expansion causes the σ* D–Ch antibonding 4a' acceptor orbital (see Figure 4.1a) to drop further in energy for lighter chalcogens, resulting in a smaller HOMO–LUMO gap and hence more stabilizing donor–acceptor interactions. This effect can be observed in Figure 4.3a, which shows the energies of the σ* F–Ch antibonding 4a' acceptor orbitals along the reaction coordinate. For Ch = S, Se, and Te, the energy of the σ* F–Ch antibonding 4a' acceptor orbital converges to an energy value of –3.8 eV as the chalcogen bond is formed. For Ch = O, on the other hand, the σ* F–O antibonding 4a' acceptor orbital energy quickly drops to a value of –6.4 eV, because the overlap between the F and O AOs is more sensitive to the D–Ch distance than for the more diffuse AOs of heavier Ch (see Figure 4.5). However, it is counteracted by the orbital overlap between the σ* D–O antibonding 4a' acceptor orbital and the np_y donor orbital, which is significantly worse for Ch = O than for other chalcogen systems (see Appendix 4.2).

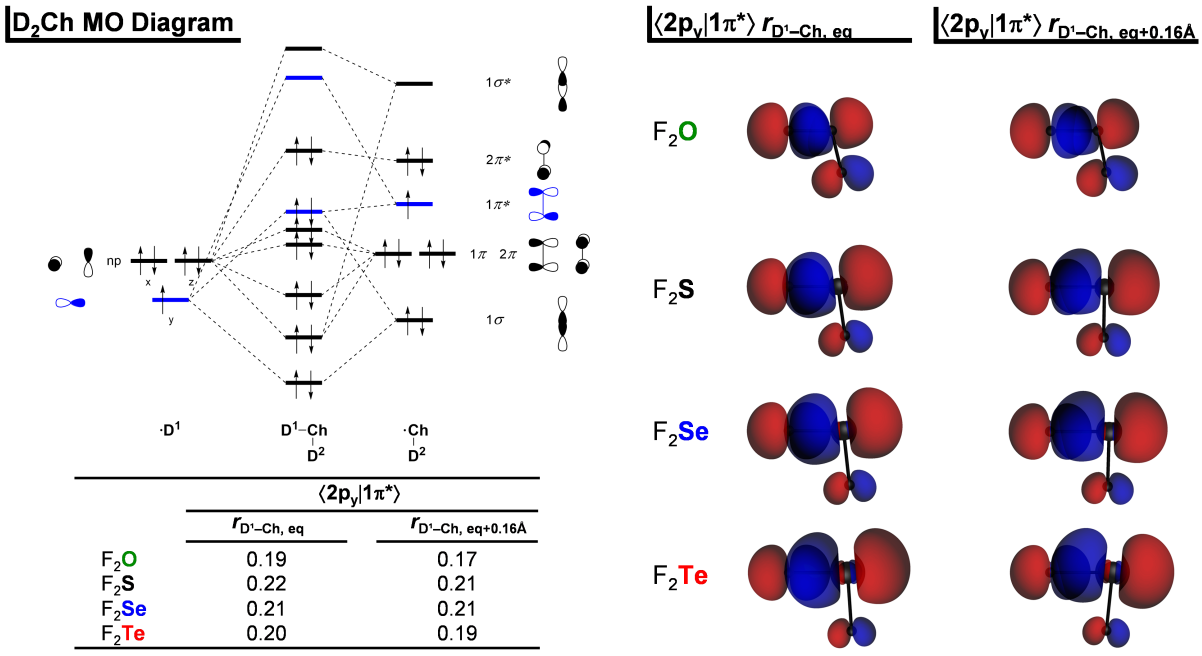

	⟨2p$_y$|1π*⟩	
	$r_{D^1\text{–Ch, eq}}$	$r_{D^1\text{–Ch, eq+0.16Å}}$
F_2O	0.19	0.17
F_2S	0.22	0.21
F_2Se	0.21	0.21
F_2Te	0.20	0.19

Figure 4.5. Orbital overlap between the $F^{1\bullet}$ and $F^2Ch^{\bullet}$ open shell fragments in the equilibrium geometries ($r_{D^1\text{–Ch, eq}}$) and with the F^1–Ch bond stretched by 0.16 Å ($r_{D^1\text{–Ch, eq+0.16Å}}$), computed at ZORA-M06/QZ4P.

Bond analyses with variation of A⁻

Our analyses show that the weakening of heavier chalcogen bonds $D_2Ch{\bullet\bullet\bullet}A^-$ (Ch = S, Se, Te), as the accepting group varies from $A^- = F^-$ to Br^-, is directly related to the concomitant reduction in electron-donating capacity of the np-type HOMO and thus the Lewis basicity of the A^- halide.[20] We recall the chalcogen bonds display both an electrostatic component (ΔV_{elstat}) and a covalent component (ΔE_{oi}). The latter stems mainly from the HOMO–LUMO interaction between the occupied halide np atomic orbital (AO) and the σ* D–Ch antibonding 4a' acceptor orbital (see Figure 4.1). Both ΔV_{elstat} and ΔE_{oi} are weakened as the halide HOMO becomes more diffuse and effectively lower in energy from $A^- = F^-$ to Br^- (see Appendix 4.2).[20b] Consequently, the interaction energy (ΔE_{int}) and, thus, the net chalcogen-bond strength ΔE becomes less stabilizing along $A^- = F^-$ to Br^- (see Table 4.1 and Appendix 4.1). This is very similar to what was found for hydrogen bonds $DH{\bullet\bullet\bullet}A^-$ and heavier halogen bonds $DX{\bullet\bullet\bullet}A^-$ (X = Cl, Br, I).[9]

The key to understanding why oxygen bonds $D_2O{\bullet\bullet\bullet}A^-$ show a more complex, partially opposite trend (*i.e.*, the expected weakening from $A^- = F^-$ to Cl^- but thereafter a strengthening along $A^- = Cl^-$ to Br^-) is contained in the counteracting effects evolving from D–O bond stretching induced in the triatomic D_2O molecule as it interacts with the halide A^-. Interestingly, activation strain analyses reveal, again, that interaction energies recover the original trend in total energies, that is, $\Delta E_{int}(\zeta)$ weakens from $A^- = F^-$ to Br^-. This can be seen in Figure 4.6 which shows the activation strain and energy decomposition diagrams along the reaction coordinate ζ projected onto the stretch $\Delta r_{D^1–Ch}$ for two representative series. Each diagram in Figure 4.6 refers to one particular F_2O or F_2Te molecule forming a chalcogen bonding with $A^- = F^-$, Cl^-, and Br^-. The ΔE_{strain} curves within each subgraph coincide because they refer to the same D–Ch bond in the same triatomic molecule being stretched as the complexation reaction progresses. Consequently, the trend $A^- = F^-$ to Br^- in the total $F_2O{\bullet\bullet\bullet}A^-$ and $F_2Te{\bullet\bullet\bullet}A^-$ energy profiles ΔE in each subgraph is directly determined by the trend in the corresponding ΔE_{int} curves.

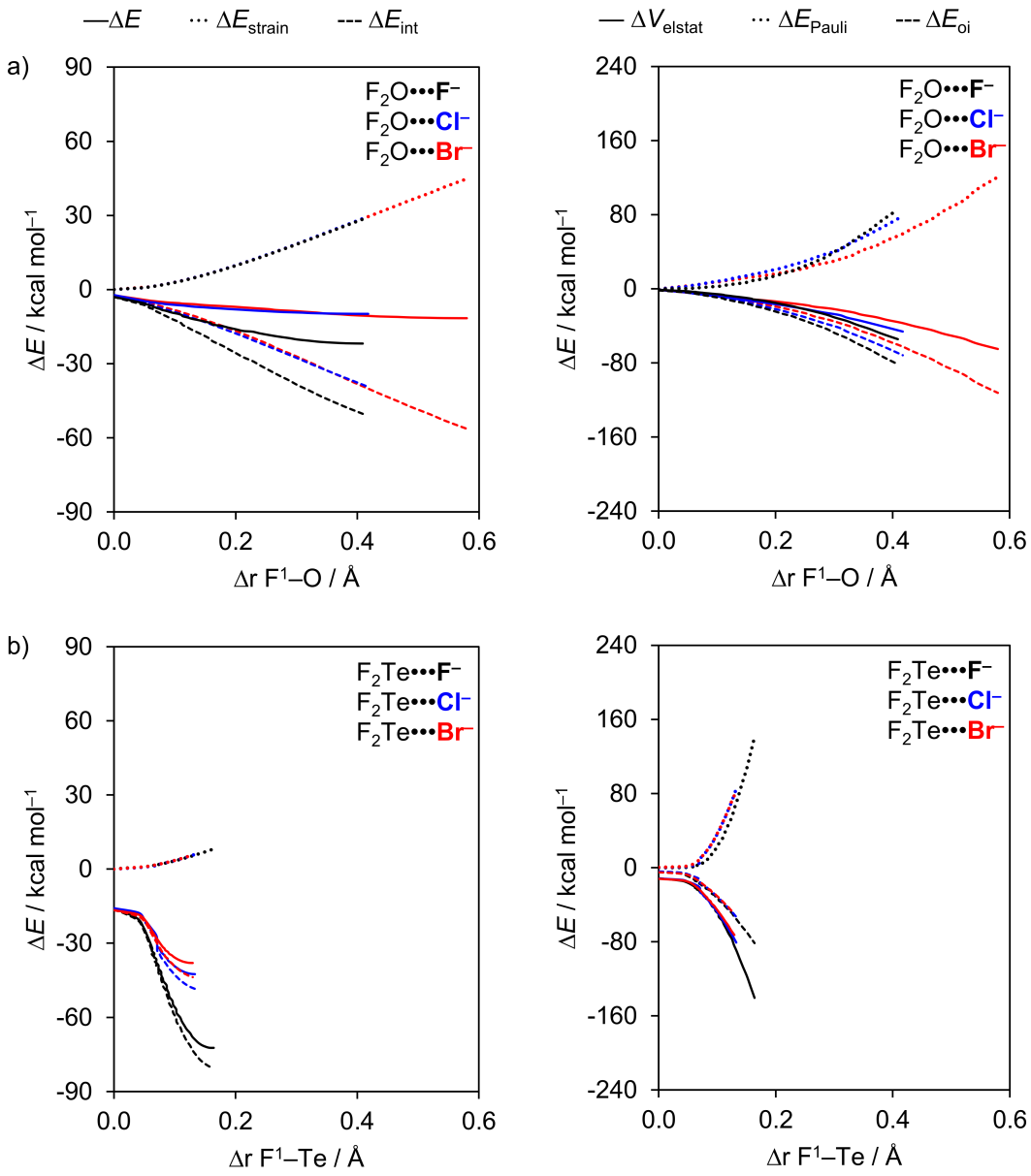

Figure 4.6. Activation strain (left panel) and energy decomposition (right panel) analyses of a) $F_2O{\bullet\bullet\bullet}A^-$ and b) $F_2Te{\bullet\bullet\bullet}A^-$ (black, $A^- = F^-$; blue, $A^- = Cl^-$; red, $A^- = Br^-$).

The reason why the oxygen bonds $D_2O{\bullet\bullet\bullet}A^-$ do not experience a weakening in ΔE_{int} from $A^- = F^-$ to Br^-, as all other chalcogen bonds, is promoted by a combination of factors: i) a weak D–O bond that is easily stretched; ii) a strong interaction with an approaching halide A^-; and iii) a σ* D–Ch antibonding 4a' acceptor orbital that drops in energy, more quickly than for other D^1–Ch bonds due to a more sensitive overlap between the D^1 and O AOs, as the D^1–O bond elongates (see Figures 4.3 and 4.5). The latter generates a stronger driving force for D^1–Ch stretching in $D_2Ch{\bullet\bullet\bullet}A^-$ because this deformation enhances the orbital interactions and thus ΔE_{int}. Note that, for $D_2O{\bullet\bullet\bullet}A^-$, ΔE_{oi} is the strongest bonding component and that the $\Delta E_{oi}(\xi)$

curves directly reflect the electron-donating capacity of the np-type HOMO of the A^- halides, that is, the ΔE_{oi} curves become more stabilizing from $A^- = Br^-$ to F^- (see Figure 4.6). Indeed, D^1–Ch stretching is most pronounced if this bond in the neutral fragment is weaker, that is, for the weaker chalcogen bonds (*e.g.*, ca. 38 kcal mol^{-1} for F–O, ca. 35 kcal mol^{-1} for Cl–O and ca. 34 kcal mol^{-1} for Br–O; see Table 4.2). In this case, it is able to affect the trend in overall bond strength ΔE. The D^1–O stretching in oxygen-bonded complexes is most pronounced in the $Cl_2O{\bullet\bullet\bullet}A^-$ series, along which the Cl^1–O stretch Δr_{D^1-Ch} varies between 0.5 and 0.9 Å, but it is already relevant in the $F_2O{\bullet\bullet\bullet}A^-$ series in which the F^1–O stretch Δr_{Ch-D^1} varies between 0.4 and 0.6 Å from $A^- = F^-$ to Br^- (see Table 4.1).

We conclude that, in general, chalcogen bonds $D_2Ch{\bullet\bullet\bullet}A^-$ become weaker along $A^- = F^-$ to Br^- because the larger radii and lower np AO energies of the halides lead to weaker electrostatic attraction and weaker orbital interactions. The trend in $D_2O{\bullet\bullet\bullet}A^-$ oxygen bond strength is partially inverted, that is, ΔE becomes more stabilizing along $A^- = Cl^-$ and Br^- because of a subtler interplay of factors. Notably, a significant stretching of the relatively weak D–O bonds in the $D_2O{\bullet\bullet\bullet}A^-$ equilibrium structures lowers the σ* D–O antibonding 4a' acceptor orbital and thus amplifies the donor-acceptor orbital interactions.

Bond analyses with variation of D

The strength of the heavier chalcogen bonds $D_2Ch{\bullet\bullet\bullet}A^-$ varies little when going from D = F to Br because the Cl–Ch and Br–Ch bonds are significantly weaker than the F–Ch. This allows the Cl–Ch and Br–Ch bonds to stretch to a higher extent and, therefore, to have more stabilizing electrostatic attraction and orbital interactions. For the oxygen bonds $D_2O{\bullet\bullet\bullet}A^-$, the bond energy is weakened along the same variation because the D–Ch bond strength are all comparable (see Table 4.2). In both cases, the trend in bond strength ΔE is determined by the interaction energy ΔE_{int}. For example, from $F_2O{\bullet\bullet\bullet}F^-$ to $Br_2O{\bullet\bullet\bullet}F^-$, ΔE_{int} is weakened from –50.2 to –17.4 kcal mol^{-1}, respectively, whereas from $F_2Te{\bullet\bullet\bullet}F^-$ to $Br_2Te{\bullet\bullet\bullet}F^-$, the bond energy only changes from –80.3 to –81.9 kcal mol^{-1}, respectively (see Table 4.1). The strain energy (ΔE_{strain}) is not negligible, but it does not offset the trend set by ΔE_{int}. Our activation strain analyses explain the above differences between oxygen and heavier chalcogen bonds (see Figure 4.7).

Starting with some general observations, we find that for oxygen, as well as heavier chalcogen bonds, the ΔE_{strain} curves are most unfavorable when D = F and gradually become less destabilizing as the donating atom is varied along D = F, Cl, and Br (see Figure 4.7).

Furthermore, for all $D_2Ch{\bullet\bullet\bullet}A^-$ complexes, the ΔE_{int} curves become less stabilizing along D = F, Cl, and Br. The resulting energy profiles of $D_2Ch{\bullet\bullet\bullet}A^-$ depend on the balance between both ΔE_{strain} and ΔE_{int}, but the interaction energy curves already show a very similar trend to ΔE.

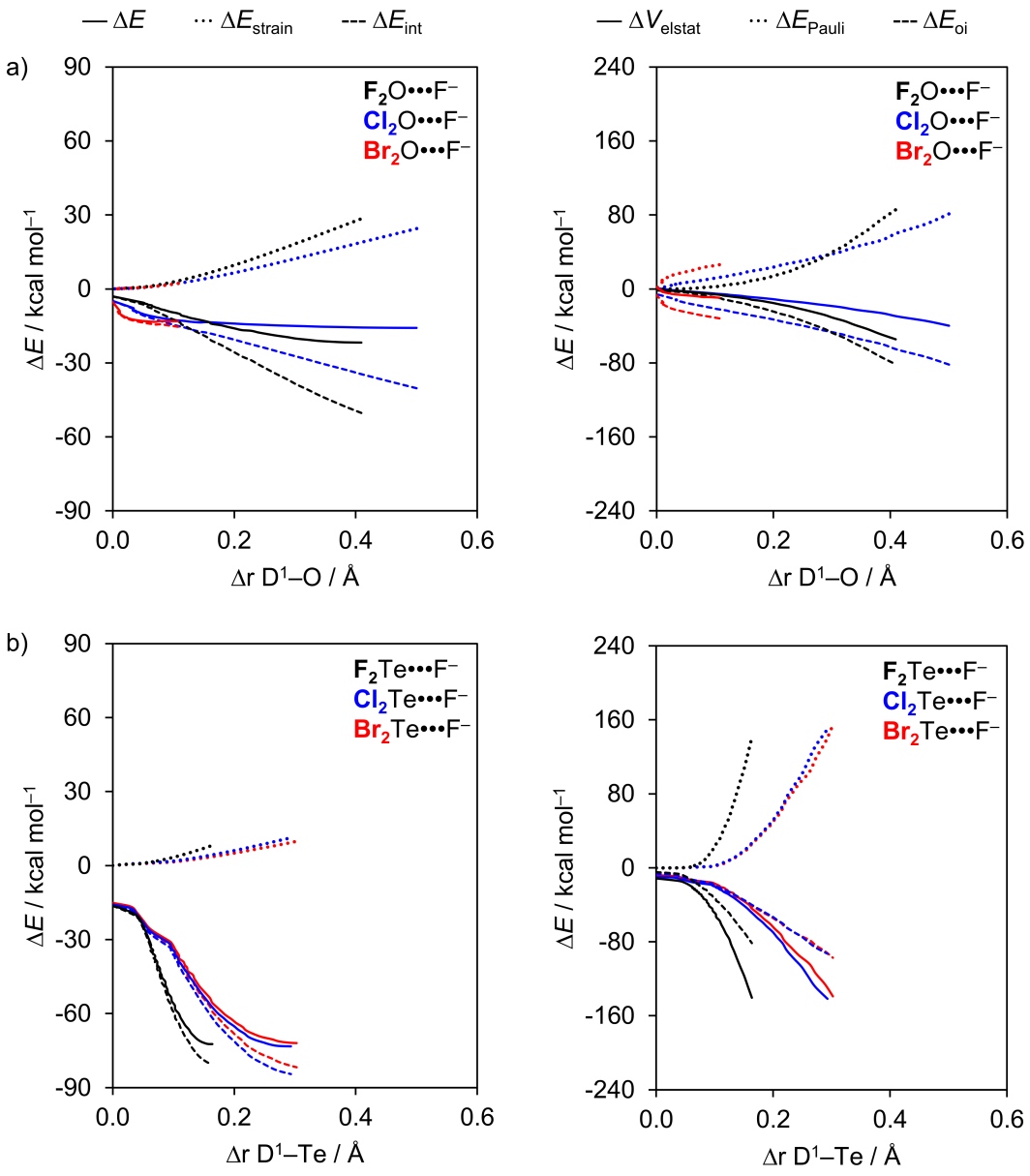

Figure 4.7. Activation strain (left panel) and energy decomposition (right panel) analyses of a) $D_2O{\bullet\bullet\bullet}F^-$ and b) $D_2Te{\bullet\bullet\bullet}F^-$ (black, D = F; blue, D = Cl; red, D = Br).

The slope and shape of the ΔE_{strain} curves is of course directly related to the D^1–Ch bond strength of the neutral fragment, which in general becomes stronger as the polarity across the D–Ch bond increases[21] (see Table 4.2). From F_2Ch to Br_2Ch, where Ch is S, Se or Te, the

halogen-chalcogen bond strength decreases significantly from a value of ca. 93 to 50 kcal mol^{-1} (Table 4.2). The corresponding halogen–oxygen bonds are all much weaker, and variations in the homolytic bond dissociation energy (BDE) are also much smaller. From F_2O to Br_2O, the bond strength decreases from 38.0 to 33.7 kcal mol^{-1}. Thus, for the heavier chalcogen-bonded complexes, where Ch is S, Se, or Te, the ΔE_{strain} curves show a pronounced reduction in slope from F_2Ch to Br_2Ch, which, in the corresponding chalcogen-bonded complexes $F_2Ch{\bullet\bullet\bullet}A^-$ to $Br_2Ch{\bullet\bullet\bullet}A^-$, translates into an increasing stretch Δr_{D^1-Ch} of the neutral fragment. As the stretch Δr_{D^1-Ch} becomes larger from equilibrium structures $F_2Ch{\bullet\bullet\bullet}A^-$ to $Br_2Ch{\bullet\bullet\bullet}A^-$, the ΔE_{int} curves have been able to descend further, to lower, more stabilizing energies. This stabilization is, of course, related to the ΔV_{elstat} and ΔE_{oi}. Note that the electrostatic attraction and orbital interaction curves become less stabilizing along D = F, Cl, and Br, but turn out to have comparable strength in the equilibrium structures, because the D^1–Ch bonds have been increasingly stretched in the latter, that is, in $Cl_2Ch{\bullet\bullet\bullet}A^-$ and $Br_2Ch{\bullet\bullet\bullet}A^-$. The bonding components ΔV_{elstat} and ΔE_{oi} are the most stabilizing for D = F because of the larger difference in electronegativity across the D–Ch bonds (*vide supra*). However, the ΔE_{oi} is able to further stabilize for D = Cl and Br because, in the equilibrium structure of the chalcogen-bonded complexes, the Cl–Ch and Br–Ch bonds expand to a higher extent, resulting in a stronger stabilization of their σ* D–Ch antibonding 4a' acceptor orbitals (see Figure 4.3b). Furthermore, the VDD atomic charge on Ch becomes increasingly more positive as the D^1–Ch bond expands, which translates into more stabilizing ΔV_{elstat} for D = Cl and Br in the equilibrium geometry. The final result is, thus, a comparable stability among heavier chalcogen bonds $D_2Ch{\bullet\bullet\bullet}A^-$ complexes when the substituent D is varied from F to Br.

Chalcogen bonds versus halogen and hydrogen bonds

Our analyses highlight that chalcogen bonds, halogen bonds, and hydrogen bonds are all similar in nature.[9] Each of these bonds in our set of model systems has a significant covalent component in addition to electrostatic attraction and can range in strength roughly between –6 and –70 kcal mol^{-1} (see Figure 4.8). Chalcogen bonds and halogen bonds have a larger range in polarities in D–Ch and D–X than in D–H bonds and are in general stronger than hydrogen bonds because of more stabilizing orbital interactions (see Appendix 4.4 for bond energies ΔE of a representative series of XB and HB ΔE computed at ZORA-M06/QZ4P). However, chalcogen bonds and halogen bonds also have more destabilizing Pauli repulsion because the lone-pair HOMO of the Lewis base overlaps with more closed shells, in particular, with the σ D–Ch bonding 3a' and 2a' FMOs or σ D–X bonding FMO with a higher amplitude on Ch and

X, respectively, than the amplitude of σ D–H bonding FMO has on H (see Figure 4.8; see also Ref. 9). Our analyses provide a unified picture for chalcogen bonds, halogen bonds, and hydrogen bonds based on quantitative Kohn-Sham molecular orbital theory, which proves that these intermolecular interactions cannot be described by a pure and simple electrostatic model.

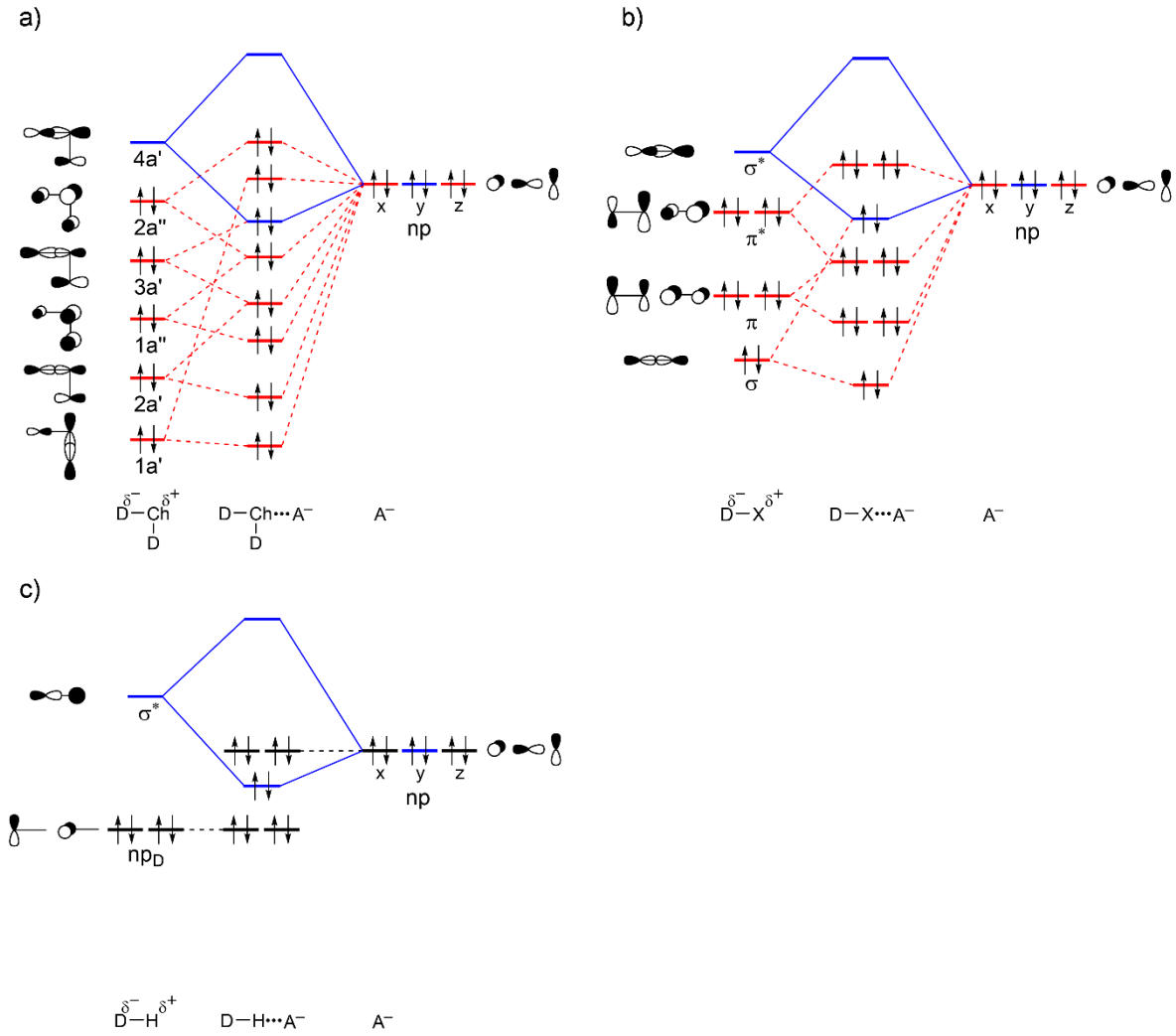

Figure 4.8. Generic molecular orbital diagrams for a) $D_2Ch{\bullet\bullet\bullet}A^-$ chalcogen bonds, b) $DX{\bullet\bullet\bullet}A^-$ halogen bonds, and c) $DH{\bullet\bullet\bullet}A^-$ hydrogen bonds.

4.4 Conclusion

Chalcogen bonds in $D_2Ch{\bullet\bullet\bullet}A^-$ range between 6 and 73 kcal mol^{-1} in strength, becoming stronger as the chalcogen atom becomes more electropositive, along Ch = O, S, Se and Te, and also as the halide becomes a stronger Lewis base, along A^- = Br^-, Cl^- and F^-. The trend upon variation of the substituent along D = F, Cl, Br is less pronounced, as are all trends for the

relatively weak oxygen bonds. This follows from our bonding analyses based on relativistic density functional theory (DFT) calculations at ZORA-M06/QZ4P.

Our activation-strain and quantitative Kohn-Sham MO bonding analyses reveal that the chalcogen bonds in $D_2Ch•••A^-$ are similar in nature to halogen bonds in $DX•••A^-$ and hydrogen bonds in $DH•••A^-$ (Ch = O, S, Se, Te; D, X, A = F, Cl, Br). Chalcogen bonds are far from being solely electrostatic phenomena. Similar to halogen and hydrogen bonds, chalcogen bonds have a sizeable covalent component, ranging up to 80% of the bonding components ($\Delta V_{elstat} + \Delta E_{oi}$), stemming from HOMO–LUMO interactions between the np-type lone pair on the bond accepting fragment A^- and the LUMO with strong D–Ch □* anti-bonding character on the bond donating fragment D_2Ch.

Chalcogen bonds become stronger for heavier Ch because of the greater difference in electronegativity across the D–Ch bonds, causing: i) the σ* D–Ch antibonding 4a' acceptor orbital to have higher amplitude on Ch, enhancing HOMO–LUMO orbital interactions; and ii) the Ch to become more positively charged, resulting in greater electrostatic attraction when descending in group 16 of the periodic table. The chalcogen bonds also become stronger for lighter A^- because the electron-donating capacity of the np-type HOMO (*i.e.* Lewis basicity) of the halides increases ascending group 17 in the periodic table. The trends for oxygen bonds, as well as along various D, are less pronounced because of counteracting effects or small values in bond strength.

4.5 References

[1] L. Vogel, P. Wonner, S. M. Huber, *Angew. Chem.* **2019**, *131*, 1896–1907; *Angew. Chem. Int. Ed*. **2019**, *58*, 1880–1891.

[2] a) R. E. Rosenfield, R. Parthasarathy, J. D. Dunitz, *J. Am. Chem. Soc*. **1977**, *99*, 4860–4862; b) T. N. Guru Row, R. Parthasarathy, *J. Am. Chem. Soc*. **1981**, *103*, 477–479; c) J. G. Ángyan, R. A. Poirier, A. Kucsman, I. G. Csizmadia, *J. Am. Chem. Soc*. **1987**, *109*, 2237–2245.

[3] a) P. Politzer, J. S. Murray, T. Clark, *Phys. Chem. Chem. Phys*. **2013**, *15*, 11178–11189; b) P. Politzer, J. S. Murray, M. C. Concha, *J. Mol. Model*. **2008**, *14*, 659–665; c) P. Politzer, J. S. Murray, T. Clark, *J. Phys. Chem. A* **2019**, *123*, 10123–10130; d) S. Scheiner, M. Michalczyk, W. Zierkiewicz, *Coord. Chem. Rev.* **2020**, *405*, 213136.

[4] a) V. Oliveira, D. Cremer, E. Kraka, *J. Phys. Chem. A* **2017**, *121*, 6845–6862; b) M. Bortoli, S. M. Ahmad, T. A. Hamlin, F. M. Bickelhaupt, L. Orian, *Phys. Chem. Chem. Phys*. **2018**, *20*, 27592–27599; c) D. J. Pascoe, K. B. Ling, S. L. Cockroft, *J. Am. Chem. Soc*. **2017**, *139*, 15160–15167.

[5] a) R. Gleiter, G. Haberhauer, D. B. Werz, F. Rominger, C. Bleiholder, *Chem. Rev*. **2018**, *118*, 2010–2041; b) L. -J. Riwar, N. Trapp, K. Root, R. Zenobi, F. Diederich, *Angew. Chem.* **2018**, *130*, 17506–17512; *Angew. Chem. Int. Ed*. **2018**, *57*, 17259–17264; c) R. Shukla, D. Chopra,

Cryst. Growth Des. **2016**, *16*, 6734–6742; d) J. Fanfrlík, A. Přáda, Z. Padělková, A. Pecina, J. Macháček, M. Lepšík, J. Holub, A. Růžička, D. Hnyk, P. Hobza, *Angew. Chem. Int. Ed*. **2014**, *53*, 10139–10142; e) S. P. Thomas, V. Kumar, K. Alhameedi, T. N. Guru Row, *Chem. Eur. J*. **2019**, *25*, 3591–3597; f) P. Scilabra, J. S. Murray, G. Terraneo, G. Resnati, *Cryst. Growth Des*. **2019**, *19*, 1149–1154. (g) F. -U. Rahman, D. Tzeli, I. D. Petsalakis, G. Theodorakopoulos, P. Ballester, J. Rebek Jr., Y. Yu, *J. Am. Chem. Soc.* **2020**, *142*, 5876–5883. (h) R. Zeng, Z. Gong, Q. Yan, *J. Org. Chem.* **2020**, *85*, 8397–8404; (i) P. C. Ho, J. Z. Wang, F. Meloni, I. Vargas-Baca, *Coord. Chem. Rev.* **2020**, *422*, 213464; (j) S. Mehrparvar, C. Wölper, R. Gleiter, G. Haberhauer, *Angew. Chem.* **2020**, *132*, 17303–17311; *Angew. Chem. Int. Ed*. **2020**, *59*, 17154–17161.

[6] a) S. Benz, M. Macchione, Q. Verolet, J. Mareda, N. Sakai and S. Matile, *J. Am. Chem. Soc*. **2016**, *138*, 9093–9096; b) M. Macchione, M. Tsemperouli, A. Goujon, A. R. Mallia, N. Sakai, K. Sugihara and S. Matile, *Helv. Chim. Acta* **2018**, *101*, e1800014; c) M. Iwaoka, in *Noncovalent Forces. Challenges and Advances in Computational Chemistry and Physics*, *Vol*. 19 (Eds.: S. Scheiner), Springer, Cham, **2015**, pp. 265–289; d) L. M. Lee, M. Tsemperouli, A. I. Poblador-Bahamonde, S. Benz, N. Sakai, K. Sugihara and S. Matile, *J. Am. Chem. Soc*. **2019**, *141*, 810–814; e) P. B. Lutz and C. A. Bayse, *J. Inorg. Biochem*. **2016**, *157*, 94–103; f) M. Iwaoka and N. Babe, *Phosphorus*, *Sulfur, and Silicon* **2015**, *190*, 1257–1264; g) S. P. Thomas, D. Jayatilaka and T. N. Guru Row, *Phys. Chem. Chem. Phys*. **2015**, *17*, 25411–25420; h) A. Lange, M. Günther, F. M. Büttner, M. O. Zimmermann, J. Heidrich, S. Hennig, S. Zahn, C. Schall, A. Sievers-Engler, F. Ansideri, P. Koch, M. Lämmerhofer, T. Stehle, S. A. Laufer, F. M. Boeckler, *J. Am. Chem. Soc*. **2015**, *137*, 14640–14652; (i) B. Galmés, A. Juan-Bals, A. Frontera, G. Resnati, *Chem. Eur. J.* **2020**, *26*, 4599–4606.

[7] a) Y. Cheng, Y. Qi, Y. Tang, C. Zheng, Y. Wan, W. Huang, R. Chen, *J. Phys. Chem. Lett*. **2016**, *7*, 3609–3615; b) J. Noh, S. Jung, D. G. Koo, G. Kim, K. S. Choi, J. H. Park, T. J. Shin, C. Yang and J. Park, *Sci. Rep*. **2018**, *8*, 1–11; c) K. Strakova, L. Assies, A. Goujon, F. Piazzolla, H. V. Humeniuk, S. Matile, *Chem. Rev*. **2019**, *119*, 10977–11005; d) G. E. Garrett, G. L. Gibson, R. N. Straus, D. S. Seferos and M. S. Taylor, *J. Am. Chem. Soc.* **2015**, *137*, 4126–4133.

[8] a) J. Bamberger, F. Ostler, O. G. Mancheño, *ChemCatChem* **2019**, *11*, 5198–5211; b) K. T. Mahmudov, M. N. Kopylovich, M. F. C. Guedes Da Silva, A. J. L. Pombeiro, *Dalt. Trans*. **2017**, *46*, 10121–10138; c) S. Benz, J. López-Andarias, J. Mareda, N. Sakai, S. Matile, *Angew. Chem.* **2017**, *129*, 830–833; *Angew. Chem. Int. Ed*. **2017**, *56*, 812–815; (d) W. Wang, H. Zhu, L. Feng, Q. Yu, J. Hao, R. Zhu, Y. Wang, *J. Am. Chem. Soc.* **2020**, *142*, 3117–3124; (e) Y. Li, L. Meng, C. Sun, Y. Zeng, *J. Phys. Chem. A* **2020**, *124*, 3815–3824.

[9] L. P. Wolters, F. M. Bickelhaupt, *ChemistryOpen* **2012**, *1*, 96–105.

[10] a) F. M. Bickelhaupt, *J. Comput. Chem*. **1999**, *20*, 114–128; b) W. -J. van Zeist, F. M. Bickelhaupt, *Org. Biomol. Chem*. **2010**, *8*, 3118–3127; c) P. Vermeeren, S. C. C. van der Lubbe; C. Fonseca Guerra, F. M. Bickelhaupt, T. A. Hamlin, *Nat. Protoc.* **2020**, *15*, 649–667.

[11] a) F. M. Bickelhaupt, E. J. Baerends, in *Reviews in Computational Chemistry*, *Vol*. 15 (Eds.: K. B. Lipkowitz, D. B. Boyd), Wiley-VCH, New York, **2000**, pp. 1–86; b) F.M. Bickelhaupt, N. M. M. Nibbering, E. M. van Wezenbeek, E.J. Baerends, *J. Phys. Chem*. **1992**, *96*, 4864–4873; c) A. Krapp, F. M. Bickelhaupt, G. Frenking, *Chem. Eur. J*. **2006**, *12*, 9196–9216.

[12] a) T. Ziegler, A. Rauk, *Inorg. Chem*. **1979**, *18*, 1558–1565; b) T. Ziegler, A. Rauk, *Inorg. Chem*. **1979**, *18*, 1755–1759; c) T. Ziegler, A. Rauk, *Theor. Chim. Acta* **1977**, *46*, 1–10.

[13] a) G. te Velde, F. M. Bickelhaupt, E. J. Baerends, C. Fonseca Guerra, S. J. A. van Gisbergen, J. G. Snijders, T. Ziegler, *J. Comput. Chem*. **2001**, *22*, 931–967; b) C. Fonseca Guerra, J. G. Snijders, G. te Velde, E. J. Baerends, *Theor. Chem. Acc*. **1998**, *99*, 391–403; c) ADF2017, SCM

Theoretical Chemistry; Vrije Universiteit: Amsterdam, The Netherlands, **2017**; http://www.scm.com.

[14] a) Y. Zhao, D. G. Truhlar, *Theor. Chem. Acc.* **2008**, *120*, 215–241; b) Y. Zhao, D. G. Truhlar, *J. Chem. Phys.* **2006**, *125*, 194101.

[15] E. van Lenthe, E. J. Baerends, *J. Comput. Chem.* **2003**, *24*, 1142–1156.

[16] E. van Lenthe, E. J. Baerends, J. G. Snijders, *J. Chem. Phys.* **1994**, *101*, 9783–9792.

[17] L. de Azevedo Santos, T. C. Ramalho, T. A. Hamlin, F. M. Bickelhaupt, *J. Comput. Chem*. **2021**, *42*, 688–698.

[18] X. Sun, T. M. Soini, J. Poater, T. A. Hamlin, F. M. Bickelhaupt, *J. Comput. Chem.* **2019**, *40*, 2227–2233.

[19] a) F. M. Bickelhaupt, N. J. R van Eikema Hommes, C. Fonseca Guerra, E. J Baerends, *Organometallics* **1996**, *15*, 2923–2931; b) C. Fonseca Guerra, J. -W. Handgraaf, E. J. Baerends, F. M. Bickelhaupt, *J. Comput. Chem*. **2004**, *25*, 189–210.

[20] a) M. Swart, F. M. Bickelhaupt, *J. Chem. Theory Comput.* **2006**, *2*, 281–287; b) W. J. van Zeist, Y. Ren, F. M. Bickelhaupt, *Sci. China Chem*. **2010**, *53*, 210–215.

[21] a) F. M. Bickelhaupt, H. L. Hermann, G. Boche, *Angew. Chem.* **2006**, *118*, 838–841; *Angew. Chem. Int. Ed*. **2006**, *45*, 823–826; b) F. M. Bickelhaupt, M. Solà, C. Fonseca Guerra, *J. Chem. Theory Comput*. **2006**, *2*, 965–980; c) F. M. Bickelhaupt, M. Solà, C. Fonseca Guerra, *Faraday Discuss*. **2007**, *135*, 451–468.

4.6 Appendices

Appendix 4.1. Activation strain analyses (in kcal mol^{-1}) of $D_2Ch{\bullet\bullet\bullet}A^-$ chalcogen bonds at the equilibrium geometries (in Å, deg.).[a]

$D_2Ch{\bullet\bullet\bullet}A^-$	$r_{Ch\bullet\bullet\bullet A}$	r_{D^1-Ch}	r_{D^2-Ch}	Θ_1	Θ_2	Δr_{D^1-Ch}	Δr_{D^2-Ch}	$\Delta\Theta_1$	ΔE	ΔE_{strain}	ΔE_{int}
$F_2O{\bullet\bullet\bullet}F^-$	1.784	1.784	1.374	97.6	97.6	0.408	–0.002	–6.1	–21.9	28.3	–50.2
$F_2O{\bullet\bullet\bullet}Cl^-$	2.183	1.778	1.383	98.8	101.3	0.402	0.007	–4.9	–9.9	28.1	–37.9
$F_2O{\bullet\bullet\bullet}Br^-$	2.113	1.958	1.399	98.6	103.4	0.582	0.023	–5.1	–11.5	45.0	–56.5
$Cl_2O{\bullet\bullet\bullet}F^-$	1.838	2.181	1.649	104.4	99.5	0.500	–0.032	–7.9	–16.0	24.3	–40.3
$Cl_2O{\bullet\bullet\bullet}Cl^-$	2.172	2.172	1.669	105.5	105.5	0.491	–0.012	–6.6	–6.5	24.5	–31.0
$Cl_2O{\bullet\bullet\bullet}Br^-$	1.966	2.559	1.690	105.7	110.8	0.878	0.009	–6.6	–11.0	46.5	–57.5
$Br_2O{\bullet\bullet\bullet}F^-$	2.162	1.971	1.825	106.1	86.6	0.153	0.007	–8.0	–12.9	4.5	–17.4
$Br_2O{\bullet\bullet\bullet}Cl^-$	2.673	1.902	1.839	111.9	94.0	0.084	0.021	–2.2	–6.0	1.5	–7.6
$Br_2O{\bullet\bullet\bullet}Br^-$	2.243	2.243	1.844	108.2	108.2	0.425	0.026	–5.9	–6.2	20.6	–26.7
$F_2S{\bullet\bullet\bullet}F^-$	1.813	1.813	1.631	87.0	87.0	0.227	0.045	–11.2	–50.1	16.2	–66.3
$F_2S{\bullet\bullet\bullet}Cl^-$	2.452	1.735	1.617	89.3	88.2	0.149	0.031	–8.9	–23.1	8.5	–31.7
$F_2S{\bullet\bullet\bullet}Br^-$	2.647	1.721	1.614	90.1	88.7	0.135	0.028	–8.1	–19.8	7.1	–26.9
$Cl_2S{\bullet\bullet\bullet}F^-$	1.748	2.477	2.051	92.1	93.0	0.461	0.035	–11.5	–53.1	24.5	–77.5
$Cl_2S{\bullet\bullet\bullet}Cl^-$	2.339	2.339	2.048	94.4	94.4	0.323	0.032	–9.2	–25.3	14.8	–40.1
$Cl_2S{\bullet\bullet\bullet}Br^-$	2.506	2.338	2.046	94.9	95.1	0.322	0.030	–8.7	–22.4	14.4	–36.9
$Br_2S{\bullet\bullet\bullet}F^-$	1.743	2.667	2.208	92.8	93.9	0.487	0.028	–11.1	–51.7	22.2	–73.9
$Br_2S{\bullet\bullet\bullet}Cl^-$	2.346	2.500	2.207	95.6	95.3	0.320	0.027	–8.3	–24.7	12.2	–36.8
$Br_2S{\bullet\bullet\bullet}Br^-$	2.507	2.507	2.207	96.0	96.0	0.327	0.027	–7.9	–22.3	12.3	–34.6
$F_2Se{\bullet\bullet\bullet}F^-$	1.931	1.931	1.773	87.3	87.3	0.201	0.043	–8.9	–62.4	11.4	–73.7
$F_2Se{\bullet\bullet\bullet}Cl^-$	2.495	1.888	1.765	88.6	89.6	0.158	0.035	–7.7	–34.6	7.7	–42.3
$F_2Se{\bullet\bullet\bullet}Br^-$	2.659	1.884	1.764	88.7	89.9	0.154	0.034	–7.6	–30.7	7.4	–38.0
$Cl_2Se{\bullet\bullet\bullet}F^-$	1.903	2.504	2.200	93.8	92.5	0.349	0.045	–7.3	–63.6	15.1	–78.6
$Cl_2Se{\bullet\bullet\bullet}Cl^-$	2.438	2.438	2.198	95.3	95.3	0.283	0.043	–5.8	–35.7	10.9	–46.6
$Cl_2Se{\bullet\bullet\bullet}Br^-$	2.600	2.438	2.198	96.0	96.0	0.283	0.043	–5.1	–32.1	10.7	–42.8
$Br_2Se{\bullet\bullet\bullet}F^-$	1.902	2.674	2.351	94.7	93.3	0.362	0.039	–7.0	–61.7	13.3	–75.0
$Br_2Se{\bullet\bullet\bullet}Cl^-$	2.440	2.601	2.353	96.4	96.3	0.289	0.041	–5.3	–34.5	9.4	–43.9
$Br_2Se{\bullet\bullet\bullet}Br^-$	2.602	2.602	2.353	97.1	97.1	0.290	0.041	–4.6	–31.2	9.3	–40.5
$F_2Te{\bullet\bullet\bullet}F^-$	2.054	2.054	1.930	84.2	84.2	0.162	0.038	–9.7	–72.4	7.9	–80.3
$F_2Te{\bullet\bullet\bullet}Cl^-$	2.608	2.026	1.927	85.2	86.3	0.134	0.035	–8.7	–42.5	5.9	–48.5
$F_2Te{\bullet\bullet\bullet}Br^-$	2.777	2.022	1.926	85.2	86.6	0.130	0.034	–8.7	–38.1	5.6	–43.7
$Cl_2Te{\bullet\bullet\bullet}F^-$	2.039	2.618	2.380	90.0	88.5	0.285	0.047	–8.2	–73.3	10.8	–84.1
$Cl_2Te{\bullet\bullet\bullet}Cl^-$	2.582	2.582	2.378	91.4	91.4	0.249	0.045	–6.8	–43.0	8.6	–51.6
$Cl_2Te{\bullet\bullet\bullet}Br^-$	2.745	2.579	2.378	91.4	91.8	0.246	0.045	–6.8	–38.6	8.4	–47.1
$Br_2Te{\bullet\bullet\bullet}F^-$	2.040	2.796	2.537	90.8	88.5	0.304	0.045	–8.3	–72.0	9.9	–81.9
$Br_2Te{\bullet\bullet\bullet}Cl^-$	2.582	2.750	2.533	92.5	92.0	0.258	0.041	–6.6	–42.0	7.6	–49.6
$Br_2Te{\bullet\bullet\bullet}Br^-$	2.751	2.751	2.535	92.8	92.8	0.259	0.043	–6.3	–37.7	7.6	–45.3

[a] Computed at ZORA-M06/QZ4P.

Appendix 4.2. Energy decomposition analyses (in kcal mol^{-1}) of $D_2Ch\bullet\bullet\bullet A^-$ chalcogen bonds at the equilibrium geometries.[a]

$D_2Ch\bullet\bullet\bullet A^-$	ΔE_{int}	ΔV_{elstat}	ΔE_{Pauli}	ΔE_{oi}	ε(4a')	⟨4a'|np$_y$⟩	⟨2a'|np$_y$⟩	⟨2a''|np$_x$⟩	Pop$_{4a'}$	Pop$_{npy}$	$\Delta Q_{D_2Ch}^{VDD}$
$F_2O\bullet\bullet\bullet F^-$	–50.2	–55.3	87.5	–82.4	–6.4	0.12	0.13	0.07	0.48	1.61	–0.37
$F_2O\bullet\bullet\bullet Cl^-$	–37.9	–43.4	72.6	–67.1	–6.4	0.13	0.13	0.06	0.54	1.53	–0.35
$F_2O\bullet\bullet\bullet Br^-$	–56.5	–65.3	121.8	–113.0	–7.4	0.14	0.14	0.07	0.79	1.30	–0.48
$Cl_2O\bullet\bullet\bullet F^-$	–40.3	–38.8	79.1	–80.6	–5.7	0.11	0.14	0.04	0.52	1.59	–0.41
$Cl_2O\bullet\bullet\bullet Cl^-$	–31.0	–39.4	80.0	–71.5	–5.7	0.12	0.15	0.04	0.62	1.53	–0.41
$Cl_2O\bullet\bullet\bullet Br^-$	–57.5	–94.2	198.8	–162.1	–6.7	0.13	0.15	0.06	1.08	1.13	–0.62
$Br_2O\bullet\bullet\bullet F^-$	–17.4	–11.5	30.5	–36.4	–3.9	0.09	0.11	0.01	0.28	1.77	–0.26
$Br_2O\bullet\bullet\bullet Cl^-$	–7.6	–7.6	19.9	–19.9	–3.6	0.09	0.09	0.01	0.25	1.88	–0.19
$Br_2O\bullet\bullet\bullet Br^-$	–26.7	–41.5	89.0	–74.3	–5.1	0.13	0.16	0.04	0.68	1.51	–0.44
$F_2S\bullet\bullet\bullet F^-$	–66.3	–126.5	168.3	–108.1	–3.6	0.18	0.16	0.15	0.33	1.71	–0.35
$F_2S\bullet\bullet\bullet Cl^-$	–31.7	–56.8	74.5	–49.3	–3.1	0.22	0.16	0.11	0.31	1.73	–0.21
$F_2S\bullet\bullet\bullet Br^-$	–26.9	–47.2	60.7	–40.4	–2.9	0.22	0.16	0.10	0.29	1.76	–0.19
$Cl_2S\bullet\bullet\bullet F^-$	–77.5	–149.7	222.8	–150.7	–4.7	0.17	0.17	0.14	0.47	1.65	–0.47
$Cl_2S\bullet\bullet\bullet Cl^-$	–40.1	–72.9	109.9	–77.1	–4.1	0.20	0.20	0.10	0.46	1.63	–0.34
$Cl_2S\bullet\bullet\bullet Br^-$	–36.9	–64.2	95.4	–68.1	–4.1	0.20	0.19	0.10	0.47	1.65	–0.34
$Br_2S\bullet\bullet\bullet F^-$	–73.9	–148.4	234.2	–159.7	–4.6	0.16	0.14	0.18	0.52	1.64	–0.51
$Br_2S\bullet\bullet\bullet Cl^-$	–36.8	–69.7	110.9	–78.0	–4.0	0.19	0.20	0.10	0.48	1.64	–0.36
$Br_2S\bullet\bullet\bullet Br^-$	–34.6	–62.2	97.5	–69.8	–4.1	0.19	0.19	0.09	0.49	1.63	–0.36
$F_2Se\bullet\bullet\bullet F^-$	–73.7	–124.6	136.6	–85.7	–3.8	0.18	0.15	0.15	0.27	1.73	–0.32
$F_2Se\bullet\bullet\bullet Cl^-$	–42.3	–69.7	79.4	–52.0	–3.5	0.21	0.15	0.12	0.28	1.76	–0.23
$F_2Se\bullet\bullet\bullet Br^-$	–38.0	–62.1	71.3	–47.2	–3.5	0.22	0.16	0.12	0.29	1.75	–0.22
$Cl_2Se\bullet\bullet\bullet F^-$	–78.6	–132.4	160.1	–106.3	–4.3	0.18	0.16	0.13	0.36	1.69	–0.40
$Cl_2Se\bullet\bullet\bullet Cl^-$	–46.6	–78.2	99.2	–67.7	–4.0	0.22	0.18	0.11	0.38	1.69	–0.31
$Cl_2Se\bullet\bullet\bullet Br^-$	–42.8	–70.0	88.6	–61.5	–4.0	0.22	0.18	0.11	0.40	1.68	–0.32
$Br_2Se\bullet\bullet\bullet F^-$	–75.0	–129.4	166.0	–111.6	–4.2	0.17	0.17	0.13	0.39	1.69	–0.43
$Br_2Se\bullet\bullet\bullet Cl^-$	–43.9	–75.9	101.5	–69.5	–3.9	0.21	0.19	0.11	0.39	1.70	–0.33
$Br_2Se\bullet\bullet\bullet Br^-$	–40.5	–68.1	90.6	–62.9	–3.9	0.22	0.19	0.10	0.42	1.66	–0.34
$F_2Te\bullet\bullet\bullet F^-$	–80.3	–134.6	132.8	–78.6	–3.8	0.19	0.13	0.15	0.21	1.79	–0.32
$F_2Te\bullet\bullet\bullet Cl^-$	–48.5	–80.5	85.1	–53.1	–3.7	0.22	0.15	0.14	0.25	1.78	–0.24
$F_2Te\bullet\bullet\bullet Br^-$	–43.7	–71.7	76.6	–48.6	–3.7	0.23	0.15	0.13	0.26	1.79	–0.24
$Cl_2Te\bullet\bullet\bullet F^-$	–84.1	–140.0	147.9	–92.1	–4.0	0.18	0.16	0.14	0.28	1.77	–0.39
$Cl_2Te\bullet\bullet\bullet Cl^-$	–51.6	–85.8	96.7	–62.5	–3.8	0.24	0.18	0.13	0.32	1.74	–0.30
$Cl_2Te\bullet\bullet\bullet Br^-$	–47.1	–77.8	88.4	–57.6	–3.8	0.24	0.18	0.13	0.33	1.75	–0.30
$Br_2Te\bullet\bullet\bullet F^-$	–81.9	–137.3	151.8	–96.4	–3.9	0.17	0.16	0.14	0.30	1.76	–0.41
$Br_2Te\bullet\bullet\bullet Cl^-$	–49.6	–84.7	99.8	–64.7	–3.7	0.23	0.19	0.13	0.34	1.75	–0.32
$Br_2Te\bullet\bullet\bullet Br^-$	–45.3	–75.7	88.9	–58.6	–3.7	0.24	0.19	0.12	0.35	1.74	–0.32

[a] Computed at ZORA-M06/QZ4P; ε(4a') = 4a' orbital energy of the prepared D_2Ch fragment (in eV); ⟨Φ|np⟩ = overlap between the Φ fragment molecular orbital of the D_2Ch fragment and one of the np orbitals of the halide A^- (see Figure 1 and Figure S1); Pop = Gross population (in electrons) of indicated orbital.

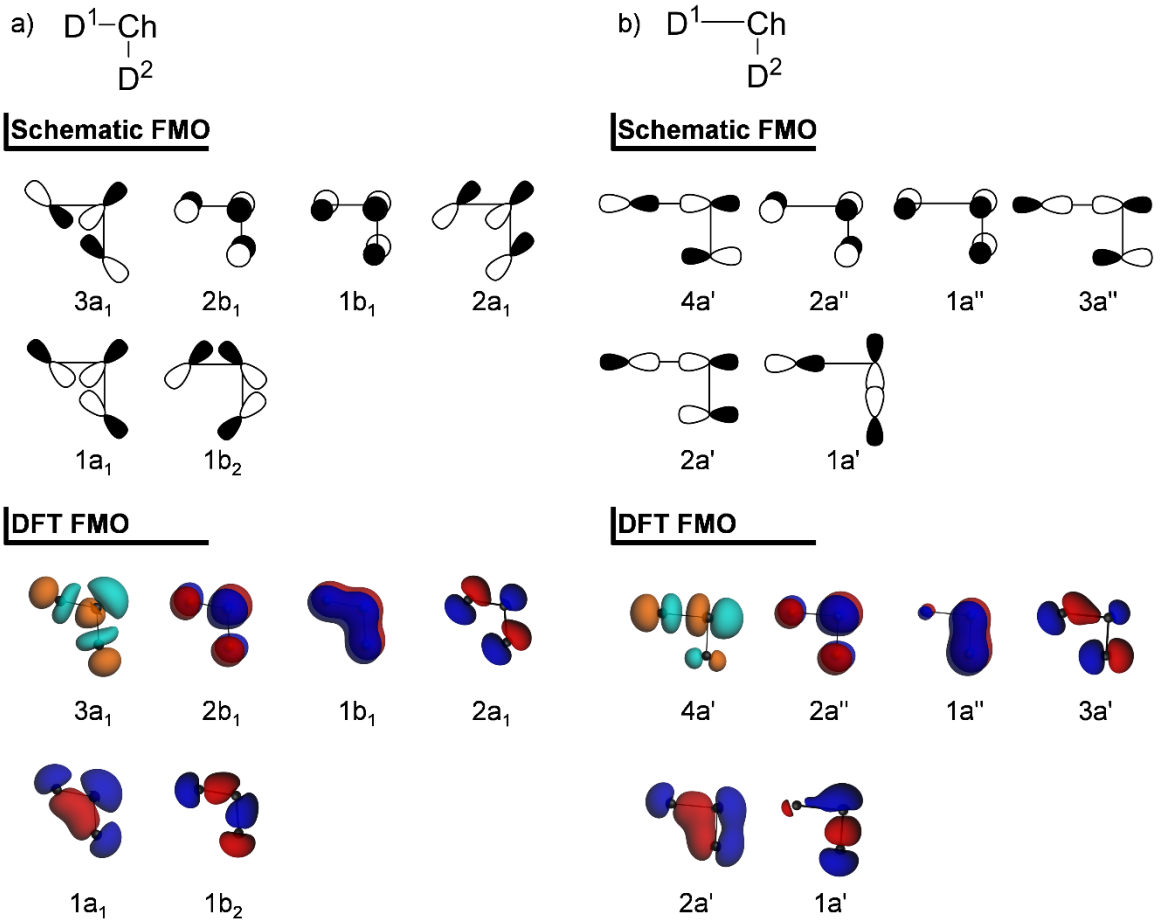

Appendix 4.3. Schematic FMO and DFT MO isosurfaces (at 0.04 a.u.) for the D_2Ch fragment in a) the ground state at C_{2v} symmetry and in b) the geometry of the complex at C_s symmetry, computed at ZORA-M06/QZ4P.

Appendix 4.4. Activation strain and energy decomposition analyses (in kcal mol^{-1}) of $D_mZ\bullet\bullet\bullet A^-$ hydrogen bonds, halogen bonds, and chalcogen bonds at the equilibrium geometries.[a]

$D_mZ\bullet\bullet\bullet A^-$	ΔE	ΔE_{strain}	ΔE_{int}	ΔV_{elstat}	ΔE_{Pauli}	ΔE_{oi}
FH•••F⁻	–45.8	22.1	–67.9	–76.2	72.9	–64.6
FF•••F⁻	–30.5	28.0	–58.5	–44.6	84.3	–98.1
FCl•••F⁻	–52.3	14.0	–66.4	–94.5	124.9	–96.7
FBr•••F⁻	–62.3	10.0	–72.3	–104.0	113.8	–82.0
FI•••F⁻	–70.3	6.9	–77.2	–116.9	115.3	–75.7
F_2O•••F⁻	–21.9	28.3	–50.2	–55.3	87.5	–82.4
F_2S•••F⁻	–50.1	16.2	–66.3	–126.5	168.3	–108.1
F_2Se•••F⁻	–62.4	11.4	–73.7	–124.6	136.6	–85.7
F_2Te•••F⁻	–72.4	7.9	–80.3	–134.6	132.8	–78.6
FH•••F⁻ [b]	–53.0	19.7	–72.8	–76.4	68.8	–65.1
FF•••F⁻ [b]	–51.5	23.5	–75.0	–41.0	73.2	–107.1
FCl•••F⁻ [b]	–64.5	11.9	–76.4	–85.5	107.2	–98.1
FBr•••F⁻ [b]	–70.9	8.6	–79.5	–92.3	98.8	–86.0
FI•••F⁻ [b]	–75.0	6.1	–81.1	–103.5	100.0	–77.7

[a] Computed at ZORA-M06/QZ4P. [b] Computed at ZORA-BP86/TZ2P (from: L. P. Wolters, F. M. Bickelhaupt, *ChemistryOpen* **2012**, *1*, 96–105).

5 | The Pnictogen Bond

Part of this chapter previously appeared as

The Pnictogen Bond: A Quantitative Molecular Orbital Picture
L. de Azevedo Santos, T. C. Ramalho, T. A. Hamlin, F. Matthias Bickelhaupt
Phys. Chem. Chem. Phys. **2021**, *23*, 13842–13852

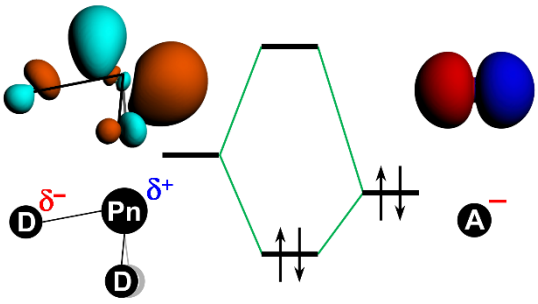

Abstract | We have analyzed the structure and stability of archetypal pnictogen-bonded model complexes D3Pn•••A– (Pn = N, P, As, Sb; D, A = F, Cl, Br) using state-of-the-art relativistic density functional calculations at ZORA-M06/QZ4P. We have accomplished two tasks: (i) to compute accurate trends in pnictogen-bond strength based on a set of consistent data; and (ii) to rationalize these trends in terms of detailed analyses of the bonding mechanism based on quantitative Kohn-Sham molecular orbital (KS-MO) theory in combination with a canonical energy decomposition analyses (EDA) and Voronoi deformation density (VDD) analyses of the charge distribution. We have found that pnictogen bonds have a significant covalent character stemming from strong HOMO–LUMO interactions between the lone pair of A^- and the σ* of D_3Pn. As such, the underlying mechanism of the pnictogen bond is similar to that of hydrogen, halogen, and chalcogen bonds.

Keywords | Activation strain model, Pnictogen bonding, Density functional calculations, Energy decomposition analysis, Noncovalent Interactions

5.1 Introduction

The term pnictogen for the elements of the nitrogen group (group 15) was first proposed by van Arkel in the early 1950s.[1] Its etymology derives from the Ancient Greek root πνιγ ("choke") and is a reference to the Dutch and German names for nitrogen, *stikstof* and *Stickstoff*, respectively, which literally mean "suffocation substance". The trivalent pnictogen atom of a Lewis-acidic pnictogen-bond donor D_3Pn (Pn = group 15 atom) can engage in an intermolecular interaction, coined pnictogen bond, with a Lewis-basic pnictogen-bond acceptor A^-.[2] One of the first indications of Pn bonding appeared from stacked distibines and dibismuthines in crystal structures[3a] and from intramolecular N•••P contact in hypervalent phosphorus compounds.[3b] Later, weak P•••P interaction was identified via through-space coupling by NMR of phosphanyl-*ortho*-carbaboranes.[3c-e] Since then, Pn bonding has flourished and emerged as a tool for coordination chemistry[4] and catalysis.[5] The nature of pnictogen bonds (similar to that of chalcogen and halogen bonds) is in general considered predominantly electrostatic,[6] although the bonding mechanism of weak interactions is still on debate.[2b,7,8]

In this study, we have computationally analyzed a range of pnictogen-bonded $D_3Pn•••A^-$ complexes (Pn = N, P, As, Sb; D, A = F, Cl, Br; see Scheme 5.1), using relativistic density functional theory (DFT) at ZORA-M06/QZ4P. One purpose of our work is to provide a set of consistent structural and energy data from which reliable trends can be inferred for a wide range of model systems. From these data, we have constructed a unified framework to rationalize the nature of pnictogen bonds, chalcogen bonds, halogen bonds, and hydrogen bonds, by studying the associated electronic structure and bonding mechanism.[8]

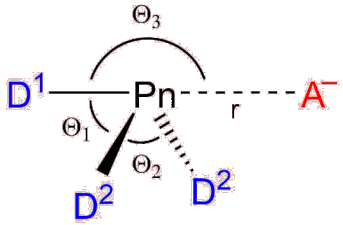

Scheme 5.1. Pnictogen-bonded $D_3Pn•••A^-$ model complexes (Pn = N, P, As, Sb; D, A = F, Cl, Br).

To this end, the pnictogen atom (Pn), the substituent (D), or the pnictogen bond accepting Lewis base (A^-) are systematically varied to assess how the geometries and energies of our model complexes $D_3Pn•••A^-$ are affected. Activation strain analyses[9] are performed on the formation of the pnictogen-bond complexes to understand the origin of the computed trends.

As part of these analyses, the underlying bonding mechanism is elucidated in the context of Kohn-Sham molecular orbital (MO) theory in combination with a matching energy decomposition analysis (EDA) as implemented in the Amsterdam Density Functional (ADF) program.[10,11] Our analyses along the entire reaction profile for each of the pnictogen-bond complexation reactions demonstrate that pnictogen bonds are not at all purely electrostatic phenomena. Instead, they are, to a substantial extent, covalent in nature, very similar to chalcogen bonds, halogen bonds, and hydrogen bonds.

5.2 Theoretical Methods

Computational details

All calculations were carried out using the Amsterdam Density Functional (ADF) 2017.103 program.[11] The equilibrium geometries and energies of pnictogen-bonded complexes were computed at DFT level using the meta-hybrid functional M06.[12] A large uncontracted relativistically optimized QZ4P Slater type orbitals (STOs) basis set containing diffuse functions was used. The QZ4P all-electron basis set.[13] no frozen-core approximation, is of quadruple-ζ quality for all atoms and has been augmented with the following sets of polarization and diffuse functions: two 3*d* and two 4*f* on nitrogen and fluorine, three 3*d* and two 4*f* on phosphorus and chlorine, two 4*d* and three 4*f* on arsenic and bromine, one 5*d* and three 4*f* on antimony and iodine. The molecular density was fitted by the systematically improvable Zlm fitting scheme. The scalar relativistic effects were accounted using the zeroth-order regular approximation (ZORA) Hamiltonian.[14]

Analysis of the bonding mechanism

Insight into the bonding mechanism is obtained through activation strain analyses of the various pnictogen bond formation reactions. These complexation reactions are computationally modeled by decreasing the distance between A^- and the Pn atom of the D_3Pn fragment, allowing the system to geometrically relax at each point. The $D_3Pn{\bullet\bullet\bullet}A^-$ distance is increased, starting from the equilibrium geometry in the pnictogen-bonded complex ($r_{Pn\cdots A}$) to a value of 5.300 Å. Thus, each analysis starts from an optimized $D_3Pn{\bullet\bullet\bullet}A^-$ complex, which is then transformed into the D_3Pn molecule and a halide at a relatively large distance.

These complexation reactions are analyzed using the activation strain model. The activation strain model of chemical reactivity[9] is a fragment-based approach to understand the

energy profile of a chemical process in terms of the original reactants. Thus, the potential energy surface $\Delta E(\zeta)$ is decomposed along the reaction coordinate ζ (or just at one point along ζ) into the strain energy $\Delta E_{\text{strain}}(\zeta)$, which is associated with the geometrical deformation of the individual reactants as the process takes place, plus the actual interaction energy $\Delta E_{\text{int}}(\zeta)$ between the deformed reactants [Eq. (5.1)].

$$\Delta E(\zeta) = \Delta E_{\text{strain}}(\zeta) + \Delta E_{\text{int}}(\zeta) \tag{5.1}$$

In the equilibrium geometry, that is, for $\zeta = \zeta_{\text{eq}}$, this yields an expression for the bond energy $\Delta E(\zeta_{\text{eq}}) = \Delta E_{\text{strain}} + \Delta E_{\text{int}}$. The PyFrag program was used to facilitate the analyses along the reaction coordinate ζ of the bond formation processes.[15] The interaction energy $\Delta E_{\text{int}}(\zeta)$ between the deformed reactants is further analyzed in the conceptual framework provided by the quantitative Kohn-Sham MO model.[10] To this end, it is decomposed in three physically meaningful terms [Eq. (5.2)] using a quantitative energy decomposition analysis (EDA) as implemented in ADF.[10,11]

$$\Delta E_{\text{int}}(\zeta) = \Delta V_{\text{elstat}}(\zeta) + \Delta E_{\text{Pauli}}(\zeta) + \Delta E_{\text{oi}}(\zeta) \tag{5.2}$$

The usually attractive term ΔV_{elstat} corresponds to the classical Coulomb interaction between the unperturbed charge distributions of the deformed reactants and has four components [Eq. (5.3)]: (i) the electrostatic repulsion between the electron densities of fragments 1 and 2, $\Delta V_{\text{elstat},\rho_1\rho_2}$; (ii) the electrostatic attraction between the nucleus of fragment 1 and the electron density of fragment 2, $\Delta V_{\text{elstat},n_1\rho_2}$; (iii) the electrostatic attraction between the electron density of fragment 1 and the nucleus of fragment 2, $\Delta V_{\text{elstat},\rho_1 n_2}$; and (iv) the electrostatic repulsion between the nuclei of fragments 1 and 2, $\Delta V_{\text{elstat},n_1 n_2}$.

$$\Delta V_{\text{elstat}}(\zeta) = \Delta V_{\text{elstat},\rho_1\rho_2}(\zeta) + \Delta V_{\text{elstat},n_1\rho_2}(\zeta) + \Delta V_{\text{elstat},\rho_1 n_2}(\zeta) + \Delta V_{\text{elstat},n_1 n_2}(\zeta) \tag{5.3}$$

The Pauli repulsion energy (ΔE_{Pauli}) comprises the destabilizing interactions between occupied orbitals of one reactant and those of another reactant and is responsible for steric repulsion. The orbital-interaction energy (ΔE_{oi}) accounts for charge transfer, that is, the

interaction between occupied orbitals of one fragment and unoccupied orbitals of the other fragment, including the interactions of the highest occupied and lowest unoccupied MOs (HOMO–LUMO), and polarization, that is, empty–occupied orbital mixing on one fragment, due to the presence of another fragment.

The electron density distribution is analyzed using the Voronoi deformation density (VDD) method for computing atomic charges.[16] The VDD atomic charge on atom X in a molecule (Q_X^{VDD}) is computed as the (numerical) integral of the deformation density in the volume of the Voronoi cell of atom X [Eq. (5.4)]. The Voronoi cell of atom X is defined as the compartment of space bounded by the bond midplanes on and perpendicular to all bond axes between nucleus X and its neighboring nuclei.

$$Q_X^{VDD} = -\int_{\text{Voronoi cell of X}} \left[\rho(r) - \rho_{\text{promolecule}}(r)\right] dr \tag{5.4}$$

Here, the deformation density is the difference between $\rho(r)$, *i.e.*, the electron density of the overall molecule or complex, and $\rho_{\text{promolecule}}(r) = \Sigma_Y \rho_Y(r)$, *i.e.*, the superposition of spherical average-of-configuration atomic densities $\rho_Y(r)$ of each atom Y in the fictitious promolecule without chemical interactions, in which all atoms are considered neutral. The interpretation of the VDD charge Q_{Pn}^{VDD} is rather straightforward and transparent: instead of measuring the amount of charge associated with a particular atom Pn, Q_{Pn}^{VDD} directly monitors how much charge flows out of ($Q_{Pn}^{VDD} > 0$) or into ($Q_{Pn}^{VDD} < 0$) the Voronoi cell of atom Pn due to chemical interactions.

The VDD scheme can also be used to directly compute how much charge flows into or out of an atomic Voronoi cell X in an overall complex (*e.g.*, $[D_3Pn{\bullet\bullet\bullet}A]^-$) relative to two (poly)atomic molecular fragments (*e.g.*, D_3Pn and A^-), instead of spherical atoms, as shown in Eq. (5.5).

$$\Delta Q_X^{VDD} = -\int_{\text{Voronoi cell of X in complex}} \left[\rho_{\text{complex}}(r) - \rho_{\text{fragment 1}}(r) - \rho_{\text{fragment 2}}(r)\right] dr \tag{5.5}$$

ΔQ_X^{VDD} is a measure of how the atomic charge of atom X changes due to the bonding between the fragments. In this work, Eq. (5.5) is used to compute the flow of electrons from the halide A^- to the pnictogen-bond donating molecule D_3Pn (see $\Delta Q_{D_3Pn}^{VDD}$ in Table 5.1).

5.3 Results and Discussion

Pnictogen bond strength and structure

Table 5.1 summarizes the results of our ZORA-M06/QZ4P calculations for a representative selection of nitrogen-, phosphorus-, and antimony-bonded model complexes $D_3Pn{\bullet\bullet\bullet}A^-$, covering D, A = F, Cl, and Br (for the complete dataset see Appendices 5.1 and 5.2). These model reactions go with a single-well potential energy surfaces (PES), that is, there is no energy barrier separating the reactants from their resulting product. In the cases where D ≠ A, C_S symmetric complexes with D^1–Pn bond lengths different from the $Pn{\bullet\bullet\bullet}A^-$ bond and with bond angles $\Theta_1 \neq \Theta_2$ are formed. For the cases where D = A, C_{2v} symmetric complexes with equal bond distances $r_{D^1\text{–}Pn} = r_{Pn\cdots A}$ are formed (see Table 5.1).

The pnictogen bonds $D_3Pn{\bullet\bullet\bullet}A^-$ become stronger and longer upon descending group 15 in the periodic table, going from N to Sb. The pnictogen bonds become weaker and longer as the accepting halide (A^-) goes down group 17, from F^- to Br^-. The elongation of the bonds descending the periodic table originates from the increase in effective size of the atoms involved. In the case of the antimony-bonded complexes $Br_3Sb{\bullet\bullet\bullet}A^-$, for example, ΔE weakens from a value of –78 kcal mol^{-1} for $A^- = F^-$ to –38 kcal mol^{-1} for $A^- = Br^-$ (see Table 5.1). The associated $Sb{\bullet\bullet\bullet}A^-$ bond elongates from around 2.0 Å for $A^- = F^-$ to around 2.8 Å for $A^- = Br^-$. From $A^- = F^-$ to Br^-, the nitrogen bond in $Br_3N{\bullet\bullet\bullet}A^-$ weakens from a value of –30 kcal mol^{-1} to –7 kcal mol^{-1}. The associated $N{\bullet\bullet\bullet}A^-$ bond elongates from a value of around 1.4 Å for $A^- = F^-$ to around 2.3 Å for $A^- = Br^-$. The reason behind the trends in stability will be discussed later.

The strength of the heavier pnictogen bonds $D_3Pn{\bullet\bullet\bullet}A^-$ are minimally affected upon variation of the substituent D. For example, along the series from $F_3Sb{\bullet\bullet\bullet}F^-$ to $Br_3Sb{\bullet\bullet\bullet}F^-$, the bond strength varies only from –72.0 to –77.7 kcal mol^{-1}, the antimony bond distance $r_{Pn\cdots A}$ decreases slightly from 2.037 to 2.014 Å, and the stretch $\Delta r_{D^1\text{–}Pn}$ upon bond formation increases from 0.144 to 0.332 Å. The nitrogen bonds $D_3N{\bullet\bullet\bullet}A^-$ behave differently and become significantly stronger and shorter as D is varied from F to Br (see Table 5.1). For example, along the series from $F_3N{\bullet\bullet\bullet}F^-$ to $Br_3N{\bullet\bullet\bullet}F^-$, the nitrogen bond strengthens from a ΔE value of –11.8 to –30.2 kcal mol^{-1}, the nitrogen bond distance $r_{Pn\cdots A}$ decreases in value from 1.859 to

1.411 Å, and the stretch Δr_{D^1-Pn} significantly increases from 0.503 to 1.417 Å. A comprehensive analysis of the origin of these trends is provided in the following.

Table 5.1. Activation strain analyses (in kcal mol^{-1}) of a representative set of $D_3Pn{\bullet\bullet\bullet}A^-$ at the equilibrium geometries (in Å, deg.).[a]

$D_3Pn{\bullet\bullet\bullet}A^-$	ΔE	ΔE_{strain}	ΔE_{int}	$\Delta Q_{D_3Pn}^{VDD}$	$r_{Pn\cdots A}$	Δr_{D^1-Pn}	Δr_{D^2-Pn}	Θ_3	$\Delta\Theta_1$
$F_3N{\bullet\bullet\bullet}F^-$	–11.8	32.5	–44.3	–0.30	1.859	0.503	–0.017	170.3	–8.9
$F_3N{\bullet\bullet\bullet}Cl^-$	–3.5	0.8	–4.3	–0.01	3.239	0.048	–0.009	168.3	–1.5
$F_3N{\bullet\bullet\bullet}Br^-$	–2.9	0.5	–3.5	0.00	3.484	0.040	–0.008	166.8	–1.2
$Cl_3N{\bullet\bullet\bullet}F^-$	–30.4	55.7	–86.1	–0.65	1.416	1.490	0.001	170.7	–25.7
$Cl_3N{\bullet\bullet\bullet}Cl^-$	–5.6	22.9	–28.5	–0.36	2.328	0.575	0.004	146.6	–7.8
$Cl_3N{\bullet\bullet\bullet}Br^-$	–6.2	3.5	–9.7	–0.18	2.920	0.149	0.024	145.6	–2.8
$Br_3N{\bullet\bullet\bullet}F^-$	–30.2	53.2	–83.3	–0.67	1.411	1.417	0.022	165.7	–24.0
$Br_3N{\bullet\bullet\bullet}Cl^-$	–8.0	2.0	–10.0	–0.18	2.813	0.111	0.026	149.4	–2.8
$Br_3N{\bullet\bullet\bullet}Br^-$	–7.0	17.2	–24.2	–0.44	2.322	0.416	0.066	127.2	–3.1
$F_3P{\bullet\bullet\bullet}F^-$	–48.9	17.4	–66.4	–0.35	1.753	0.189	0.044	189.4	–10.6
$F_3P{\bullet\bullet\bullet}Cl^-$	–16.0	4.4	–20.4	–0.12	2.700	0.083	0.016	183.4	–5.6
$F_3P{\bullet\bullet\bullet}Br^-$	–12.9	3.0	–15.9	–0.09	2.982	0.067	0.012	181.6	–4.6
$Cl_3P{\bullet\bullet\bullet}F^-$	–67.4	31.8	–99.3	–0.52	1.649	0.572	0.048	181.4	–11.8
$Cl_3P{\bullet\bullet\bullet}Cl^-$	–25.5	14.4	–39.8	–0.31	2.370	0.315	0.034	174.6	–8.7
$Cl_3P{\bullet\bullet\bullet}Br^-$	–20.5	10.7	–31.3	–0.26	2.617	0.263	0.030	172.9	–7.6
$Br_3P{\bullet\bullet\bullet}F^-$	–71.0	30.2	–101.2	–0.56	1.637	0.647	0.045	175.4	–11.3
$Br_3P{\bullet\bullet\bullet}Cl^-$	–28.5	15.4	–43.9	–0.37	2.312	0.382	0.038	172.0	–8.9
$Br_3P{\bullet\bullet\bullet}Br^-$	–23.4	11.9	–35.3	–0.32	2.550	0.323	0.034	170.6	–7.9
$F_3Sb{\bullet\bullet\bullet}F^-$	–72.0	8.8	–80.8	–0.31	2.037	0.144	0.037	193.9	–8.9
$F_3Sb{\bullet\bullet\bullet}Cl^-$	–38.9	5.8	–44.7	–0.21	2.643	0.112	0.030	188.3	–7.3
$F_3Sb{\bullet\bullet\bullet}Br^-$	–33.6	5.0	–38.7	–0.19	2.840	0.103	0.028	186.7	–6.8
$Cl_3Sb{\bullet\bullet\bullet}F^-$	–77.1	12.3	–89.4	–0.38	2.017	0.301	0.051	183.7	–7.6
$Cl_3Sb{\bullet\bullet\bullet}Cl^-$	–42.7	8.9	–51.7	–0.28	2.592	0.244	0.045	178.4	–6.5
$Cl_3Sb{\bullet\bullet\bullet}Br^-$	–37.3	8.0	–45.3	–0.27	2.780	0.229	0.043	177.0	–6.1
$Br_3Sb{\bullet\bullet\bullet}F^-$	–77.7	11.5	–89.2	–0.41	2.014	0.332	0.049	181.2	–7.2
$Br_3Sb{\bullet\bullet\bullet}Cl^-$	–43.5	8.5	–52.0	–0.31	2.580	0.272	0.046	175.6	–6.1
$Br_3Sb{\bullet\bullet\bullet}Br^-$	–38.1	7.7	–45.8	–0.30	2.766	0.256	0.045	174.2	–5.8

[a] Computed at ZORA-M06/QZ4P. For full set of data, see Appendices 5.1 and 5.2.

Bond analyses with variation of Pn

The pnictogen bond $D_3Pn{\bullet\bullet\bullet}A^-$ strength ΔE increases as Pn varies along N, P, As, and Sb, when the donating atom (D) and the accepting halide (A^-) remains unchanged and the trend in ΔE is mainly set by the interaction energy ΔE_{int}. For example, from $F_3N{\bullet\bullet\bullet}F^-$ to $F_3Sb{\bullet\bullet\bullet}F^-$, ΔE is strengthened from a value of –11.8 to –72.0 kcal mol^{-1} and ΔE_{int} is strengthened from a value of –44.3 to –80.8 kcal mol^{-1} (see Table 5.1). The trend in ΔE is reinforced by the strain energy (ΔE_{strain}), which becomes less destabilizing from 32.5 to 8.8 kcal mol^{-1} along the same series. We extend our analysis to the entire reaction coordinate ζ, projected onto the stretch in D^1–Pn bond, $\Delta r_{D^1–Pn}$, that occurs as the pnictogen-bond accepting A^- atom approaches the D_3Pn molecule (see Theoretical Methods section). The activation strain and energy decomposition diagrams (ASD and EDD) for a representative example series, namely $F_3N{\bullet\bullet\bullet}F^-$ to $F_3Sb{\bullet\bullet\bullet}F^-$, are given in Fig. 5.1 (for the complete dataset, see Appendices 5.1 and 5.2). Notably, the trend in bond energy $\Delta E(\zeta)$ is in fact determined by $\Delta E_{int}(\zeta)$, which strengthens when going from Pn = N to Sb (Fig. 5.1, left), whereas the $\Delta E_{strain}(\zeta)$ curves are relatively similar. In fact, only in the equilibrium geometries, the strain term $\Delta E_{strain}(\zeta_{eq})$ become less destabilizing from Pn = N to Sb. The reason is that as the interaction curve becomes steeper along the series, it pulls the equilibrium geometry [which results from the balance between $\Delta E_{strain}(\zeta)$ and $\Delta E_{int}(\zeta)$] to an earlier stage along the reaction coordinate, at which the system is less distorted (*i.e.,* less expanded F^1–Pn bond in the F_3Pn fragment) and thus less strained, as reflected by $\Delta E_{strain}(\zeta_{eq})$ (see Table 5.1).

To understand the trends in $\Delta E_{int}(\zeta)$, we further decomposed the ΔE_{int} into the individual energy components (Fig. 5.1, right). The strengthening of $\Delta E_{int}(\zeta)$ and, consequently, the increasing stabilization of $D_3Pn{\bullet\bullet\bullet}A^-$ as Pn varies along N, P, As, and Sb, is caused by the rising electronegativity difference across the D–Pn bonds as Pn descends in the periodic table. Firstly, this causes the Pn atom to become increasingly positive along N, P, As, and Sb (see VDD atomic charges in Table 5.2), resulting in the $\Delta V_{elstat}(\zeta)$ curves to be the least stabilizing for Pn = N and the most stabilizing for Pn = Sb. For example, the VDD atomic charge on Pn in F_3N, F_3P, F_3As, and F_3Sb amounts to +0.21, +0.33, +0.51, and +0.57 a.u., respectively. Secondly, this causes, among other effects that will be explained later, the σ* D–Pn antibonding 5a' acceptor orbital to have higher amplitude on Pn (see Fig. 5.2), resulting in stronger HOMO–LUMO overlap and thus more stabilizing orbital interactions. These features are also observed for chalcogen bonds $D_2Ch{\bullet\bullet\bullet}A^-$, halogen bonds $DX{\bullet\bullet\bullet}A^-$, and hydrogen bonds $DH{\bullet\bullet\bullet}A^-$, which makes them similar to the pnictogen bonds.[8]

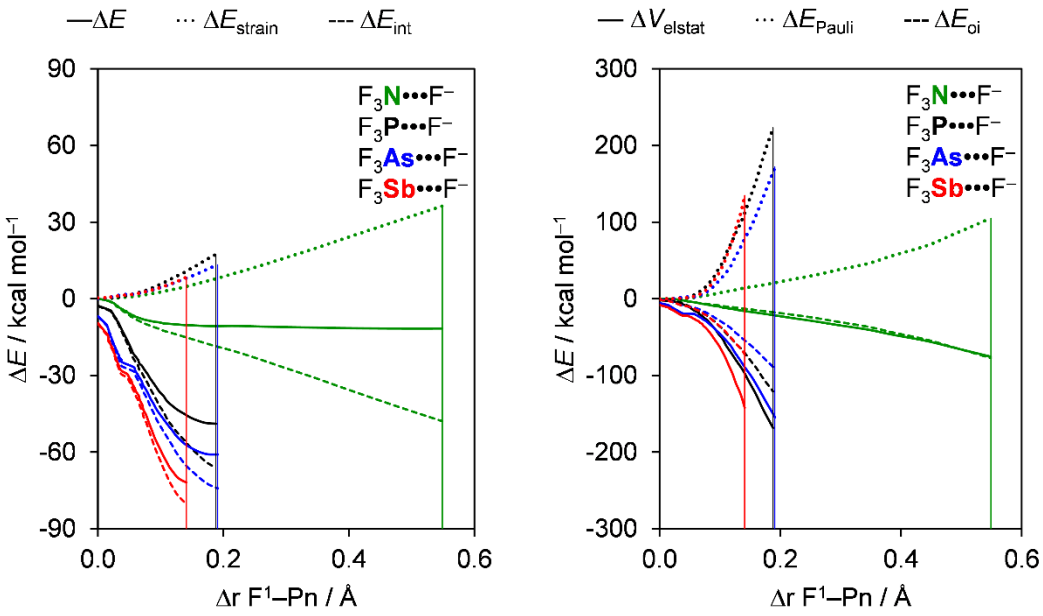

Fig. 5.1. Activation strain (left panel) and energy decomposition (right panel) analyses of $F_3Pn{\bullet\bullet\bullet}F^-$ pnictogen-bonded complexes (green, Pn = N; black, Pn = P; blue, Pn = As; red, Pn = Sb). The vertical lines indicate the position of the stationary points.

Table 5.2. Bonds lengths (in Å), bond angle (in deg.), VDD charge (in a.u.), orbital energies (in eV) and the homolytic bond dissociation energy without ZPE (in kcal mol^{-1}) of isolated D_3Pn fragments.[a]

D_3Pn	r_{D^1-Pn}	r_{D^2-Pn}	Θ_1	Θ_2	Q_{Pn}^{VDD}	$\varepsilon(1e_1)$	$\varepsilon(2a_1)$	$\varepsilon(3a_1)$	$\varepsilon(4e_1)$	BDE_{D-Pn}[b]
F_3N	1.356	1.356	101.9	101.9	0.21	–18.2	–16.8	–10.3	0.6	59.4
Cl_3N	1.753	1.753	107.7	107.7	0.01	–14.4	–13.0	–8.2	–1.3	35.6
Br_3N	1.906	1.906	108.5	108.5	–0.09	–13.1	–11.8	–7.6	–1.4	30.2
F_3P	1.564	1.564	97.5	97.5	0.33	–16.1	–15.1	–9.3	–0.5	133.6
Cl_3P	2.055	2.055	100.4	100.4	0.32	–12.8	–11.7	–8.3	–1.4	79.0
Br_3P	2.227	2.227	100.9	100.9	0.25	–11.8	–10.8	–7.9	–1.7	60.8
F_3As	1.717	1.717	95.8	95.8	0.51	–14.7	–13.8	–10.1	–1.3	116.4
Cl_3As	2.179	2.179	99.1	99.1	0.44	–12.2	–11.2	–8.7	–1.7	76.4
Br_3As	2.342	2.342	99.7	99.7	0.37	–11.3	–10.4	–8.1	–1.9	59.7
F_3Sb	1.893	1.893	94.3	94.3	0.57	–13.5	–12.8	–9.7	–1.9	117.9
Cl_3Sb	2.348	2.348	97.0	97.0	0.55	–11.5	–10.6	–8.5	–2.1	82.8
Br_3Sb	2.510	2.510	97.7	97.7	0.49	–10.7	–9.9	–8.0	–2.2	66.2

[a] Computed at ZORA-M06/QZ4P; [b] Energy for the reaction $D_3Pn \rightarrow D_2Pn^{\bullet} + D^{\bullet}$.

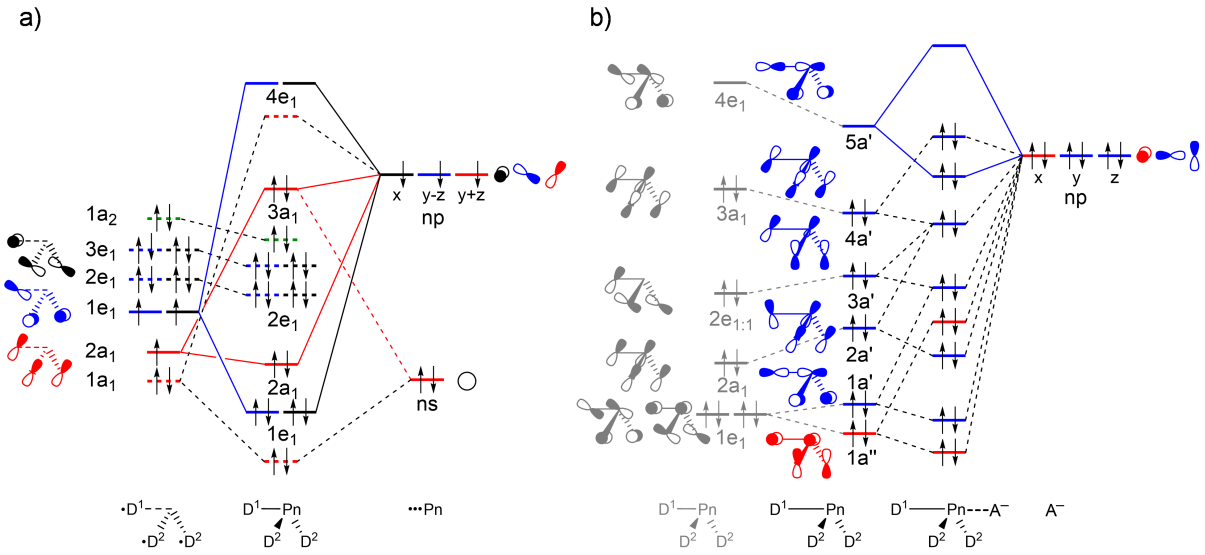

Fig. 5.2. Schematic molecular orbital diagram for (a) isolated D_3Pn fragments at C_{3v} symmetry (red: a_1; green: a_2; blue: $e_{1:1}$; black: $e_{1:2}$) and (b) $D_3Pn{\bullet\bullet\bullet}A^-$ complexes. The first column in (b) refers to the isolated D_3Pn fragment and the second column refers to the D_3Pn fragment deformed to its C_s symmetric geometry in the complex (blue: a'; red: a''), in which one D–Pn bond has been elongated. See Appendix 5.3 for computed 3D isosurfaces of the orbitals.

Our analyses reveal that the pnictogen bonding mechanism is not purely electrostatic but, instead, has a relatively large covalent component (ΔE_{oi}), stemming mainly from the HOMO–LUMO interaction between the occupied halide np_y atomic orbital (AO) and the σ* D–Pn antibonding 5a' acceptor orbital (see Fig. 5.2). For the pnictogen-bonded complexes, the orbital-interaction term ranges from 34% for $F_3Sb{\bullet\bullet\bullet}F^-$ to as much as 65% for $Br_3N{\bullet\bullet\bullet}Cl^-$ of the total bonding interactions ($\Delta E_{oi} + \Delta V_{elstat}$; see Appendix 5.2), and the orbital interaction curves $\Delta E_{oi}(\zeta)$ become more stabilizing from Pn = N to Sb (Fig. 5.1, right). The stronger orbital interaction for the heavier pnictogens is the result of the larger LUMO–HOMO overlap (*i.e.* $\langle 5a' \mid np_y \rangle$; see Fig. 5.2 for the MO diagram that depicts the np_y orbital of A^- oriented towards the D^1–Pn bond of the D_3Pn fragment) as Pn becomes more electropositive. For example, in the $Cl_3Pn{\bullet\bullet\bullet}Cl^-$ series, $\langle 5a' \mid np_y \rangle$ increases from 0.11 to 0.20 to 0.21 to 0.22 along Pn = N, P, As, and Sb in the equilibrium geometry (see Appendix 5.2). The associated charge transfer from A^- to D_3Pn is reflected by the VDD charge of the D_3Pn fragment in the complex, $\Delta Q_{D_3Pn}{}^{VDD}$, which is negative (see Table 5.1). Thus, D_3Pn gains charge from A^- upon complexation, for all $D_3Pn{\bullet\bullet\bullet}A^-$ complexes. For example, $\Delta Q_{D_3Pn}{}^{VDD}$ is –0.30 a.u. for $F_3N{\bullet\bullet\bullet}F^-$ and –0.31 a.u. for $F_3Sb{\bullet\bullet\bullet}F^-$. The HOMO–LUMO charge transfer nature of the pnictogen bond is also reflected by the 3D plots of the deformation densities associated with pnictogen-bond formation in $F_3P{\bullet\bullet\bullet}F^-$ and $F_3Sb{\bullet\bullet\bullet}F^-$ (see Fig. 5.3). Note the charge depletion in the region of the HOMO on

the Lewis base F^- (and in between the Pn•••F^- bond due to the Pauli repulsion[10a]) and the charge accumulation in the region of the LUMO on D_3Pn.

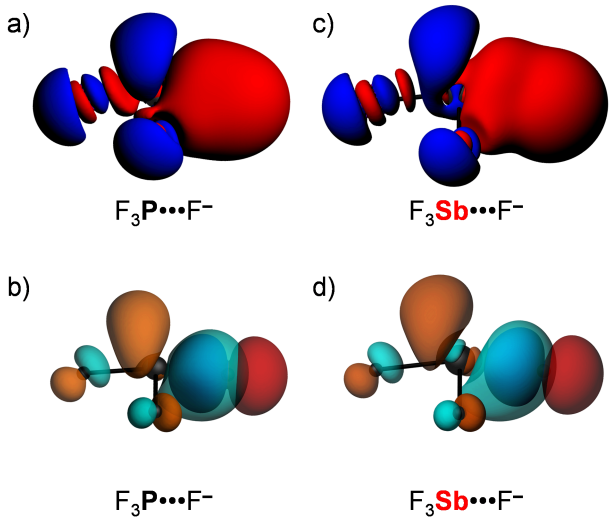

Fig. 5.3. Deformation density ($\Delta\rho(r) = \rho_{[D_3Pn\cdots A^-]}(r) - \rho_{D_3Pn}(r) - \rho_{A^-}(r)$; red = depletion; blue = accumulation) plot (a and c) and HOMO–LUMO interaction (b and d) for a representative series of $D_3Pn•••A^-$ pnictogen bonds.

The $\Delta E_{oi}(\zeta)$ curves become more stabilizing if one goes from nitrogen to the heavier pnictogen bonds but, interestingly, the orbital interaction $\Delta E_{oi}(\zeta_{eq})$ at the stationary point of the complex turns out to be comparable in magnitude for all pnictogens (see Appendix 5.2). The reason is the significantly more pronounced stretch in the F^1–Pn bond for Pn = N than for the heavier pnictogens. This phenomenon causes $\Delta E_{oi}(\zeta_{eq})$ for nitrogen to occur at a later point at which the intrinsically less stabilizing $\Delta E_{oi}(\zeta)$ curve has achieved a more stabilizing value that, as mentioned above, is comparabel to the value of the other pnictigen bonds that do not feature this strong F^1–Pn bond stretch.

The reason that the F^1–Pn streches more for Pn = N than for the heavier pnictogens is its lower polarity and thus weaker bond strength (see Table 5.2) which translates into less strain when it streches upon complexation with the lewis base (see Fig. 5.1). Thus, as the F^1–Pn bond in the $F_3Pn•••F^-$ complexes expands most, the σ* D–Pn antibonding 5a' acceptor orbital drops significantly in energy and, due to a smaller HOMO–LUMO gap, enters into a more stabilizing donor–acceptor orbital interaction $\Delta E_{oi}(\zeta_{eq})$ (see Fig 5.2b). This effect can be observed in Fig. 4a, which shows the energies of the σ* F–Pn antibonding 5a' acceptor orbitals, as well as the VDD atomic charge on Pn in the F_3Pn fragments, along the reaction coordinate. The F^1–Pn bond in the $F_3Pn•••F^-$ complexes expands less from Pn = N to Sb and leads to a smaller

stabilization of the σ* D–Pn antibonding 5a' acceptor orbital and the decrease in HOMO–LUMO gap becomes smaller from Pn = N to Sb, resulting in less stabilization by orbital interactions. For example, for Pn = Sb, the energy of the σ* F–Sb antibonding 5a' acceptor orbital is up to –3.0 eV in F_3Sb at the equilibrium geometry of the $F_3Sb{\bullet\bullet\bullet}F^-$ complex. Due to the weaker F–N bond compared to the F–Sb (*e.g.* BDE_{F-N} = 59.4 kcal mol^{-1} and BDE_{F-Sb} = 117.9 kcal mol^{-1}; see Table 5.2), the F^1–N bond expands to higher extent and the σ* F–N antibonding 5a' acceptor orbital quickly drops to a value of –5.1 eV.

Nevertheless, the nitrogen-bonded complexes remain the weakest as the high stabilization of the σ* F–N antibonding 5a' acceptor orbital is counteracted by its poor orbital overlap with the np_y donor orbital due to the absence of radial nodes in and, thus, the very compact nature of, the nitrogen 2p valence AOs (see Appendix 5.2).

In addition, note that, as the F^1–Pn bond in the $F_3Pn{\bullet\bullet\bullet}F^-$ complexes expands, the pnictogen atom in the D_3Pn fragment becomes more positive (Fig. 5.4a), resulting in a more stabilizing electrostatic $\Delta V_{elstat}(\zeta_{eq})$ (see Appendix 5.2). However, the significant expansion of the F^1–N bond is not enough to make the highly electronegative N atom as positive as the heavier pnictogens, making the nitrogen-bonded complexes to be also the least stabilized by electrostatic attraction.

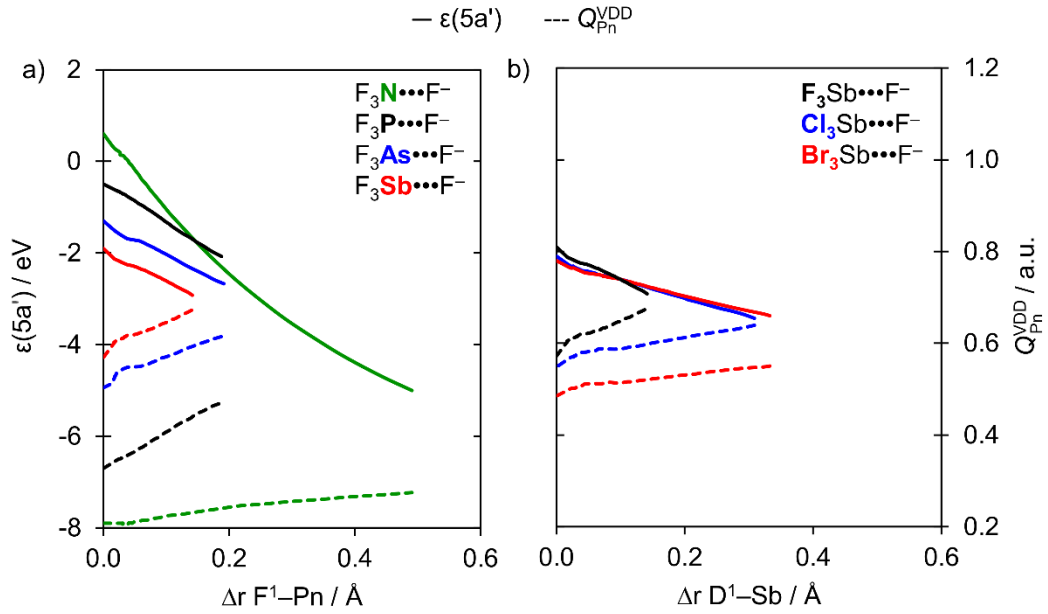

Fig. 5.4. Energy of the 5a' orbital (in eV) and the VDD charge on Pn atom (in a.u.) in the neutral fragment D_3Pn projected onto (a) the F^1–Pn bond stretch (green, Pn = N; black, Pn = P; blue, Pn = As; red, Pn = Sb) and (b) the D^1–Sb bond stretch (black, D = F; blue, D = Cl; red, D = Br).

Bond analyses with variation of A^-

Our analyses show that the pnictogen bonds $D_3Pn{\bullet\bullet\bullet}A^-$ become weaker as the Lewis basicity of the A^- halide decreases from F^- to Br^-.[17] Again, this is equivalent to what was found for chalcogen bonds $D_2Ch{\bullet\bullet\bullet}A^-$, halogen bonds $DX{\bullet\bullet\bullet}A^-$, and hydrogen bonds $DH\cdots A^-$.[8] As aforementioned, pnictogen bonds have both an electrostatic component (ΔV_{elstat}) and a covalent component (ΔE_{oi}) stemming mainly from the HOMO–LUMO interaction between the occupied halide np atomic orbital (AO) and the σ* D–Pn antibonding 5a' acceptor orbital, shown schematically in Fig. 5.2. The electron-donating capacity of the halides is reduced as the halide np AOs become more diffuse and lower in energy from $A^- = F^-$ to Br^-, thus, weakening ΔE_{oi}.[8,17b] This will also result in longer bonds and weaker electrostatic attraction. As a result, the interaction energy (ΔE_{int}) and, thus, the net pnictogen-bond strength ΔE becomes less stabilizing along $A^- = F^-$ to Br^- (see Table 5.1 and Appendix 5.1).

Activation strain analyses reveal that the trend $A^- = F^-$ to Br^- in the total energies $\Delta E(\zeta)$ is directly determined by the trend in the corresponding interaction energies, that is, $\Delta E_{int}(\zeta)$ weakens from $A^- = F^-$ to Br^-. This is nicely seen at the left diagrams in Fig. 5.5, that shows the formation of the pnictogen bonds $D_3Pn{\bullet\bullet\bullet}A^-$, with $A^- = F^-$, Cl^-, and Br^-, for a presentative series of F_3N and F_3Sb molecules. Note that the ΔE_{strain} curves coincide (because they stem from the same molecule with the same F–N bond being stretched as the complexation reaction progresses) and, thus, do not affect the trends in $\Delta E(\zeta)$. For the nitrogen bonds involving the Lewis bases $A^- = Cl^-$ and Br^-, the bond strength is particularly weak because the interaction is too weak to significantly stretch the D^1–N bonds. Consequently, the D_3N fragment achieves a much weaker the electron-accepting capacity in this less distorted equilibrium geometry and so the eventual interaction and bond energy becomes relatively weak (see Fig. 5.5a).

The trend in $\Delta E_{int}(\zeta)$ is again dictated by the bonding components ΔV_{elstat} and ΔE_{oi}. This can be seen in the right panel of Fig. 5.5 which shows that both $\Delta V_{elstat}(\zeta)$ and $\Delta E_{oi}(\zeta)$ become more stabilizing from $A^- = F^-$ to Br^-. The key to understand these trends is of course related to the factors that enhance the strength of the bonding components and, thus, ΔE_{int}. Firstly, an approaching halide A^- with higher lying HOMO and, secondly, a weak D–Pn bond that is easily stretched resulting in a σ* D–Pn antibonding 5a' acceptor orbital that quickly drops in energy as the D^1–Pn bond elongates (see Fig. 5.4). These factors are the driving force for D^1–Pn stretching in $D_3Pn{\bullet\bullet\bullet}A^-$ since they generate stronger orbital interactions and, therefore, stronger pnictogen bonds. For $F_3N\cdots A^-$, the 5a' acceptor orbital energy in the equilibrium geometry of the complex adopts significantly lower values for weaker Lewis bases ($A^- = Cl^-$ or Br^-) than

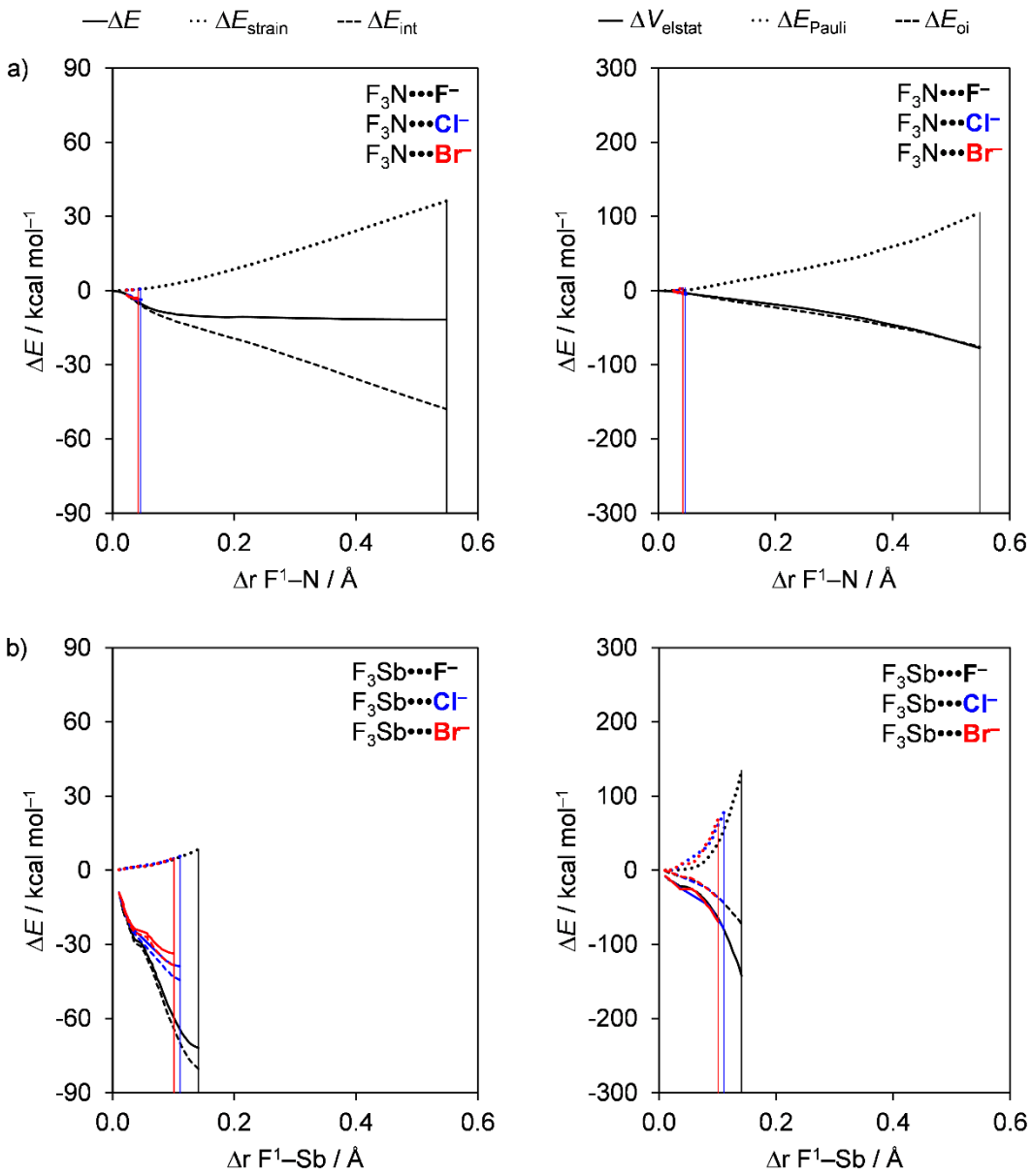

Fig. 5.5. Activation strain (left panel) and energy decomposition (right panel) analyses of (a) $F_3N{\bullet\bullet\bullet}A^-$ and (b) $F_3Sb{\bullet\bullet\bullet}A^-$ (black, $A^- = F^-$; blue, $A^- = Cl^-$; red, $A^- = Br^-$). The vertical lines indicate the position of the stationary points.

for $A^- = F^-$ (*i.e.*, –5.1 eV for $A^- = F^-$, –0.2 eV for $A^- = Cl^-$, and –0.1 eV for $A^- = Br^-$; see Appendix 5.2). Indeed, D^1–Pn stretching is most pronounced if this bond in the neutral fragment is weaker (*e.g.*, ca. 59 kcal mol^{-1} for F–N, ca. 35 kcal mol^{-1} for Cl–N, and ca. 30 kcal mol^{-1} for Br–N; see Table 5.2). For example, the D^1–N stretching in nitrogen-bonded complexes is longer in $Br_3N{\bullet\bullet\bullet}F^-$, which $\Delta r_{D^1\text{–Pn}}$ is 1.4 Å, and less pronounced in $F_3N{\bullet\bullet\bullet}F^-$, which $\Delta r_{D^1\text{–Pn}}$ is 0.5 Å (see Table 5.1). As result, the bonding components, ΔV_{elstat} and ΔE_{oi}, become significantly stronger, up to –300 kcal mol^{-1}, in the $Cl_3N{\bullet\bullet\bullet}A^-$ and the $Br_3N{\bullet\bullet\bullet}A^-$ series. However, the

bonding components are significantly weakened to ca. –60 kcal mol^{-1} for weaker Lewis bases, in which cases $\Delta r_{D^1–Pn}$ varies between only 0.04 and 0.6 Å (see Table 5.1).

Bond analyses with variation of D

The strength of the heavier $D_3Pn•••A^-$ pnictogen bonds (Pn = P, As, Sb) slightly strengthens when the substituent D varies from F to Br. Based on the purely electrostatic picture of the σ-hole model, one might expect just the opposite, that is, a weakening of the pnictogen bond in $D_3Pn•••A^-$ as D varies from F to Br due to a decrease in the positive molecular electrostatic potential of the σ-hole at the Pn atom in the D_3Pn fragment ($V_{S,max}$).[6a,18] This apparent discrepeny from the σ-hole model is traced to the trend that D–Pn bonds become weaker along F–Pn, Cl–Pn and Br–Pn (see Table 5.2). And the weaker the D–Pn bonds, the more they elongate in the eventual equilibrium geometry of the corresponding $D_3Pn•••A^-$ complex. Therefore, the latter is reached at a later stage along the reaction coordinate $\Delta r_{D^1–Pn}$. A consequence of this D–Pn bond elongation is a more electropositive Pn atom and a lower energy of the σ* D–Pn antibonding 5a' acceptor orbital due to a reduction in antibonding character (see Fig. 5.4b). This situation translates into more stabilizing $\Delta V_{elstat}(\zeta)$ and $\Delta E_{oi}(\zeta)$ curves as D varies from F to Cl to Br (see Fig. 5.6, right). For the $D_3N•••A^-$ nitrogen bonds, these effects are most pronounced because the D–N bonds in D_3N are the weakest halogen–pnictogen bonds. Thus, stronger $D_3N•••A^-$ complexes with a more pronounced D–N stretch occur if we go from F_3N to Cl_3N and Br_3N.

In the following, we exemplify the above with a few concrete examples. For the heavier pnictogen bonds (Pn = P, As, Sb), we find that the trend in bond energy curves $\Delta E(\zeta)$ is set by the interaction energy curves $\Delta E_{int}(\zeta)$, that is, it becomes less stabilizing along D = F, Cl, and Br. However, as the D^1–Pn bond expands more for D = Cl and Br compared to D = F, both the $\Delta E(\zeta_{eq})$ and $\Delta E_{int}(\zeta_{eq})$ in the equilibrium geometry are slightly more stabilizing for D = Cl and Br. This trend in the interaction energy curves $\Delta E_{int}(\zeta)$ is a direct consequence of the electrostatic attraction ΔV_{elstat} and orbital interactions ΔE_{oi}. The curves for the bonding components $\Delta V_{elstat}(\zeta)$ and $\Delta E_{oi}(\zeta)$ are the most stabilizing for D = F because of the larger difference in electronegativity across the D–Pn bonds (*vide supra*). Nevertheless, the Cl–Pn and Br–Pn bonds are substantially weaker than the associated F–Pn bond (*e.g.* $BDE_{F–Sb}$ = 117.9 kcal mol^{-1}, $BDE_{Cl–Sb}$ = 82.8 kcal mol^{-1}, and $BDE_{Br–Sb}$ = 66.2 kcal mol^{-1}; see Table 5.2), and the Cl–Pn and Br–Pn bonds expand to a greater degree. Consequently, the $\Delta E_{oi}(\zeta)$ becomes more stabilizing for D = Cl and Br because the σ* D–Pn antibonding 5a' acceptor orbital is strongly

stabilized and can engage in stronger donor–acceptor interactions with np-type lone pair HOMO on A^- (see Fig. 5.4b). In parallel, the VDD atomic charge on Pn becomes increasingly more positive as the D^1–Pn bond expands (see Fig. 5.4b), which translates into more stabilizing $\Delta V_{elstat}(\zeta)$ for D = Cl and Br. This results in the slight strengthening of $\Delta V_{elstat}(\zeta_{eq})$ and $\Delta E_{oi}(\zeta_{eq})$, and thus $\Delta E_{int}(\zeta_{eq})$, in the equilibrium geometry along D = F, Cl, Br.

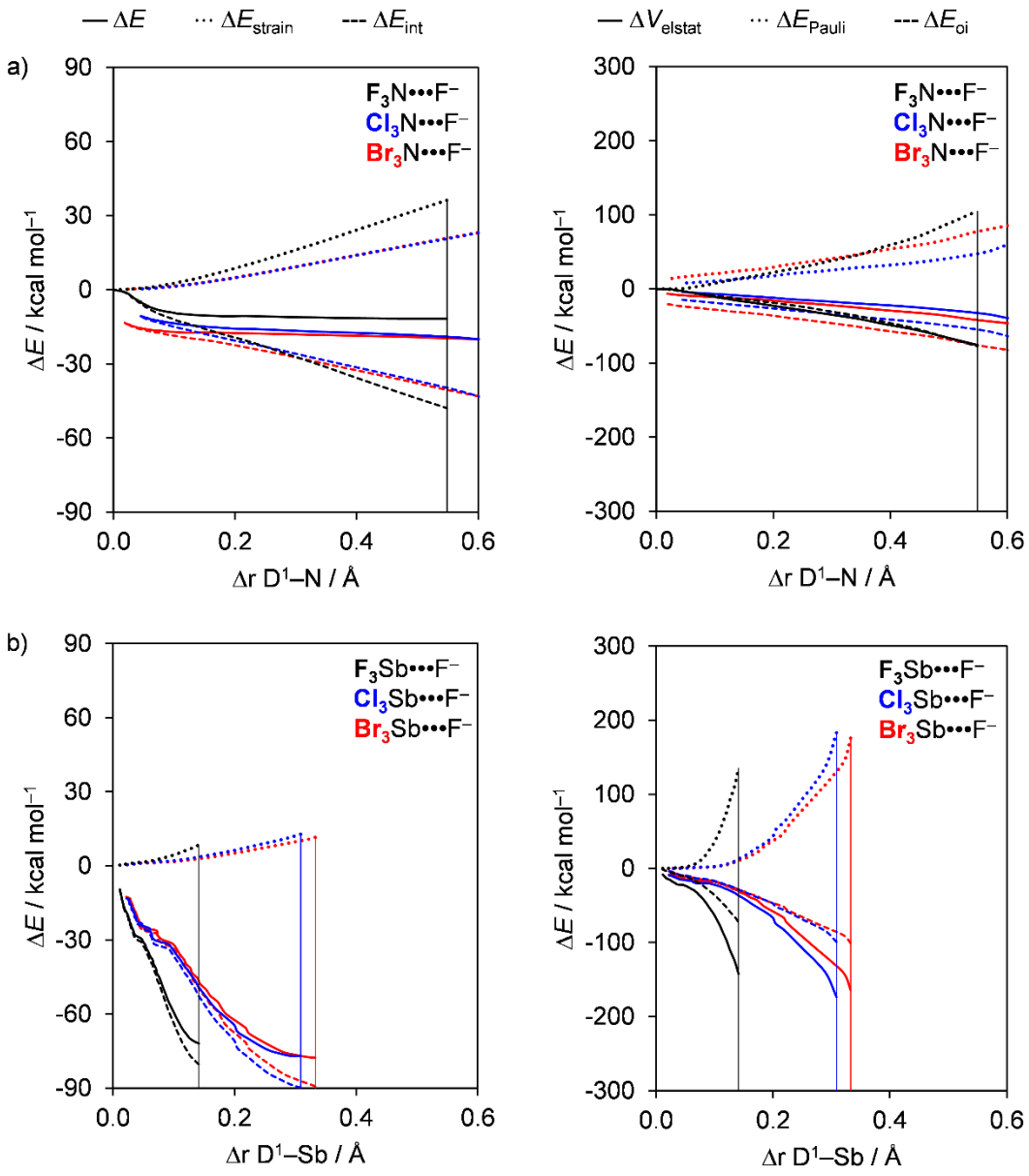

Fig. 5.6. Activation strain (left panel) and energy decomposition (right panel) analyses of (a) $D_3N{\bullet\bullet\bullet}F^-$ and (b) $D_3Sb{\bullet\bullet\bullet}F^-$ (black, D = F; blue, D = Cl; red, D = Br). The vertical lines indicate the position of the stationary points.

The $D_3N{\bullet\bullet\bullet}A^-$ complexes, on the other hand, show on somewhat deviating behavior as compared to the heavier pnictogen bonding complexes exemplified above. Thus, for the $D_3N{\bullet\bullet\bullet}A^-$ complexes, $\Delta E(\zeta)$ becomes significantly more stabilizing along D = F, Cl, and Br instead of remaining relatively constant. This is because the D^1–N bonds are all much weaker (*e.g.* $BDE_{F–N}$ = 59.4 kcal mol^{-1}, $BDE_{Cl–N}$ = 35.6 kcal mol^{-1}, and $BDE_{Br–N}$ = 30.2 kcal mol^{-1}; see Table 5.2), and the stretch $\Delta r_{D^1–Pn}$ for all nitrogen-bonded complexes is much more pronounced, that is, the complexes occur later in the reaction coordinate. For example, the D^1–N stretch has variation between 0.5 and 1.4 Å in $D_3N{\bullet\bullet\bullet}F^-$, whereas the D^1–Sb stretch varies only between 0.1 and 0.3 Å in $D_3Sb{\bullet\bullet\bullet}F^-$ from D = F to Br (see Table 5.1). As result, $D_3N{\bullet\bullet\bullet}A^-$ complexes show more significant streghtening of $\Delta V_{elstat}(\zeta_{eq})$ and $\Delta E_{oi}(\zeta_{eq})$ along D = F to Br in the equilibrium geometries, and, therefore, a significant increase in stability along the same series.

Comparison of pnictogen-, chalcogen-, halogen-, and hydrogen bonds

Our analyses highlight that pnictogen bonds share strong similarities with the corresponding chalcogen bonds (ChB), halogen bonds (XB), and hydrogen bonds (HB).[8] We find that these bonds have considerable covalency on top of electrostatic attraction and can range in strength roughly between –3 and –78 kcal mol^{-1} (see Fig. 5.7). The contribution of the covalent component ΔE_{oi} to the total bonding components ($\Delta V_{elstat} + \Delta E_{oi}$) is up to 97%, 76%, and 65% for XB, ChB, and PnB, respectively, whereas it is up to 66% for HB.[8a,b] The same bonding mechanism with a substantial covalent component is also observed for the archetypal $DM{\bullet\bullet\bullet}A^-$ alkali- and coinage-metal bonds (MB) that have even more pronounced polarization in the D–M bonds.[8c]

Our findings consolidate earlier work and support the charge-transfer character of pnictogen bonds by providing a causal bonding mechanism.[2b,7] The PnB, ChB, and XB are generally stronger than HB due to more stabilizing orbital interactions (see Appendix 5.4 for bond energies ΔE of a representative series of ChB, XB, and HB). On the other hand, hydrogen bonds have less destabilizing Pauli repulsion because of the absent amplitude that the higher-lying D–H FMOs have on H (therefore left out in Fig. 5.7). Our analyses also show that PnB, ChB, and XB, but also MB, have even stronger electrostatic attraction than HB.[8a,b] Note that this cannot be straightforwardly explained by the σ-hole model which, based on hydrogen having the highest $V_{S,max}$, erroneously suggests that HB should have the stronger electrostatic attraction.[6]

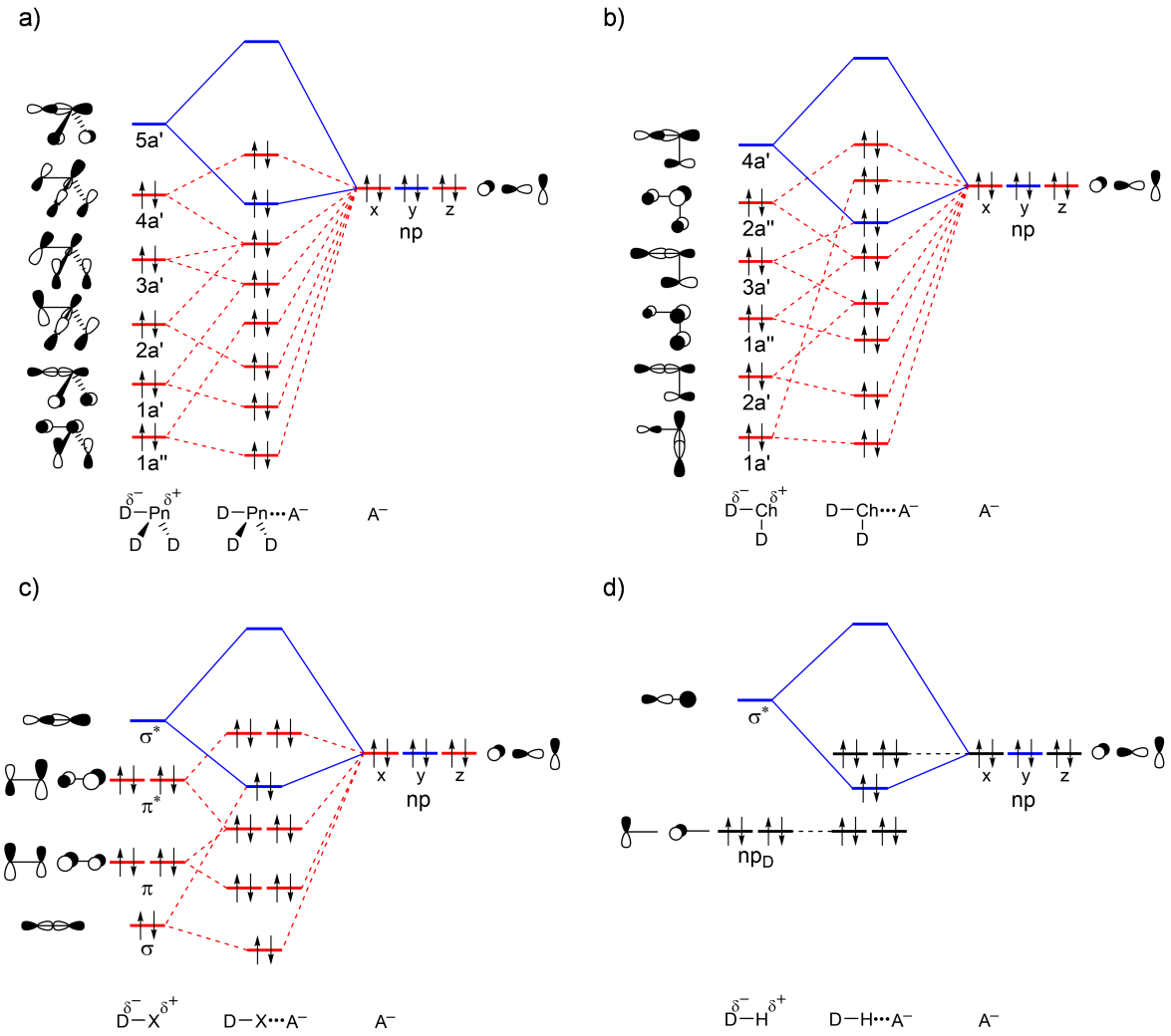

Fig. 5.7. Generic molecular orbital diagrams for (a) $D_3Pn{\bullet\bullet\bullet}A^-$ pnictogen bonds, (b) $D_2Ch{\bullet\bullet\bullet}A^-$ chalcogen bonds, (c) $DX{\bullet\bullet\bullet}A^-$ halogen bonds, and (d) $DH{\bullet\bullet\bullet}A^-$ hydrogen bonds.

5.4 Conclusion

Pnictogen bonds in $D_3Pn{\bullet\bullet\bullet}A^-$ range between 3 and 78 kcal mol^{-1} in strength, becoming stronger as the pnictogen atom becomes more electropositive, along Pn = N, P, As and Sb, and as the halide becomes a stronger Lewis base, along A^- = Br^-, Cl^- and F^-. The trend upon variation of the substituent along D = F, Cl, Br is less pronounced, as are all trends for the relatively weak nitrogen bonds. This follows from our bonding analyses based on relativistic density functional theory.

Our activation-strain and quantitative Kohn-Sham MO bonding analyses reveal that the pnictogen bonds in $D_3Pn{\bullet\bullet\bullet}A^-$ have a considerable covalent component ΔE_{oi}, ranging from 34% to 65% of the bonding components (ΔV_{elstat} + ΔE_{oi}), stemming from HOMO–LUMO interactions between the np-type lone pair HOMO on A^- and the σ* D–Pn antibonding LUMO

on D_3Pn. The $D_3Pn{\bullet\bullet\bullet}A^-$ pnictogen bond becomes stronger as Pn descends in the periodic table along N, P, As and Sb. One reason is the increasing polarization towards Pn of the σ* LUMO and the associated increase in LUMO–HOMO overlap with A^- (along P, As, and Sb this trend is reinforced by the drop in σ* LUMO energy). Another reason is the higher positive charge on Pn which goes with more stabilizing electrostatic interactions with the Lewis base.

Finally, it appears that pnictogen bonds in $D_3Pn{\bullet\bullet\bullet}A^-$ are similar in nature to chalcogen bonds in $D_2Ch{\bullet\bullet\bullet}A^-$, halogen bonds in $DX{\bullet\bullet\bullet}A^-$, and hydrogen bonds in $DH{\bullet\bullet\bullet}A^-$ (Pn = N, P, As, Sb; Ch = O, S, Se, Te; D, X, A = F, Cl, Br). Our work constitutes a unified picture of all these interactions which appear to be far from solely electrostatic phenomena. We conclude that the often-used designation of "noncovalent interactions" for these types of bonds is not consistent with their significant covalent nature. Instead of this term, we propose to refer to such bonds as (weak or strong) intermolecular interactions.

5.5 References

1 G. S. Girolami, *J. Chem. Educ.*, 2009, **86**, 1200–1201.

2 a) S. Scheiner, *Acc. Chem. Res*., 2013, **46**, 280–288; b) S. Scheiner, *Int. J. Quantum Chem*., 2013, **113**, 1609–1620; c) J. E. Del Bene, I. Alkorta and J. Elguero, in *Noncovalent Forces. Challenges and Advances in Computational Chemistry and Physics*, ed. S. Scheiner, Springer, Cham, 2015, vol. 19, pp. 191–263; d) P. R. Joshi and K. Sankaran, *J. Mol. Struct*, 2020, **1217**, 128408; e) R. Mokrai, J. Barret, D. C. Apperley, A. S. Batsanov, Z. Benkő and D. Heift, *Chem. Eur. J.*, 2019, **25**, 4017–4024.

3 a) A. J. Ashe III, *Adv. Organomet. Chem.*, 1990, **30**, 77–97; b) F. Carré, C. Chuit, R. J. P. Corriu, P. Monforte, N. K. Nayyar and C. Reyé, *J. Organomet. Chem.*, 1995, **499**, 147–154; c) S. Bauer, S. Tschirschwitz, P. Lönnecke, R. Frank, B. Kirchner, M. L. Clarke and E. Hey-Hawkins, *Eur. J. Inorg. Chem.*, 2009, **12**, 2776–2788; d) S. Zahn, R. Frank, E. Hey-Hawkins and B. Kirchner, *Chem. Eur. J*., 2011, **17**, 6034–6038; e) J. E. Del Bene, I. Alkorta, G. Sanchez-Sanz and J. Elguero, *Chem. Phys. Lett*., 2011, **512**, 184–187.

4 a) M. S. Taylor, *Coord. Chem. Rev.*, 2020, **413**, 213270; b) K. T. Mahmudov, A. V. Gurbanov, V. A. Aliyeva, G. Resnati and A. J. L. Pombeiro, *Coord. Chem. Rev.*, 2020, **418**, 213381; c) L. M. Lee, M. Tsemperouli, A. I. Poblador-Bahamonde, S. Benz, N. Sakai, K. Sugihara and S. Matile, *J. Am. Chem. Soc*., 2019, **141**, 810–814; d) K. T. Mahmudov, A. V. Gurbanov, F. I. Guseinov and M. Fátima C. Guedes da Silva, *Coord. Chem. Rev.*, 2019, **387**, 32–46; e) G. Park and F. P. Gabbaï, *Chem. Sci.*, 2020, **11**, 10107–10112; f) P. Scilabra, G. Terraneo, A. Daolio, A. Baggioli, A. Famulari, C. Leroy, D. L. Bryce and G. Resnati, *Cryst. Growth Des.*, 2020, **20**, 916–922.

5 a) Y. Li, L. Meng, C. Sun and Y. Zeng, *J. Phys. Chem. A*, 2020, **124**, 3815–3824; b) S. Benz, A. I. Poblador-Bahamonde, N. Low-Ders and S. Matile, *Angew. Chem.*, 2018, **130**, 5506–5510; *Angew. Chem. Int. Ed*., 2018, **57**, 5408–5412; c) A. Gini, M. Paraja, B. Galmés, C. Besnard, A. I. Poblador-Bahamonde, N. Sakai, A. Frontera and S. Matile, *Chem. Sci.*, 2020, **11**, 7086–7091; d) M. Paraja, A. Gini, N. Sakai and S. Matile, *Chem. Eur. J.*, 2020, **26**, 1–7.

6 a) P. Politzer, J. S. Murray and T. Clark, *Phys. Chem. Chem. Phys*., 2013, **15**, 11178–11189; b) P. Politzer, J. S. Murray and M. C. Concha, *J. Mol. Model*., 2008, **14**, 659–665; c) P. Politzer,

J. S. Murray and T. Clark, *J. Phys. Chem. A*, 2019, **123**, 10123–10130; d) A. Bauzá, T. J. Mooibroek and A. Frontera, *ChemPhysChem*, 2015, **16**, 2496–2517.

7 a) R. Shukla and D. Chopra, *Phys. Chem. Chem. Phys.*, 2016, **18**, 13820–13829; b) W. Zierkiewicz, M. Michalczyk, R. Wysokiński and S. Scheiner, *J. Mol. Model.*, 2019, **25**, 152; c) I. Alkorta, J. Elguero and J. E. Del Bene, *J. Phys. Chem. A*, 2013, **117**, 10497–10503; d) J. E. Del Bene, I. Alkorta and J. Elguero, *J. Phys. Chem. A*, 2014, **118**, 2360–2366; e) J. E. Del Bene, I. Alkorta and J. Elguero, *J. Phys. Chem. A*, 2014, **118**, 3386–3392.

8 a) L. P. Wolters and F. M. Bickelhaupt, *ChemistryOpen*, 2012, **1**, 96–105; b) L. de Azevedo Santos, S. C. C. van der Lubbe, T. C. Ramalho, T. A. Hamlin and F. M. Bickelhaupt, *ChemistryOpen*, 2021, **10**, 391-401; c) O. Larrañaga, A. Arrieta, C. Fonseca Guerra, F. M. Bickelhaupt and A. de Cózar, *Chem. Asian J.*, 2021, **16**, 315-321.

9 a) F. M. Bickelhaupt, *J. Comput. Chem*., 1999, **20**, 114–128; b) W. -J. van Zeist and F. M. Bickelhaupt, *Org. Biomol. Chem*., 2010, **8**, 3118–3127; c) P. Vermeeren, S. C. C. van der Lubbe; C. Fonseca Guerra, F. M. Bickelhaupt and T. A. Hamlin, *Nat. Protoc.*, 2020, **15**, 649–667.

10 a) F. M. Bickelhaupt and E. J. Baerends, in *Reviews in Computational Chemistry*, ed. K. B. Lipkowitz and D. B. Boyd, Wiley-VCH, New York, 2000, vol. 15, pp. 1–86; b) F.M. Bickelhaupt, N. M. M. Nibbering, E. M. van Wezenbeek and E.J. Baerends, *J. Phys. Chem*., 1992, **96**, 4864–4873; c) A. Krapp, F. M. Bickelhaupt and G. Frenking, *Chem. Eur. J*., 2006, **12**, 9196–9216; d) T. A. Hamlin, P. Vermeeren, C. Fonseca Guerra, F. M Bickelhaupt, in *Complementary Bonding Analyses*, ed. S. Grabowski, De Gruyter, Berlin, 2021, pp. 199–212.

11 a) G. te Velde, F. M. Bickelhaupt, E. J. Baerends, C. Fonseca Guerra, S. J. A. van Gisbergen, J. G. Snijders and T. Ziegler, *J. Comput. Chem*., 2001, **22**, 931–967; b) C. Fonseca Guerra, J. G. Snijders, G. te Velde and E. J. Baerends, *Theor. Chem. Acc*., 1998, **99**, 391–403; c) ADF2017.103, SCM Theoretical Chemistry; Vrije Universiteit: Amsterdam (The Netherlands); http://www.scm.com.

12 a) Y. Zhao and D. G. Truhlar, *Theor. Chem. Acc.*, 2008, **120**, 215–241; b) Y. Zhao, D. G. Truhlar, *J. Chem. Phys.*, 2006, **125**, 194101.

13 E. van Lenthe and E. J. Baerends, *J. Comput. Chem.*, 2003, **24**, 1142–1156.

14 E. van Lenthe and E. J. Baerends, J. G. Snijders, *J. Chem. Phys.*, 1994, **101**, 9783–9792.

15 X. Sun, T. M. Soini, J. Poater, T. A. Hamlin and F. M. Bickelhaupt, *J. Comput. Chem.*, 2019, **40**, 2227–2233.

16 a) F. M. Bickelhaupt, N. J. R van Eikema Hommes, C. Fonseca Guerra and E. J Baerends, *Organometallics*, 1996, **15**, 2923–2931; b) C. Fonseca Guerra, J. -W. Handgraaf, E. J. Baerends and F. M. Bickelhaupt, *J. Comput. Chem*., 2004, **25**, 189–210.

17 a) M. Swart and F. M. Bickelhaupt, *J. Chem. Theory Comput.*, 2006, **2**, 281–287; b) W. J. van Zeist, Y. Ren and F. M. Bickelhaupt, *Sci. China Chem*., 2010, **53**, 210–215.

18 J. -W. Zou, Y. -J. Jiang, M. Guo, G. -X. Hu, B. Zhang, H. -C. Liu and Q. -S. Yu, *Chem. Eur. J.*, 2005, **11**, 740–751.

5.6 Appendices

Appendix 5.1. Activation strain analyses (in kcal mol^{-1}) of $D_3Pn{\bullet\bullet\bullet}A^-$ pnictogen bonds at the equilibrium geometries (in Å, deg.).[a]

$D_3Pn{\bullet\bullet\bullet}A^-$	ΔE	ΔE_{strain}	ΔE_{int}	$r_{Pn\cdots A^-}$	$r_{Pn-D}{}^1$	$r_{Pn-D}{}^2$	$\Delta r_{Pn-D}{}^1$	$\Delta r_{Pn-D}{}^2$	Θ_1	Θ_2	Θ_3	$\Delta\Theta_1$	$\Delta\Theta_2$
$F_3N{\bullet\bullet\bullet}F^-$	–11.8	32.5	–44.3	1.859	1.859	1.339	0.503	–0.017	93.0	102.4	170.3	–8.9	0.5
$F_3N{\bullet\bullet\bullet}Cl^-$	–3.5	0.8	–4.3	3.239	1.404	1.347	0.048	–0.009	100.4	102.3	168.3	–1.5	0.4
$F_3N\cdots Br^-$	–2.9	0.5	–3.5	3.484	1.396	1.348	0.040	–0.008	100.7	102.2	166.8	–1.2	0.3
$Cl_3N{\bullet\bullet\bullet}F^-$	–30.4	55.7	–86.1	1.416	3.243	1.754	1.490	0.001	82.0	108.1	170.7	–25.7	0.4
$Cl_3N{\bullet\bullet\bullet}Cl^-$	–5.6	22.9	–28.5	2.328	2.328	1.757	0.575	0.004	99.9	106.9	146.6	–7.8	–0.8
$Cl_3N{\bullet\bullet\bullet}Br^-$	–6.2	3.5	–9.7	2.920	1.902	1.777	0.149	0.024	104.9	106.8	145.6	–2.8	–0.9
$Br_3N{\bullet\bullet\bullet}F^-$	–30.2	53.2	–83.3	1.411	3.323	1.928	1.417	0.022	84.5	108.5	165.7	–24.0	0.0
$Br_3N{\bullet\bullet\bullet}Cl^-$	–8.0	2.0	–10.0	2.813	2.017	1.932	0.111	0.026	105.7	107.7	149.4	–2.8	–0.8
$Br_3N{\bullet\bullet\bullet}Br^-$	–7.0	17.2	–24.2	2.322	2.322	1.972	0.416	0.066	105.4	106.8	127.2	–3.1	–1.7
$F_3P{\bullet\bullet\bullet}F^-$	–48.9	17.4	–66.4	1.753	1.753	1.608	0.189	0.044	86.9	98.7	189.4	–10.6	1.2
$F_3P{\bullet\bullet\bullet}Cl^-$	–16.0	4.4	–20.4	2.700	1.647	1.580	0.083	0.016	91.9	97.8	183.4	–5.6	0.3
$F_3P{\bullet\bullet\bullet}Br^-$	–12.9	3.0	–15.9	2.982	1.631	1.576	0.067	0.012	92.9	97.7	181.6	–4.6	0.2
$Cl_3P{\bullet\bullet\bullet}F^-$	–67.4	31.8	–99.3	1.649	2.627	2.103	0.572	0.048	88.6	100.2	181.4	–11.8	–0.2
$Cl_3P{\bullet\bullet\bullet}Cl^-$	–25.5	14.4	–39.8	2.370	2.370	2.089	0.315	0.034	91.7	100.1	174.6	–8.7	–0.3
$Cl_3P{\bullet\bullet\bullet}Br^-$	–20.5	10.7	–31.3	2.617	2.318	2.085	0.263	0.030	92.8	100.1	172.9	–7.6	–0.3
$Br_3P{\bullet\bullet\bullet}F^-$	–71.0	30.2	–101.2	1.637	2.874	2.272	0.647	0.045	89.6	100.3	175.4	–11.3	–0.6
$Br_3P{\bullet\bullet\bullet}Cl^-$	–28.5	15.4	–43.9	2.312	2.609	2.265	0.382	0.038	92.0	100.2	172.0	–8.9	–0.7
$Br_3P{\bullet\bullet\bullet}Br^-$	–23.4	11.9	–35.3	2.550	2.550	2.261	0.323	0.034	93.0	100.2	170.6	–7.9	–0.7
$F_3As{\bullet\bullet\bullet}F^-$	–61.0	12.6	–73.6	1.900	1.900	1.757	0.183	0.040	87.1	97.2	188.7	–8.7	1.4
$F_3As{\bullet\bullet\bullet}Cl^-$	–28.7	6.1	–34.9	2.595	1.836	1.744	0.119	0.027	89.5	95.8	182.3	–6.3	0.0
$F_3As{\bullet\bullet\bullet}Br^-$	–24.2	4.8	–29.0	2.820	1.820	1.741	0.103	0.024	90.2	95.6	180.4	–5.6	–0.2
$Cl_3As{\bullet\bullet\bullet}F^-$	–70.0	18.7	–88.7	1.850	2.585	2.229	0.406	0.050	91.6	98.7	175.7	–7.5	–0.4
$Cl_3As{\bullet\bullet\bullet}Cl^-$	–35.1	11.3	–46.4	2.465	2.465	2.223	0.286	0.044	93.4	98.2	169.7	–5.7	–0.9
$Cl_3As{\bullet\bullet\bullet}Br^-$	–30.1	9.6	–39.7	2.668	2.437	2.220	0.258	0.041	93.9	98.2	167.9	–5.2	–0.9
$Br_3As{\bullet\bullet\bullet}F^-$	–71.5	17.3	–88.8	1.843	2.789	2.391	0.447	0.049	93.0	99.1	172.0	–6.7	–0.6
$Br_3As{\bullet\bullet\bullet}Cl^-$	–37.0	10.7	–47.6	2.438	2.663	2.389	0.321	0.047	94.7	98.6	165.7	–5.0	–1.1
$Br_3As{\bullet\bullet\bullet}Br^-$	–32.0	9.2	–41.2	2.634	2.634	2.387	0.292	0.045	95.2	98.6	164.0	–4.5	–1.1
$F_3Sb{\bullet\bullet\bullet}F^-$	–72.0	8.8	–80.8	2.037	2.037	1.930	0.144	0.037	85.4	97.0	193.9	–8.9	2.7
$F_3Sb{\bullet\bullet\bullet}Cl^-$	–38.9	5.8	–44.7	2.643	2.005	1.923	0.112	0.030	87.0	95.1	188.3	–7.3	0.8
$F_3Sb{\bullet\bullet\bullet}Br^-$	–33.6	5.0	–38.7	2.840	1.996	1.921	0.103	0.028	87.5	94.8	186.7	–6.8	0.5
$Cl_3Sb{\bullet\bullet\bullet}F^-$	–77.1	12.3	–89.4	2.017	2.649	2.399	0.301	0.051	89.4	97.6	183.7	–7.6	0.6
$Cl_3Sb{\bullet\bullet\bullet}Cl^-$	–42.7	8.9	–51.7	2.592	2.592	2.393	0.244	0.045	90.5	96.7	178.4	–6.5	–0.3
$Cl_3Sb{\bullet\bullet\bullet}Br^-$	–37.3	8.0	–45.3	2.780	2.577	2.391	0.229	0.043	90.9	96.6	177.0	–6.1	–0.4
$Br_3Sb{\bullet\bullet\bullet}F^-$	–77.7	11.5	–89.2	2.014	2.842	2.559	0.332	0.049	90.5	98.0	181.2	–7.2	0.3
$Br_3Sb{\bullet\bullet\bullet}Cl^-$	–43.5	8.5	–52.0	2.580	2.782	2.556	0.272	0.046	91.6	97.2	175.6	–6.1	–0.5
$Br_3Sb{\bullet\bullet\bullet}Br^-$	–38.1	7.7	–45.8	2.766	2.766	2.555	0.256	0.045	91.9	97.0	174.2	–5.8	–0.7

[a] Computed at ZORA-M06/QZ4P.

Appendix 5.2. Energy decomposition analyses (in kcal mol^{-1}) of $D_3Pn{\bullet\bullet\bullet}A^-$ pnictogen bonds at the equilibrium geometries.[a]

$D_3Pn{\bullet\bullet\bullet}A^-$	ΔE_{int}	ΔV_{elstat}	ΔE_{Pauli}	ΔE_{oi}	ε(5a')	$\langle$5a'$|$np$_y\rangle$	$\langle$4a'$|$np$_y\rangle$	$Pop_{5a'}$	Pop_{npy}	$\Delta Q_{D_3Pn}{}^{VDD}$
$F_3N{\bullet\bullet\bullet}F^-$	–44.3	–66.9	89.6	–67.0	–5.1	0.12	0.05	0.40	1.68	–0.30
$F_3N{\bullet\bullet\bullet}Cl^-$	–4.3	–5.8	4.5	–3.1	–0.2	0.10	0.05	0.02	1.99	–0.01
$F_3N\cdots Br^-$	–3.5	–4.7	3.5	–2.3	–0.1	0.10	0.04	0.02	2.00	0.00
$Cl_3N{\bullet\bullet\bullet}F^-$	–86.1	–208.3	431.6	–309.5	–6.5	0.13	0.08	1.24	1.34	–0.65
$Cl_3N{\bullet\bullet\bullet}Cl^-$	–28.5	–41.8	69.2	–55.9	–5.2	0.11	0.06	0.54	1.59	–0.36
$Cl_3N{\bullet\bullet\bullet}Br^-$	–9.7	–11.9	18.8	–16.7	–3.7	0.09	0.03	0.26	1.75	–0.18
$Br_3N{\bullet\bullet\bullet}F^-$	–83.3	–204.1	439.6	–318.8	–6.0	0.12	0.07	1.25	1.38	–0.67
$Br_3N{\bullet\bullet\bullet}Cl^-$	–10.0	–10.3	19.2	–18.9	–3.6	0.08	0.04	0.23	1.86	–0.18
$Br_3N{\bullet\bullet\bullet}Br^-$	–24.2	–51.1	95.0	–68.1	–4.6	0.12	0.08	0.67	1.60	–0.44
$F_3P{\bullet\bullet\bullet}F^-$	–66.4	–167.7	221.7	–120.3	–2.1	0.15	0.19	0.28	1.75	–0.35
$F_3P{\bullet\bullet\bullet}Cl^-$	–20.4	–40.4	46.0	–25.9	–1.2	0.22	0.17	0.17	1.87	–0.12
$F_3P{\bullet\bullet\bullet}Br^-$	–15.9	–29.1	30.7	–17.4	–1.1	0.25	0.16	0.18	1.81	–0.09
$Cl_3P{\bullet\bullet\bullet}F^-$	–99.3	–222.6	312.1	–188.7	–4.1	0.16	0.13	0.48	1.70	–0.52
$Cl_3P{\bullet\bullet\bullet}Cl^-$	–39.8	–84.8	119.2	–74.2	–3.1	0.20	0.12	0.40	1.73	–0.31
$Cl_3P{\bullet\bullet\bullet}Br^-$	–31.3	–64.2	86.5	–53.6	–2.9	0.20	0.08	0.36	1.75	–0.26
$Br_3P{\bullet\bullet\bullet}F^-$	–101.2	–228.4	331.2	–204.1	–4.2	0.15	0.12	0.53	1.69	–0.56
$Br_3P{\bullet\bullet\bullet}Cl^-$	–43.9	–95.9	141.9	–89.8	–3.4	0.19	0.13	0.45	1.72	–0.37
$Br_3P{\bullet\bullet\bullet}Br^-$	–35.3	–73.7	104.8	–66.5	–3.2	0.20	0.12	0.42	1.72	–0.32
$F_3As{\bullet\bullet\bullet}F^-$	–73.6	–145.4	158.0	–86.2	–2.6	0.15	0.15	0.23	1.77	–0.30
$F_3As{\bullet\bullet\bullet}Cl^-$	–34.9	–64.4	67.6	–38.1	–2.2	0.21	0.16	0.20	1.84	–0.17
$F_3As{\bullet\bullet\bullet}Br^-$	–29.0	–52.1	52.8	–29.7	–2.1	0.22	0.16	0.18	1.85	–0.14
$Cl_3As{\bullet\bullet\bullet}F^-$	–88.7	–166.5	194.3	–116.5	–3.7	0.16	0.11	0.34	1.74	–0.42
$Cl_3As{\bullet\bullet\bullet}Cl^-$	–46.4	–85.5	101.9	–62.8	–3.2	0.21	0.11	0.33	1.76	–0.29
$Cl_3As{\bullet\bullet\bullet}Br^-$	–39.7	–71.4	83.2	–51.5	–3.1	0.22	0.10	0.31	1.78	–0.26
$Br_3As{\bullet\bullet\bullet}F^-$	–88.8	–167.8	203.9	–124.9	–3.7	0.15	0.11	0.37	1.75	–0.45
$Br_3As{\bullet\bullet\bullet}Cl^-$	–47.6	–89.9	112.3	–70.1	–3.3	0.20	0.11	0.35	1.78	–0.33
$Br_3As{\bullet\bullet\bullet}Br^-$	–41.2	–75.9	92.9	–58.3	–3.3	0.21	0.10	0.34	1.76	–0.31
$F_3Sb{\bullet\bullet\bullet}F^-$	–80.8	–148.9	143.6	–75.5	–3.0	0.16	0.15	0.20	1.82	–0.31
$F_3Sb{\bullet\bullet\bullet}Cl^-$	–44.7	–82.6	83.4	–45.4	–2.7	0.23	0.18	0.21	1.83	–0.21
$F_3Sb{\bullet\bullet\bullet}Br^-$	–38.7	–70.7	70.9	–38.9	–2.7	0.24	0.18	0.21	1.84	–0.19
$Cl_3Sb{\bullet\bullet\bullet}F^-$	–89.4	–158.0	161.0	–92.4	–3.4	0.16	0.11	0.26	1.79	–0.38
$Cl_3Sb{\bullet\bullet\bullet}Cl^-$	–51.7	–93.3	100.9	–59.2	–3.2	0.22	0.11	0.28	1.80	–0.28
$Cl_3Sb{\bullet\bullet\bullet}Br^-$	–45.3	–81.1	87.3	–51.5	–3.1	0.23	0.10	0.28	1.82	–0.27
$Br_3Sb{\bullet\bullet\bullet}F^-$	–89.2	–157.4	166.1	–97.9	–3.4	0.16	0.10	0.28	1.79	–0.41
$Br_3Sb{\bullet\bullet\bullet}Cl^-$	–52.0	–95.2	106.8	–63.5	–3.2	0.21	0.11	0.29	1.81	–0.31
$Br_3Sb{\bullet\bullet\bullet}Br^-$	–45.8	–83.2	92.7	–55.3	–3.2	0.22	0.11	0.30	1.81	–0.30

[a] Computed at ZORA-M06/QZ4P; ε(5a') = 5a' orbital energy of the prepared D_3Pn fragment (in eV); $\langle\Phi|np\rangle$ = overlap between the Φ orbital of the D_3Pn fragment (see Fig. 5.2) and one of the np orbitals of the halide A^-; Pop = Gross population (in electrons) of indicated orbital.

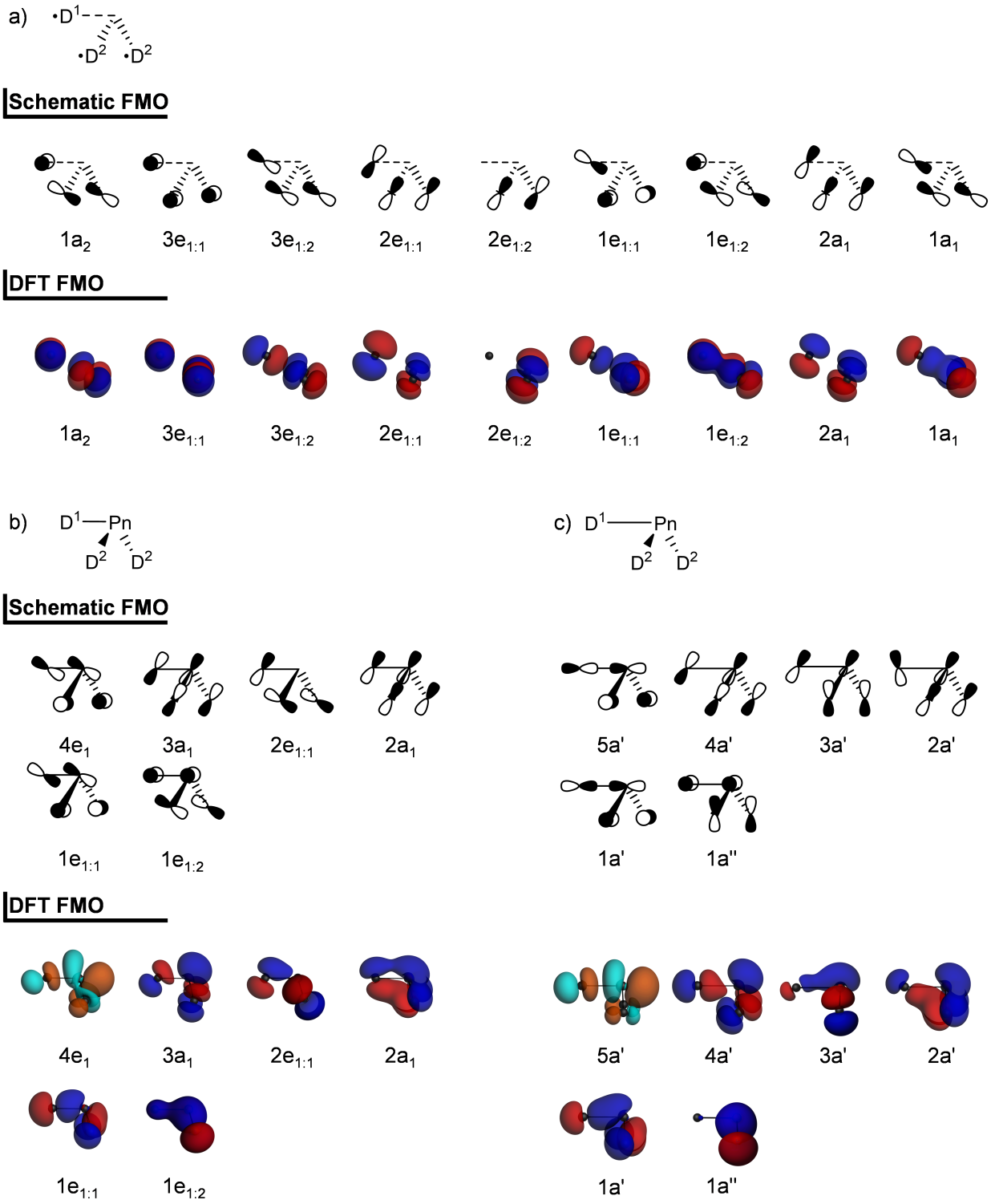

Appendix 5.3. Schematic FMO and DFT MO isosurfaces (at 0.04 a.u.) for (a) the $(D^{\bullet})_3$ molecule in its quadruplet valence state at C_{3v} symmetry and for the D_3Pn fragment in (b) the ground state at C_{2v} symmetry and in (c) the geometry of the complex at C_s symmetry.

Appendix 5.4. Activation strain and energy decomposition analyses (in kcal mol^{-1}) of D_mZ•••A^- hydrogen bonds, halogen bonds, chalcogen bonds, and pnictogen bonds at the equilibrium geometries.[a]

D_mZ•••A^-	ΔE	ΔE_{strain}	ΔE_{int}	ΔV_{elstat}	ΔE_{Pauli}	ΔE_{oi}
FH•••F$^-$ [b]	–45.8	22.1	–67.9	–76.2	72.9	–64.6
FF•••F$^-$ [b]	–30.5	28.0	–58.5	–44.6	84.3	–98.1
FCl•••F$^-$ [b]	–52.3	14.0	–66.4	–94.5	124.9	–96.7
FBr•••F$^-$ [b]	–62.3	10.0	–72.3	–104.0	113.8	–82.0
FI•••F$^-$ [b]	–70.3	6.9	–77.2	–116.9	115.3	–75.7
F_2O•••F$^-$ [b]	–21.9	28.3	–50.2	–55.3	87.5	–82.4
F_2S•••F$^-$ [b]	–50.1	16.2	–66.3	–126.5	168.3	–108.1
F_2Se•••F$^-$ [b]	–62.4	11.4	–73.7	–124.6	136.6	–85.7
F_2Te•••F$^-$ [b]	–72.4	7.9	–80.3	–134.6	132.8	–78.6
F_3N•••F$^-$	–11.8	32.5	–44.3	–66.9	89.6	–67.0
F_3P•••F$^-$	–48.9	17.4	–66.4	–167.7	221.7	–120.3
F_3As•••F$^-$	–61.0	12.6	–73.6	–145.4	158.0	–86.2
F_3Sb•••F$^-$	–72.0	8.8	–80.8	–148.9	143.6	–75.5

[a] Computed at ZORA-M06/QZ4P.

[b] Computed at ZORA-M06/QZ4P (from: L. de Azevedo Santos, T. A. Hamlin, T. C. Ramalho, F. M. Bickelhaupt, *ChemistryOpen*, 2021, **10**, 391–401).

6 | Summary

This thesis provides a unified picture of chalcogen bonds (ChB) and pnictogen bonds (PnB), together with hydrogen bonds (HB) and halogen bonds (XB), based on detailed quantum chemical investigations on the nature and strength of intermolecular interactions in $D_nZ\bullet\bullet\bullet A^-$ complexes, mediated via atoms Z of groups 15–17 in the periodic table. State-of-the-art analyses reveal that these intramolecular interactions have a strong covalent component and are certainly not purely electrostatic in nature. Therefore, "Non-Covalent Interactions (NCI)" does not seem to be a proper designation for PnB, ChB, XB, and HB. Herein, it is suggested to use the designation "Intermolecular Covalent Interactions (ICI)" to better assemble the features of the nature of the associated intermolecular interactions. This follows from the findings reported in Chapters 3–5 of this thesis.

In Chapter 3, a hierarchical *ab initio* benchmark study of $D_2Ch\bullet\bullet\bullet A^-$ anionic chalcogen bonds (Ch = S, Se; D, A = F, Cl) was performed aiming to identify the ideal DFT approach to compute accurate chalcogen-bond energies and geometries. Compared to the best *ab initio* level found at ZORA-CCSD(T)/ma-ZORA-def2-QZVPP, the best $D_2Ch\bullet\bullet\bullet A^-$ geometries are given by the meta-hybrid functionals M06, M06-HF, and M06-2X, and the best chalcogen bond energies are given by the hybrid B3LYP functional and by the meta-hybrid M06 and M06-2X. The GGA density functionals, such as BLYP-D3(BJ) and PBE, perform the worst. In essence, these findings have revealed efficient, accurate, and non-expensive approaches for the routine investigation of chalcogen bonds.

The nature of the ChB and PnB were investigated in Chapters 4 and 5, respectively. To this end, the archetypal $D_2Ch\bullet\bullet\bullet A^-$ chalcogen-bonded and $D_3Pn\bullet\bullet\bullet A^-$ pnictogen-bonded complexes (Ch = O, S, Se, Te; Pn = N, P, As, Sb; D, A = F, Cl, Br) were used as models to compute accurate trends in bond strength and to understand these trends in terms of quantitative Kohn-Sham molecular orbital theory. Herein, it is found that both ChB and PnB are very similar to XB and HB. That is, they are all far from being purely electrostatic phenomena and have a substantial contribution from donor–acceptor interactions. These findings reveal the bonding mechanism of intermolecular interactions based on a causal quantitative quantum chemical method that odds with the commonly accepted σ-hole model.

7 | Acknowledgements

I am deeply thankful to my supervisors for all the care and support during my PhD. To Teo, I am grateful for accepting me in the Molecc group in 2011 during my bachelor's and, since then, encouraging me to do my best as a researcher. It has been a long way of learning and respect, which I could not have enjoyed more. To Matthias, I am very thankful for the valuable scientific discussions and for having me in the TheoCheM group. Despite a top scientist, I have met a patient, generous, and kind person. Herein, I would like to extend my gratitude to Célia for the kindness and care about my future carrier and well-being. I am looking forward to our future work during my postdoc. I would also like to thank Trevor, my co-promotor, for the insightful discussions about scientific career, future challenges, and for always pushing me to the next level. I have no words to express how much I have grown up as a professional during my stay in Amsterdam.

The greatest advantage of being a joint degree PhD student is to have the opportunity to meet so many lovely people. I thank my colleagues at the UFLA and at the VU for all the fun and friendly moments we spent together, namely Alexandre, Ander, Aquino, Bruna, Daiana, Daniel, Elaine, Francisco, Giovanna, Ingrid, Joyce, Letícia, Lívia, Maíra, Marcus, Stephen, Tamiris, Telles, Thaís, Arno, Ayush, Celine, Chandan, Eva, Jelena, Johan, Nicolai, Pascal, Song, Souloke, Stephanie, Thomas, and Xiaobo. Special thanks to Matheus for our extensive discussions about science, politics, and football. I am also especially grateful for my office mates Enrico, Marco, Maxime, and Tanja for creating such a pleasant working environment and for their contributions to "the dictionary".

Lastly, I feel blessed to have my parents and my sister, even with the Atlantic Ocean and the North Sea in between us, guiding and supporting me. There is no need to say that every achievement in my life, every step I take, is because of you. I am especially grateful for Dani, my best friend, partner, and most brilliant person I ever met in all aspects.

8 | List of publications

25. *Source of Cooperativity and Ring Equalization in Hydrogen-Bonded Supramolecular Polymers*
L. de Azevedo Santos, D. Cesario, P. Vermeeren, S. C. C. van der Lubbe, F. Nunzi, C. Fonseca Guerra
Submitted

24. *Organic iodine induces unexpected conformational effects in 1-fluoro-2-iodoethane and 2-iodoethanol*
F. A. Martins, L. de Azevedo Santos, D. Rodrigues Silva, F. M. Bickelhaupt, C. Fonseca Guerra, M. P. Freitas
Manuscript in preparation

23. *Steric Repulsion, Not Electrostatics, Drives the Directionality of Pnictogen, Chalcogen, and Halogen Bonds*
L. de Azevedo Santos, T. C. Ramalho, T. A. Hamlin, F. M. Bickelhaupt
Manuscript in preparation

22. *Management of powdery mildew in soybean plants and systemic detection of phosphite combined with fungicides*
A. E. Vilela, M. L. Vilela de Resende, F. C. L. de Medeiros, M. H. Brito Pereira, W. D. Santiago, D. M. dos Santos Botelho, L. de Azevedo Santos, T. C. Ramalho
Manuscript in preparation

21. *Dipolar Repulsion in α-Halocarbonyl Compounds Revisited*
D. Rodrigues Silva, L. de Azevedo Santos, T. A. Hamlin, F. M. Bickelhaupt, M. P. Freitas, C. Fonseca Guerra
Phys. Chem. Chem. Phys. **2021**, *Accepted*.
DOI: 10.1039/D1CP02502C

20. *The Pnictogen Bond: A Quantitative Molecular Orbital Picture*
L. de Azevedo Santos, T. A. Hamlin, T. C. Ramalho, F. M. Bickelhaupt
Phys. Chem. Chem. Phys. **2021**, *23*, 13842–13852.
DOI: 10.1039/D1CP01571K

19. *A Quantitative MO Perspective of the Chalcogen Bond*
L. de Azevedo Santos, S. C. C. van der Lubbe, T. A. Hamlin, T. C. Ramalho, F. M. Bickelhaupt
ChemistryOpen **2021**, *10*, 391–401 (Front Cover and Cover Profile).
DOI: 10.1002/open.202000323

18. *The Gauche Effect in XCH_2CH_2X Revisited*
D. Rodrigues Silva, L. de Azevedo Santos, T. A. Hamlin, C. Fonseca Guerra, M. P. Freitas, F. M. Bickelhaupt
ChemPhysChem **2021**, *22*, 641–648.
DOI: 10.1002/cphc.202100090

17. *Chalcogen Bonds: Hierarchical ab initio benchmark and density functional theory performance study*
L. de Azevedo Santos, T. C. Ramalho, T. A. Hamlin, F. M. Bickelhaupt
J. Comput. Chem. **2021**, *42*, 688–698 (Front Cover)
DOI: 10.1002/jcc.26489

16. *Nature and Strength of Lewis Acid/Base Interaction in Boron and Nitrogen Trihalides*
D. Rodrigues Silva, L. de Azevedo Santos, M. P. Freitas, C. Fonseca Guerra, T. A. Hamlin
Chem. Asian J. **2020**, *15*, 4043–4054 (Very Important Paper and Front Cover)
DOI: 10.1002/asia.202001127

15. *Halogen Bonds in Ligand-Protein Systems: Molecular Orbital Theory for Drug Design*
E. Margiotta, S. C. C. van der Lubbe, L. de Azevedo Santos, G. Paragi, S. Moro, F. M. Bickelhaupt, C. Fonseca Guerra
J. Chem. Inf. Model. **2020**, *60*, 1317–1328
DOI: 10.1021/acs.jcim.9b00946

14. *Synthesis and special characterization through X-ray analysis of 1,8-dioxooctahydroxanthenes*
M. L. da Silva, R. R. Teixeira, L. de Azevedo Santos, F. T. Martins, T. C. Ramalho
Arab. J. Chem. **2020**, *13*, 974–987
DOI: 10.1016/j.arabjc.2017.09.001

13. *The Role of Intramolecular Interactions on the Bioactive Conformation of Epinephrine*
D. Rodrigues Silva, J. M. Silla, L. de Azevedo Santos, E. F. F. da Cunha, M. P. Freitas
Molecular Informatics **2019**, *38*, 1800167
DOI: 10.1002/minf.201800167

12. *Could Quantum Mechanical Properties Be Reflected on Classical Molecular Dynamics? The Case of Halogenated Organic Compounds of Biological Interest*
L. de Azevedo Santos, I. G. Prandi, T. C. Ramalho
Front. Chem. **2019**, *7*, 848
DOI: 10.3389/fchem.2019.00848

11. *Experimental and Theoretical Studies of Solvent Polarity Influence on the Preparation of Molecularly Imprinted Polymers for the Removal of Estradiol from Water*
L. P. dos Santos Xavier, A. C. Dias, B. E. Lobo Baeta, L. de Azevedo Santos, T. C. Ramalho, S. F. de Aquino, A. C. da Silva
New J. Chem. **2019**, *43*, 1775–1784
DOI: 10.1039/C8NJ03639J

10. *Etherification of Hydroxymethylfurfural with Preyssler Heteropolyacids Immobilized on Magnetic Composites*
O. H. P. Cuervo, H. A. Rojas, L. de Azevedo Santos, T. C. Ramalho, G. P. Romanelli, J. J. Martínez
ChemistrySelect **2018**, *3*, 5526–5533
DOI: 10.1002/slct.201801051

9. *Insights into the pharmaceuticals and mechanisms of neurological orphan diseases: Current Status and future expectations*
T. C. Ramalho, A. A. de Castro, T. S. Tavares, M. C. Silva, D. Rodrigues Silva, P. H. Cesar, L. de Azevedo Santos, E. F. F. da Cunha, E. Nepovimova, K. Kuca
Progress in Neurobiology **2018**, *169*, 135–157
DOI: 10.1016/j.pneurobio.2018.06.011

8. *Molecularly imprinted polymers for selective adsorption of quinoline: theoretical and experimental studies*
L. N. M. Saavedra, R. G. Penido, L. de Azevedo Santos, T. C. Ramalho, B. E. Lobo Baeta, M. C. Pereira, A. C. da Silva
RSC Adv. **2018**, *8*, 28775
DOI: 10.1039/C8RA04261F

7. *Reductive amination of levulinic acid to different pyrrolidones on Ir/SiO 2 -SO 3 H: Elucidation of reaction mechanism*
J. J. Martínez, L. Silva, H. A. Rojas, G. P. Romanelli, L. de Azevedo Santos, T. C. Ramalho, M. H. Brijaldo, F. B. Passos
Catal. Today **2017**, *296*, 118–126
DOI: 10.1016/j.cattod.2017.08.038

6. *Structural Analysis of Two Tetraketones and Theoretical Investigation of the Reactions Involved in their Preparation*
M. L. da Silva, R. R. Teixeira, L. de Azevedo Santos, F. T. Martins, T. C. Ramalho
J. Mol. Struct. **2017**, *1156*, 700–711
DOI: 10.1016/j.molstruc.2017.11.105

5. *Toward the Classical Description of Halogen Bonds: A Quantum Based Generalized Empirical Potential for Fluorine, Chlorine, and Bromine*
L. de Azevedo Santos, E. F. F. da Cunha, T. C. Ramalho
J. Phys. Chem. A **2017**, *121*, 2442–2451
DOI: 10.1021/acs.jpca.6b13112

4. *Hydrophobic Non-covalent Interactions of Inosine-Phenylalanine: A Theoretical Model for Investigating the Molecular Recognition of Nucleobases*
   L. de Azevedo Santos, E. F. F. da Cunha, M. P. Freitas, T. C. Ramalho
   J. Phys. Chem. A **2014**, *118*, 5808–5817
   DOI: 10.1021/jp411230w

3. *Ring-annelated corannulenes as fullerene receptors. A DFT-D study*
   D. Josa, L. de Azevedo Santos, I. González-Veloso, J. Rodríguez-Otero, E. M. Cabaleiro-Lago, T. C. Ramalho
   RSC Adv. **2014**, *4*, 29826–29833
   DOI: 10.1039/c4ra02744b

2. *Substituted Corannulenes and Sumanenes as Fullerene Receptors. A Dispersion-Corrected Density Functional Theory Study*
   D. Josa, J. Rodríguez-Otero, E. M. Cabaleiro-Lago, L. de Azevedo Santos, T. C. Ramalho
   J. Phys. Chem. A **2014**, *118*, 9521–9528
   DOI: 10.1021/jp5061107

1. *Thermodynamic framework of hydrophobic/electrostatic interactions*
   T. C. Ramalho, L. de Azevedo Santos, E. F.F. da Cunha
   J. Biomol. Struct. Dyn. **2013**, *31*, 995–1000
   DOI: 10.1080/07391102.2012.748539

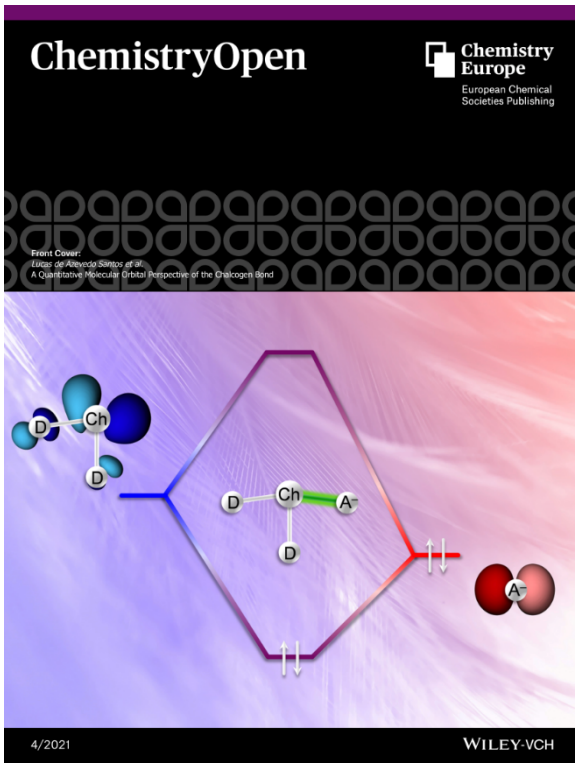
ChemistryOpen
Chemistry Europe
European Chemical Societies Publishing
Front Cover:
Lucas de Azevedo Santos et al.
A Quantitative Molecular Orbital Perspective of the Chalcogen Bond
D
Ch
A
4/2021
WILEY-VCH


Volume 42, Issue 10 | 2021
Issue 10 (April 15, 2021)
Journal of
COMPUTATIONAL
CHEMISTRY
Organic • Inorganic • Physical
Biological • Materials
www.c-chem.org
CCSD(T)/QZVPP+
HF
MP2
CCSD
QZVPP
TZVP
DZ
D
Ch
A
M06-2X
M06
B3LYP
Editors:
Charles L. Brooks III • Masahiro Ehara • Gernot Frenking • Peter R. Schreiner
WILEY


CHEMISTRY
AN ASIAN JOURNAL
www.chemasianj.org
B
N
H
Br
Cl
F
15/23
2020
A Journal of
ACES
Asian Chemical Editorial Society
Front Cover:
WILEY-VCH